Doctoral Dissertation
Doctoral Program in Chemical Engineering (32nd Cycle)

Catalytic processes for CO₂ conversion into Synthetic Methane

Eduard Alexandru Morosanu
* * * * * *

Supervisors
Prof. Samir Bensaid, Supervisor
Prof. Raffaele Pirone, Co-Supervisor

Doctoral Examination Committee:
Prof. Claudio Ampelli, Referee, Università degli studi di Messina
Prof. Serena Esposito, Referee, Politecnico di Torino
Prof. Gianluca Landi, Referee, Istituto di ricerca sulla combustione
Prof. Nunzio Russo, Referee, Politecnico di Torino
Prof. Onofrio Scialdone, Referee, Università degli studi di Palermo

Politecnico di Torino
November 2019

I hereby declare that, the contents and organisation of this dissertation constitute my own original work and does not compromise in any way the rights of third parties, including those relating to the security of personal data.

………………………………......
Eduard Alexandru Morosanu
Turin, November 15, 2019

Summary

According to the Intergovernmental Panel on Climate Change (IPCC), human activity is responsible for climate change mainly due to the emission of greenhouse gasses from fossil fuel usage. After the Kyoto protocol commitment, many climate change mitigation policies have been promulgated to reduce anthropogenic greenhouse gas emissions in the EU and incentives were given to install renewable power plants (e.g. wind or solar) to reduce the dependency on fossil fuels. Renewable energy sources (RES) have a fluctuating and intermittent characteristic (daily or seasonal) with peak production generally not matching the demand. As the adoption of RES grows in the electricity power source scenario, balancing of the electric grid without modulating the RES power plant is needed. Different technologies are available and under study for this purpose: flywheels, supercapacitors, batteries, compressed air storage, pumped hydroelectric storage, power-to-fuels (gas or liquid).

Power to Gas (PtG) appears to be a promising solution in converting renewable electricity in an energy carrier. Water electrolysis is used to convert electricity into hydrogen, which unfortunately presents some drawbacks as low energy density, steel embrittlement and challenges in storage/transportation. On the other hand, natural gas has a well-developed distribution grid and mature applications. Therefore, the most feasible solution is to further convert hydrogen in a substitute natural gas (SNG) compliant with the natural gas grid specifications. SNG can be produced by mixing hydrogen with carbon dioxide to carry out the Sabatier reaction.

The objective of this thesis was firstly to perform the process modelling of a power to liquefied methane system. The main units of the plant are the electrolyser, CO_2 capture from air, methanation unit, gas separation unit and the liquefaction unit. In this part the sizing and design of the separation system and liquefaction system was carried out in detail. Furthermore, the energy analysis of the system was carried. An efficiency of 46% $_{(HHV\ basis)}$ could be reached with a mild heat integration between the methanation unit and the CO_2 capturing unit. The main energy losses/consumptions are due to the direct air capture (20%), the electrolyser (19%) and the methanation unit (8%). The liquefaction process, a well-known energy intensive process, has an a less than 2 % energy impact in this case.

The aging of a commercial nickel-based catalyst was studied in process relevant conditions in terms of temperature, pressure and feed gas composition. The feed gas composition was determined through the process modelling of the gas separation subsystem. The separation unit contains recycle streams and therefore methane is expected in the reactor feed stream. Through 100 h long aging tests it was determined that the catalyst loses performance at temperature above 350 °C with a slow and gradual activity loss. The cause of the catalyst activity decay was individuated by employing different catalyst characterisation techniques. Through temperature programmed combustion (TPC) it was excluded carbon deposition as a possible cause of deactivation. Using X-ray diffractometry phase change of the nickel active metal was excluded as a possible cause of aging. The surface area analysis revealed a huge total area decrease that can only be caused by the sintering of the alumina support. A kinetic analysis was performed on a fresh and aged sample. The activation energy does not change between the samples meaning that there is no change in the reaction mechanism. Furthermore, a very good correlation was found between the ratio of the surface areas and the preexponential factors of the rate equation for the fresh and aged samples.

In order to correctly design a reliable methanation reactor it is essential to have a kinetic model that includes also the aging kinetics. For this purpose, a second set of experiments was carried out, in order to determine the intrinsic kinetics of the catalyst. The kinetic parameters of a Langmuir–Hinshelwood–Hougen–Watson (LHHW) type kinetic model were identified by using a nonlinear regression analysis. Subsequently, a power law aging model was proposed to consider the performance loss in time. Thus, a complete description of the catalyst behaviour both in terms of operating conditions and time on stream.

Finally, a multitube methanation reactor was developed in order to understand the effects of the operating conditions (temperature, pressure, space velocity) and the geometry on the temperature profiles and performance. An aging law was used in the model in order to consider the aging effect on the conversion rate. It was determined that to manage the declining performance caused by aging it is enough to adjust the operating temperature and pressure of the system to restore the initial conversion rates.

v

Acknowledgment

Contents

List of Tables

List of Figures

XIV

Chapter 1

Introduction

1.1 General introduction

Economic and population growth in the industrial era has led to a large increase of anthropogenic greenhouse gas emissions, now higher than ever. As a matter of fact, such high quantity of atmospheric concentrations of carbon dioxide, methane and nitrous oxide has never been recorded in at least the last 800,000 years. Their effects have impacted the climate system and it is extremely likely that they are the dominant cause of the observed warming since the mid-20th century. About 40% of the total anthropogenic CO_2 emissions up until now have remained in the atmosphere while the rest was stored in plants, soils and in the ocean, removing it from the atmosphere.

According to the Intergovernmental Panel on Climate Change (IPCC), human activity is responsible for climate change mainly due to the emission of greenhouse gasses from fossil fuel usage[1]. Despite of climate change mitigation policies, between 2000 and 2010 the greenhouse gas (GHG) emissions have increased sharper than the period from 1970 to 2000 (Figure 1-1). About 78% of the total GHG emissions increase in the considered period is due fossil fuel combustion and industrial processes, driven by population and in particular economic growth. Population size, economic activity, lifestyle, energy use, land use patterns, technology and climate policy drive anthropogenic GHG emissions.
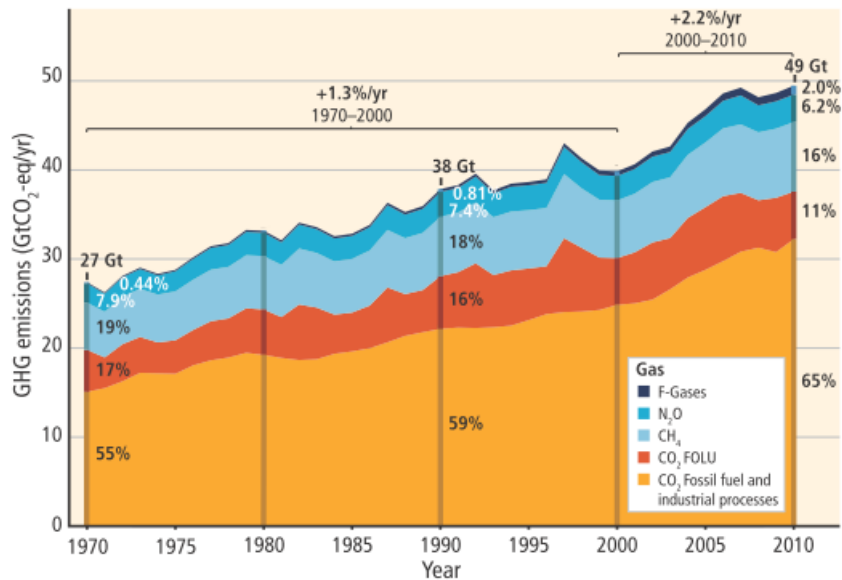
Figure 1-1: Total annual anthropogenic GHG emissions by gases 1970–2010. CO2 from fossil fuel combustion and industrial processes; CO2 from Forestry and Other Land Use (FOLU); methane (CH4); nitrous oxide (N2O); fluorinated gases covered under the Kyoto Protocol (F-gases)[1]

The forecasted mean global surface temperature rise according to the IPCC predictions could reach an increase up to 4.6°C in the worst-case scenario by the end of the 21st century. Furthermore, the artic regions will warmup faster than the rest of the world (Figure 1-2). It is virtually certain that there will be more frequent hot and fewer cold temperature extremes over most land areas on daily and seasonal timescales, as global mean surface temperature increases. It is very likely that heat waves will occur with a higher frequency and long-lasting. Occasional cold winter extremes will also occur.
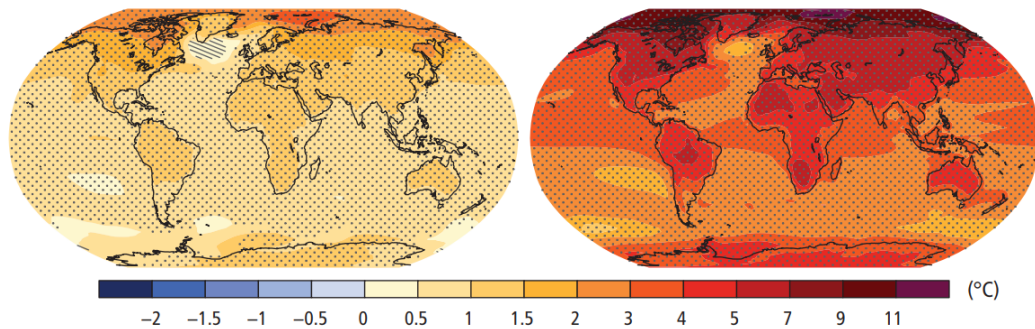
Figure 1-2: Change in average surface temperature (1986−2005 to 2081−2100)[1]

Continued emissions of GHG will cause further warming and long-lasting changes in the climate system, with severe and irreversible impacts for people and ecosystems. The Representative Concentration Pathways (RCPs) are used for making projections of greenhouse gas emissions, atmospheric concentrations, air pollutant emissions and land use, that vary over a wide range, depending on both socio-economic development and climate policy. The risks related to climate change can be reduced and managed with complementary strategies of adaptation and mitigation, designing properly climate policies, that are influenced by organizations perceive risks.

2

For this reason, in 1997 during the United Nations Framework Convention on Climate Change the Kyoto Protocol has been stipulated. It is an international agreement which commits its parties by setting internationally binding emission reduction targets under the principle of "common but differentiated responsibilities". Developed countries are mostly burdened by the Protocol because it is thought that more than 150 years of industrial activity are the main responsible for the current high levels of emissions in the atmosphere.

The greenhouse gases (GHG) to reduce are:

➤ Carbon dioxide (CO_2);
➤ Methane (CH_4);
➤ Nitrous oxide (N_2O);
➤ Hydrofluorocarbons (HFCs);
➤ Perfluorocarbons (PFCs);
➤ Sulphur hexafluoride (SF_6).

The maximum amount of emissions is measured as the equivalent in carbon dioxide.

From 2008 to 2012, the first commitment period, 37 industrialized countries and the European Community pledged to reduce GHG emissions to an average of 5% against 1990 levels, that is the reference year. In the second commitment period, from 2013 to 2020, the parties, different from the first period, committed to decrease emissions of at least 18% below 1990 levels. The Kyoto Protocol has the scope to assist countries in adapting to the effects of climate change by means of facilitating the development and deployment of technologies able to mitigate the emissions. For this reason, the Adaptation Fund was established to finance projects and programs in developing countries, parties of the Kyoto Protocol.

Going forward in time, in 2016, 187 countries of 197 belonging to United Nations Framework Convention on Climate Change (UNFCCC) ratified the Paris Agreement. This Agreement aims to combat climate change by intensifying the actions and investments needed for a sustainable low carbon future.

After the Kyoto protocol commitment, many climate change mitigation policies have been promulgated to reduce anthropogenic greenhouse gas emissions in the EU and incentives were given to install renewable power plants (e.g. wind or solar) to reduce the dependency on fossil fuels[2]. Nowadays, the development of non-fossil energy is leading to an increasing penetration of renewable energy sources (RES)[3]. According to the International Energy Agency (IEA) energy outlook the adoption of RES will grow in the electricity power source[4]. IEA estimates that renewable installed capacity for electric production will represent 42% of the overall capacity and will generate 33% of the total electricity over the period 2012 – 2040. Precisely, between 2014 and 2015 there was a decrease in electricity production from coal and oil, while electricity production from natural gas and RES, as wind and solar, increased. In 2015, much of the newly installed electric capacity in Europe came from RES:

wind power was the technology with the highest installation rate followed by solar PV [6].
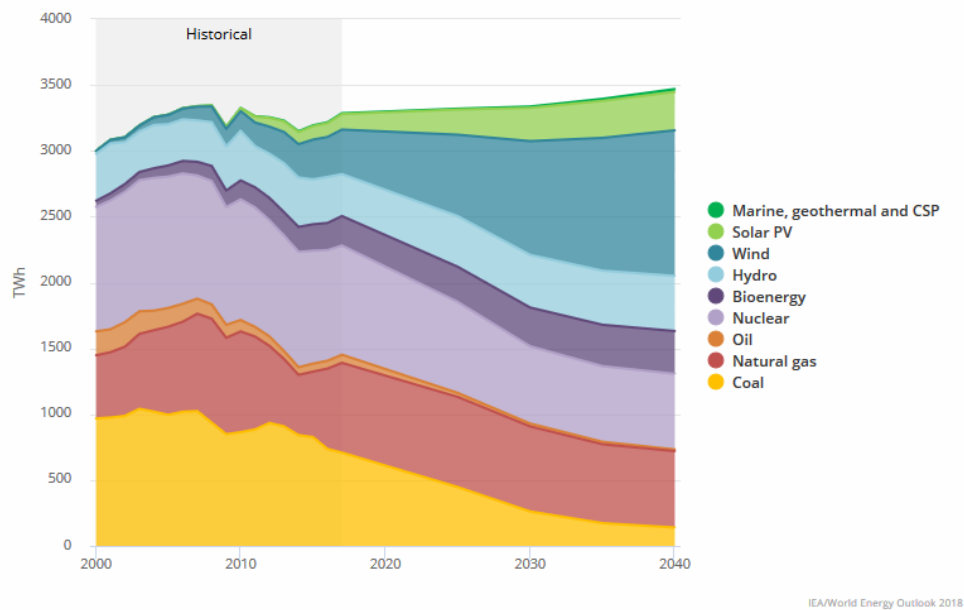
Figure 1-3 New Policies Scenario (NPS): Incorporates existing energy policies as well as an assessment of the results likely to stem from the implementation of announced policy intentions[4].

Renewable energy sources (RES) have a fluctuating and intermittent characteristic (daily or seasonal) with peak production generally not matching the demand [5]. In fact, the major inconvenient of the RESs is that their fluctuation are independent from the end-user demand. Furthermore, also users power consumption during the day is characterized by inconsistency and fluctuation, meaning that minimum consumption is closely half of a maximum peak. The ratio between peak and average power levels of the end-user demand often reaches a value of 10 [6]. Looking at Figure 4, it is shown a future scenario for a case study in Germany in 2050. The scenario is based only on RESs, both solar and wind. Photovoltaic generation prevails in the south of the state, while wind power overcomes in the north. The wind power production is distinguished by a more uniform power generation and lower oscillation frequency compared to photovoltaic generation. During the day, the largest contribution to energy production is due to the solar energy source, that has a high frequency of oscillation. During the night, only wind power generation is present. These features give to the electrical residual profile a high oscillation frequency with surplus spikes very intense sometimes. Furthermore, the electric load profile has a weekly periodicity as well as a seasonal trend, which shows photovoltaic intense spikes during summer and mostly wind power during winter, due to weather conditions during different seasons [7]. Balancing of the electric grid without resorting to modulation of the RES power plant is needed.
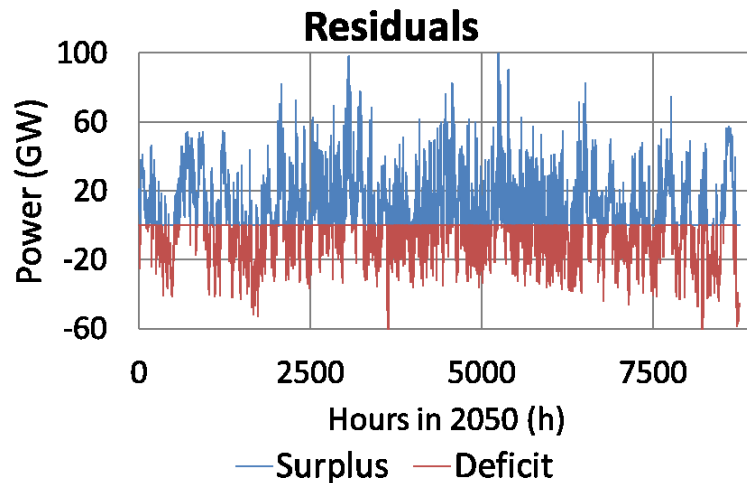
Figure 1-4: Example of energy net electricity residuals for Germany in 2050[7]

Today one of the solutions in balancing the electric grid is by electricity curtailment. As the renewable share in electricity production mix will rise the curtailment will be done on these sources as well. The consequence is that low environmental impact electricity will be wasted. It is clear that some kind of electricity storage technology, that stores electricity during surplus periods and returns it to the grid when required, is fundamental. In the next section some electricity storage technologies are presented and discussed.

1.2   Energy storage technologies

At present, the production of electricity is highly centralized and often far away from end-users. In order to manage the load levelling, predictions are based on daily and seasonal needs, but also, when production is not sufficient, on the contribution of RES. Delocalized electricity production and fluctuating energy sources, increase the difficulty of stabilizing the power network. A solution could be to generate the energy, transmit it, convert it, and then store it if need. Generally electricity storage requires bulky and costly equipment[6]. For this reason, the management of intermittent RES and their integration with the electric grid is not simple because higher integration costs may occur as their penetration level increases. The difficulty in grid management caused by sudden and fluctuating RES availability should be solved in order to encourage a widespread diffusion of wind and solar energy as primary energy sources. A key challenge can be represented by the need for a high storage capacity [8]. These types of technologies compose an integral and indispensable part of a reliable and effective renewable generation unit [9].

Different technologies are available and under study for this purpose: flywheels, supercapacitors, batteries[10], compressed air storage[11], pumped hydroelectric storage[12], power-to-fuels (gas[13] or liquid[14]). These solutions have been extensively reviewed in literature along with their advantages and drawbacks[6], [15]–[17]. The basic mechanism under all these energy storage technologies is to transform electricity into another energy carrier and to

transform it back when need. All forms of energy (mechanical, chemical, and thermal) can be considered convenient for the storage. The types of the storage technologies are function of applications and needs, that answer to specific technical and economic criteria.

According to their applications, the techniques can be divided into four categories:

> Low-power application. They can be used in isolated areas, essentially to feed transducers and emergency terminals.
> Medium-power application. For example, in isolated areas, specific techniques can supply energy to individual electrical systems or a town.
> Network connection application with peak levelling. Storage systems decouple synchronization between power generation and consumption. A typical application is load levelling. In this case during off-peak hours (low energy cost) energy is stored up and during peak hours (high energy cost) the stored energy is used.
> Power-quality control applications. Stored energy is only used for a few seconds or less to ensure the quality of power delivered.

In the first two categories are present small-scale systems where the energy could be stored as kinetic energy (flywheel), chemical energy, compressed air, hydrogen (fuel cells), or in supercapacitors or superconductors. In the large-scale systems belonging to three and four categories, the energy could be stored as gravitational energy (hydraulic systems), thermal energy (sensible, latent), chemical energy (accumulators, flow batteries), or compressed air (or coupled with liquid or natural gas storage) [6].
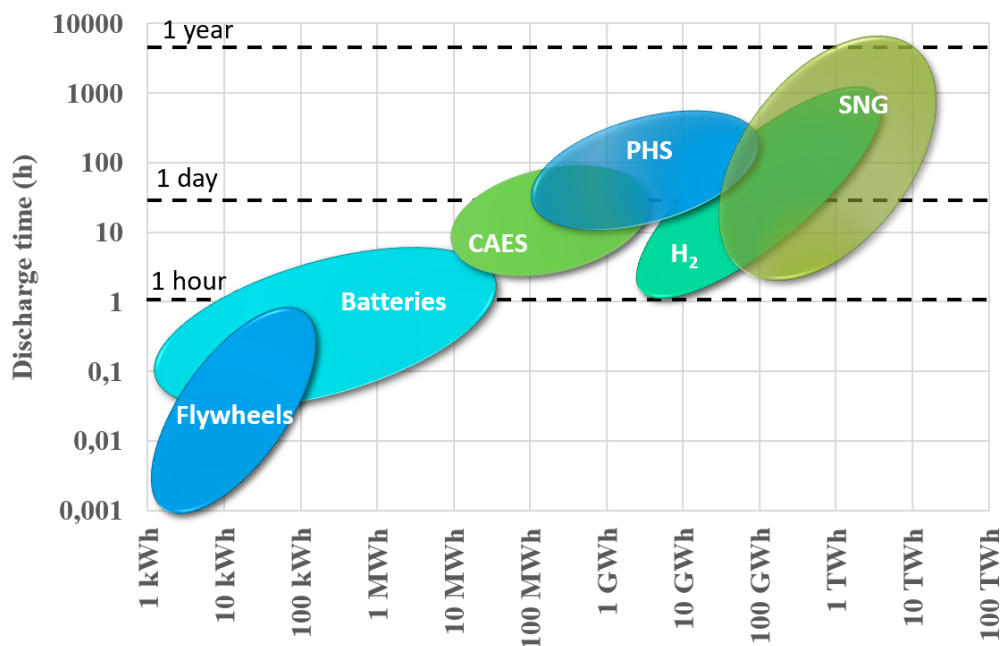
Figure 1-5: Discharge time and storage capacity of different electricity storage systems based technical and economical evaluations [18]

Pumped hydroelectricity is the dominant mean for the electricity storage, but the potential of this technology is limited by the topography of the region where it is installed. Compressed-air storage seems to be an alternative, but it requires large volumes for the energy storage. Batteries represent a future perspective for the electrochemical energy storage, even though this technology is still characterized by low capacity and degradation challenges. In order to store large amounts of surplus electricity for long periods and to balance seasonally RES electric production, chemical storage/conversion in synthetic fuels might represent a viable alternative [8].

1.2.1 Pumped hydroelectric (PHS)

Pumped hydroelectricity storage is a technique of storing and producing electricity by moving water between reservoirs at different elevations. The operating principle is divided in two phases, according to the energy demand. In the first phase, during periods when demand is low, the stations pump the water from the lower reservoir to the upper reservoir using electricity. In the second phase, when demand is very high, the water flows out of the upper reservoir and starts the turbines to generate high-value electricity for peak hours. Abandoned mines are used as the lower reservoir, but many PHS use the height difference between two natural bodies of water or artificial reservoirs[9].
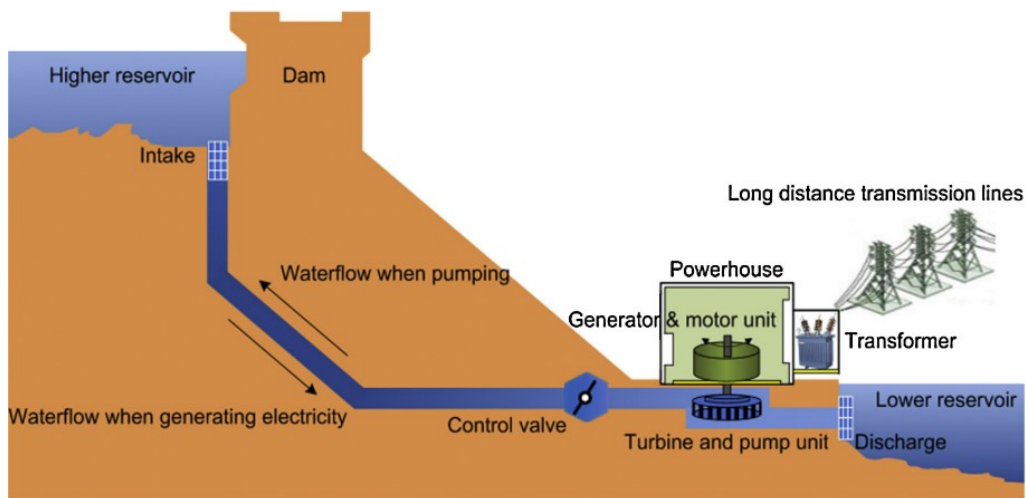
Figure 1-6: Pumped hydroelectric storage

The energy stored in a PHS is proportional, by means of ρ (density of water) and g (acceleration due to gravity), to the product of volume of water (V), and the difference in height between upper and lower reservoirs ($H_{upper} - H_{lower}$), as shown in the following equation.

$$E = \rho g V (H_{upper} - H_{lower}) \qquad (1\text{-}1)$$

For example, a mass of 1 ton falling 100 m generates 0.272 kWh [6]. Consequently, it is possible to store a large energy quantity through both a big volume of water, that means a large body of water reservoir, and a huge difference between the two heights [5].

In PHS, reversible turbine/generator assemblies that act as pump and turbine are used. In production mode, the reversible turbine feeds produced power to the grid. On the contrary, in storage mode, electricity from an external source powers the pumps. The round-trip efficiency (RTE) is calculated dividing PHS energy output (from generation) by the recorded energy input (for pumping), as shown in the equation.

$$RTE = \frac{E_{out}}{E_{in}} \qquad (1\text{-}2)$$

RTE is also called AC/AC efficiency and takes values lower than 1 due to both hydraulic, for example evaporation losses from the exposed water surface, and equipment-related losses (pump, turbine, generator, motor and transformer). Typical RTE range is between 65 and 85%, depending on the technical characteristics of the PHS and the expected lifetime is of 40-60 years [19].

PHS is generally distinguished in two different types. The first one is the "pure PHS" (also known as "closed-loop" PHS), that refers to stations not receiving natural inflows, because they are located far from streams and which scope is purely serving energy storage purposes. The second one is "pump-back" PHS (also known as "mixed" PHS), that utilizes both stored water and natural inflows to produce electricity and it is similar to conventional hydropower technology, with the additional peculiarity of storage [19].

The main advantage of this technology is that the energy is readily available, because the power of water is a highly concentrated renewable energy source.

This technique is currently the most cost-effective and most used for high-power applications, because it levels out load variations on the power grid. Indeed, PHS allows to thermal power stations (coal-fired plants and nuclear plants) to provide base-load electricity, reducing the need of use costly fuels to supply peak demand. Furthermore, pumped storage plants are faster than thermal plants in responding to sudden changes in electrical demand [9].

More than 99% of worldwide bulk storage capacity is provided by PHS and it contributes to about 3% of global generation capacity. As the matter of fact, since first use in Italy and Switzerland in the 1890s and the first large-scale application in the USA in 1929, more than 200 PHS units worldwide provide 100 GW of generation capacity [15].

Nevertheless, the main weakness of this technology is the need for a site with different water elevations. On the other side, long lead time, typically a decade, a high cost for construction artificial reservoirs and environmental issues, such as deforestation of the land where the reservoir will be found, are constraints in the deployment of PHS [15]. Nowadays, innovative research has led to some systems that could reduce the environmental impacts of PHS technologies, such as sub-sea PHS, seawater PHS, and variable-speed PHS [5].

1.2.2 Compressed air energy storage (CAES)

Compressed air energy storage (CAES) is a derivation of basic gas turbine (GT) technology, that makes it readily available and reliable. For this reason,

CAES has a high economic feasibility, that could contribute to creating a flexible energy system coupled with plants using RES, especially wind power [11]. Together with PHS, CAES is the only other commercial large-scale system that provides energy capacities of around 50–300 MW, ready to be used combined with entire power plants. Since the losses are very small, the storage period is the longest, more than a year [15].

The basic installation, as shown in Fig. 1-7, is composed by 5 components:

1. The motor/generator used to provide electricity to the compressor or turbine trains.
2. The air compressor (two or more stages), intercoolers and aftercoolers to achieve economy of compression.
3. The heat exchangers coupled with high- and low-pressure turbines.
4. Equipment control center for operating the combustion turbine, with a compressor.
5. Auxiliary equipment for fuel storage and handling and to support various heat exchangers required [9].

Nearly two-thirds of the available power is used by a power plant with a standard gas turbine to compress the combustion air. Separating the processes in time, it is possible to use electrical power during off-peak hours (storage hours) in order to compress the air, typically at 4-8 MPa, and store it [6]. In order of using in the best way the storage space available, the air is cooled prior to injection [9]. During peak hours (retrieval hours), to extract the stored energy, the compressed air is heated by the heat exchanger and then expanded through a high-pressure turbine. Some of air from high turbine is mix with fuel in a combustion chamber before feeding it into the low turbines [15]. Residual heat from the smoke is recovered and used to heat the air. At high pressures (40–70 bars) and at near-ambient temperatures, compressed air energy storage is achieved. This means less volume and a smaller storage reservoir. This operation can produce three times the power for the same fuel consumption.
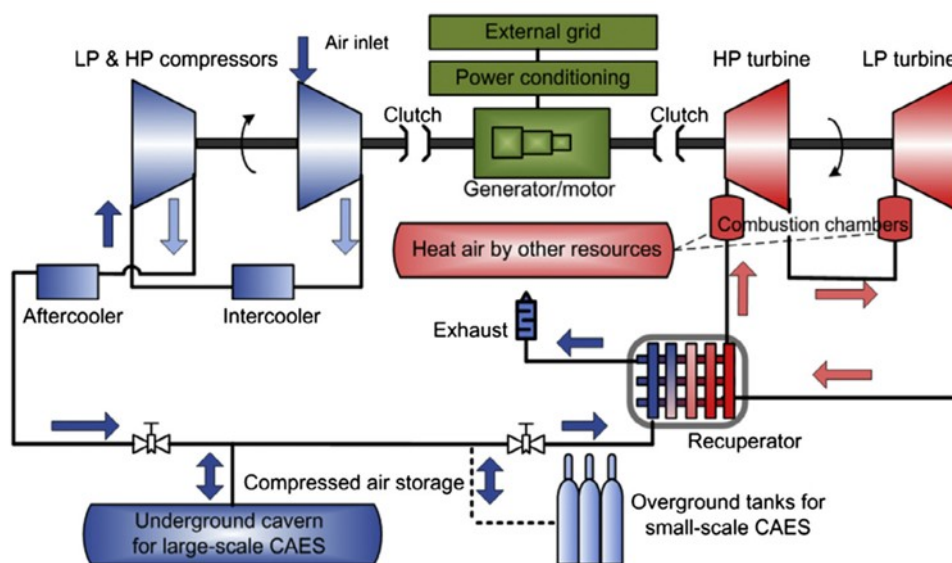
Figure 1-7: Compressed air energy storage

In order to store compressed air, the best options to consider are large caverns made of high-quality rock deep in the ground, ancient salt mines, or underground natural gas storage caves. The reason is that they benefit from geostatic pressure, which facilitates the containment of the air mass.

Rock caverns, created by excavating solid rock formations, are about 60% more expensive to mine than salt caverns, because are composed by solution of salt formations. Hence, aquifer storage is the least expensive method and the most used [9]. For geological criteria, it's possible to compress and store the air in underground, with high pressure piping (20–100 bars). This method makes the system easier to operate. Another system is the CAS, compressed air storage in vessels, fabricated high-pressure tanks. However, to manufacture these high-pressure tanks at a feasible cost now is not possible [9].

The RTE (round-trip efficiency) of CAES is the range of 70 - 89% and the expected life time is 20–40 years, features that make it a suitable option for large-scale storage applications [5].

At present, there are two CAES plants in the world for a total of 400 MW of capacity. The first is in Huntorf (Germany, 1978) with a capacity of 290 MW for 2 h. This system, with a demonstrated 90% availability and 99% starting reliability, was initially built to support a nuclear plant, but now is used for grid support 3 h/day. The second CAES plant was built in 1991, in McIntosh (USA), with a 110 MW capacity for 26 h. Using a recuperator, the fuel consumption is reduced of approximately 25% compared to the Huntorf plant [20].

The main advantages of CAES are the long energy storage period, low capital costs, high efficiency and emissions of greenhouse gases lower than in normal gas plants. The main drawback is probably the geological structure availability, which limits the usability of this storage method [9].

1.2.3 Flywheels

For thousands of years, flywheels have been used to store energy. Currently, flywheels are a suitable way to stabilise a small-scale wind turbine output on an island or to mitigate the cloud cover effects on solar photovoltaic by preventing voltage disturbances [20].

A flywheel is a mass rotating about an axis, which can store energy in the form of rotational energy, in the angular momentum of the spinning mass [9]. During charge, a motor turns the flywheel, that stores mechanically energy, while during discharge the same motor acts as a electricity generator led by the kinetic energy of the flywheel, that slows down via a decelerating torque [15]. The stored energy depends on its rotational velocity and its moment of inertia: the faster a flywheel rotates the more energy it stores during the charge [9]. A typical structure consists of a cylindric rotor, a high vacuum containment system to minimise windage losses and maintain good performances, a magnetic low friction bearing assembly and a power conversion and control system to store energy or generate the electricity on demand. The flywheel systems can be classified into two categories: conventional metal rotor systems and high-speed

composite systems [15]. The first systems operate with low speed, up to 6000 rpm, provided by motor, achieving specific energy of around 5 Wh/kg and usually are made of steel rotors and conventional bearings [9]. Since they have relatively large standby losses, they are typically used for short-term (10–100 s) and medium/high load applications [15]. The second flywheel systems work with high speed, up to 50,000 rpm, and can achieve specific energy of 100 Wh/kg. Their structure is made of relatively low-density composite materials with ultra-low friction bearing assemblies, such as the container that is evacuated or helium filled to reduce aerodynamic losses and rotor stresses. The low pressure is also useful to reduce self-discharge losses [9].
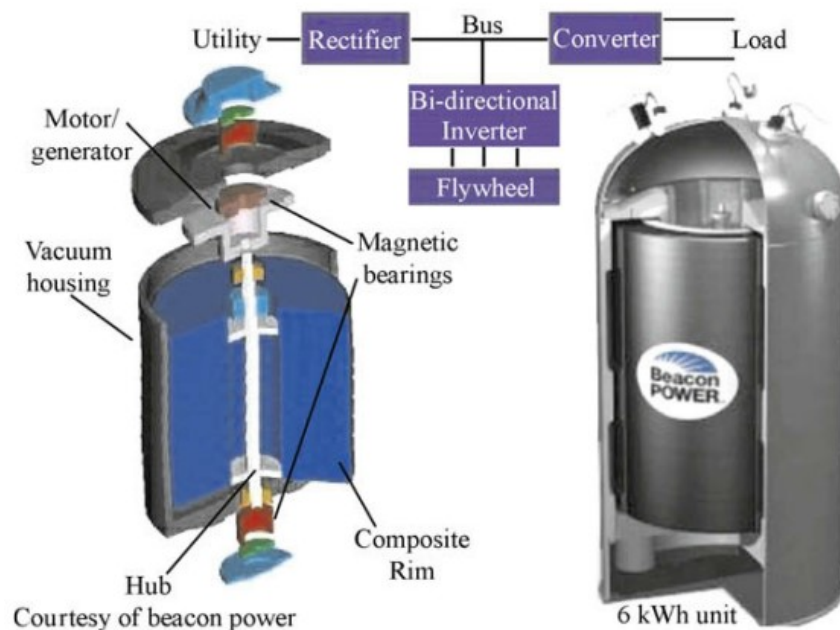
Figure 1-8: Flywheel system

The flywheel is a promising technology: its life is about 15–20 years with a long capable of providing from 10,000 to 100,000 of full charge–discharge cycles, and high efficiency of 90–95%, despite self-discharge rate is between 55% and 100%/day [20]. As a matter of fact, the instantaneous efficiency of the system corresponds to 85%, but the overall efficiency would drop to 78% after 5 h, and 45% after one day, due to friction losses. Long-term storage with this type of apparatus is therefore not foreseeable. Flywheels are more useful to produce energy in isolated areas, from a practical point of view [16]. High power/short duration applications (e.g. 100 s of kW/10 s of seconds) are the most common ones for flywheels. The main drawbacks consist in the relatively short duration, high frictional loss (windage) for the conventional metal rotor systems and the low energy density restrain [15].

1.2.4 Batteries

The oldest form of electricity storage is the rechargeable/secondary battery, which stores electricity in the form of chemical energy [15], and it is widely used in electrical energy storage technologies in industry and in daily life [17]. Developments in the battery technology have been done, some of battery types are available commercially while some others are still in the experimental stage [10].

Depending on the technology, the battery has a round trip efficiency (RTE) between 60% and 90% and can offer a very rapid response, within 20 ms, to load changes, as well as accepting co-generated and/or third-party power, thus improving the system stability [15]. The features that characterize a battery are efficiency, life span (number of cycles), operating temperature, depth of discharge, self-discharge and energy density. The Depth of Discharge (DoD) measures the discharge entity and it influences the battery lifetime, because batteries are generally not discharged completely. The self-discharge is important because estimates the rate of discharge when the battery is stored in a shelf and loses a part of its electrical capacity. Based on its energy and power capacities, that usually are not independent and are fixed during the battery design, a battery can be choose for different applications, such as power quality, energy management, ride-through power and transportation systems [10], [17]. Deep cycle batteries are used in power system applications. They have an energy capacity ranging from 17 to 40 MWh and efficiencies of about 70–80% [10].

The main advantages of this technology concern the very low standby losses as well as the fuel flexibility and the high energy efficiency. Because of the short lead times (roughly within 12 months) and the technology's modularity, a construction of a secondary battery is eased [15]. Furthermore, it is possible to install it flexibly, either housed inside a building or close to the facilities where needed [17]. On the contrary, implementing a large-scale utility battery storage is difficult because of low energy densities, small power capacity, high maintenance costs, a short cycle life and a limited discharge capability. In addition, most batteries contain toxic materials that must be correctly disposed in order to not have an ecological impact on the environment [15].

The operating principle of a battery consists in considering the electrochemical reactions that happen in the cells, where chemical energy is converted to electrical energy and vice versa [10]. The reactions involve the transfer of electrons between two electrodes plunged into an electrolyte, through an external electric circuit/load connected to the cell terminal [9]. Connecting several cells in series or in parallel or both, the required voltage or current levels can be obtained [10]. Each cell is composed by 4 elements:

1. The anode or negative electrode which provides electrons to the load oxidizing itself during the electrochemical reaction.
2. The cathode or positive electrode is reduced accepting electrons.
3. The electrolyte, which can be liquid, paste, or solid, allows the transfer of electrons between the anode and the cathode.
4. The separators between the two electrodes for electrical insulation [9].

During discharge, electrochemical reactions occur at the two electrodes and the result is a flow of electrons through an external circuit, linked to cell. Since the reactions are reversible, applying an external voltage across the electrodes the battery can be recharged [15].

Below the most important types of battery will be presented.

> Lead acid. The cathode is made of PbO_2 and the anode is made of sponge Pb, separated by a micro-porous material and immersed in an aqueous sulfuric acid electrolyte [10]. During the discharged, $PbSO_4$ is produced both at the two electrodes, while the electrolyte changes to water [5]. These batteries have fast response times with small daily self-discharge rates (<0.3%) and relatively high cycle efficiencies (63-90%) [17].

> Flooded type. During discharge, the PbO_2 on the cathode is reduced to lead oxide. Then it reacts with sulfuric acid solution to form lead sulfate. The sponge Pb on the anode is oxidized to lead ions, that reacts with sulfuric acid to form lead sulfate. The reaction generates electricity and during charging it is reversed [10].

> Valve regulated (VRLA) type. The same basic electrochemical technology of flooded lead-acid batteries is used, except that these batteries are sealed with a pressure regulating valve and the acid electrolyte is immobilized [10].

> Sodium sulphur (NaS). A NaS battery consists of a solid beta alumina ceramic electrolyte that separates a molten sulfur cathode and molten sodium anode. Only the positive sodium ions are allowed to go through the electrolyte and to combine with the sulfur to form sodium polysulfides. The voltage produced in the discharge is about 2 V and the operative temperature is about 300°C to allow this process [10].

Flow batteries are a two-electrolyte system. The chemical compounds used for energy storage are in liquid state, in solution with the electrolyte. The limitations of standard electrochemical accumulators (lead–acid or nickel–cadmium for example) are overcome because the electrochemical reactions create solid compounds that are stored directly on the electrodes on which they form. Since it is limited-mass system, also the capacity is limited. In the battery, the electrolyte uses bromine as a central element: with zinc (ZnBr), sodium (NaBr), vanadium (VBr) and sodium polysulfide. The electrochemical reaction through a membrane in the cell can be in both directions (charge–discharge). Using large reservoirs and coupling many cells, it is possible to store large quantities of energy and then release by pumping electrolyte into the reservoirs. The overall electricity storage efficiency is about 75%.
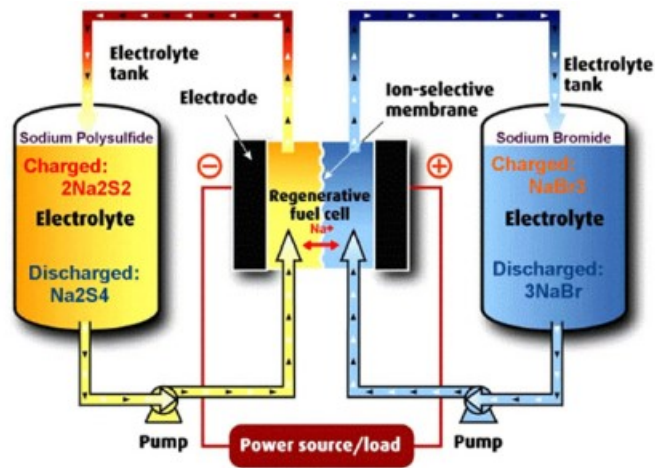
Figure 1-8: Illustration of a flow battery of type PSB (Polysulfide Bromide Battery).

1.2.5 Synthetic Fuels

Instead of storing electrical energy in a different kind of energy (chemical in batteries, kinetic in flywheels, compressed air in CAES or gravitational energy in PHS), the electricity from renewable sources could be employed to produce new synthetic fuels. The fuels can be made preferentially when an excess electricity supply from fluctuating and intermittent energy sources happens. This system could have the consequence of reducing the demand for energy storage systems that are designed to accept and return electric power, for instance pumped hydro storage, compressed air storage, batteries, etc [21]. The high energy density of these synthetic fuels allows to store the original renewable energy in the long-term [22].

The fuels provide energy in all artificial sectors, from industry to transportation, and the most important kind is hydrocarbon fuel. Its dominant feedstock for the transportation energy is petroleum, from which transportation fuels are manufactured. Nowadays, more sustainable potential alternatives are being studied in order to produce hydrocarbons from other feedstocks (fossil and biomass), as well as carbon-free energy carriers (such as hydrogen, batteries and ultracapacitors). Biofuels and fossil carbon derived synthetic fuels, such as coal derived liquid fuels, are studied as a direct replacement for petroleum-based hydrocarbons, but their sustainability depends largely on the source of the feedstock, in particular on the availability of carbon capture and storage technologies and sites. It is possible to produce similar hydrocarbons without using fossil fuels or biomass, through a non-biological process, that consumes renewable and/or nuclear energy in the form of heat, electricity, and/or sunlight, carbon dioxide and water. Initially, CO_2 from large industrial sources could be utilized, but, in the long term, the capture of CO_2 from the atmosphere will be necessary to enable a closed-loop hydrocarbon fuel cycle, as shown in Figure 1-9 [21].
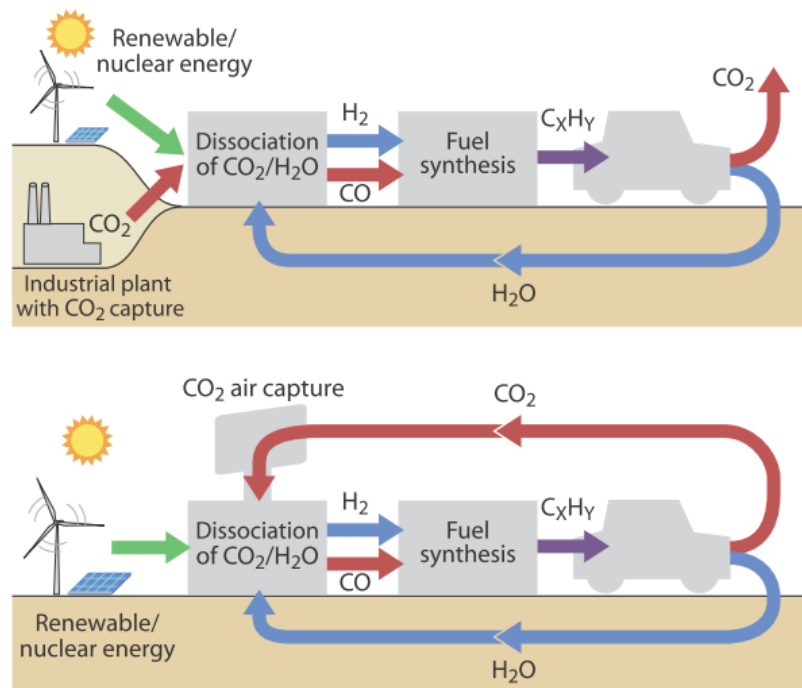
Figure 1-9: CO₂ -recycled synthetic fuel cycles.

The CO₂-recycled fuel cycle avoids the biomass intermediate product, which consumes a lot of resources to cultivate, such as land, water, fertilizer, and needs to be processed further to produce a fuel. The biofuel production would need more land than fuel production driven by photovoltaic, because even with low-efficiency solar panels the components would cover less than a tenth of the land area that is needed to grow typical biomass. Through this cycle, the competition with food agriculture and other important land uses would be avoided.

Compared to hydrogen as a fuel, CO₂-recycled fuels are a form of chemical storage of hydrogen combined with carbon. The production of such fuels would be analogous to hydrogen production, that could use a variety of sustainable resources, while distribution and consumption would use the existing hydrocarbon fuel-based infrastructure [21].

Many pathways are valid for the transformation of renewable energy into gaseous or liquid fuels through the combination with residual CO₂, as shown in Figure 1-10. Power-to-fuel processes can be promising systems which convert electricity into synthetic fuels. This technology makes possible the connection of electrical and gas networks in a single energy system, introducing high flexibility in the balance of the grid and allowing exchange in both directions [22]. Power-to-fuel could thus be applied for energy transport via the gas distribution grid, production of renewable fuels for heating and transport purposes, and production of renewable raw materials for the chemical industry [23].
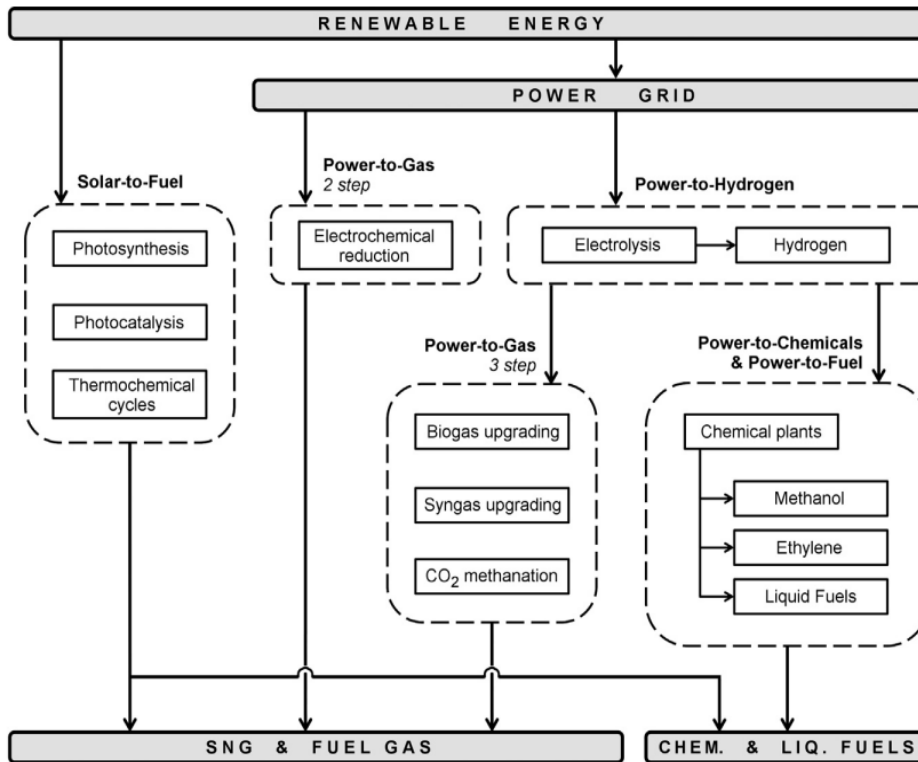
Figure 1-10: Renewable energy and CO_2 storage techniques.

A particular and rising power-to-fuel technology is the power-to-gas (PtG). The considered technology is a long-term energy storage option, especially suited for balancing seasonal energy fluctuations, in contrast to battery system. Whereas pumped hydropower plants have a limited potential due to the available of sites with appropriate geography, power-to-gas doesn't show geographical problems and, in combination with the existing gas infrastructure, offers a huge potential [23].

Possible synthetic fuels produced are:

➢ Hydrogen
➢ Methane
➢ Methanol/Dimethyl ether
➢ Gasoline, jet fuel and diesel by Fischer Tropsch process

For H_2 production, the power-to-gas system utilizes surplus electricity mainly from renewable sources to split water into hydrogen (H_2) and oxygen (O_2) in an electrolyser, by mean of electrolysis technology. The product H_2 can be transported via a hydrogen pipeline, but only a few pipelines exist in industrial regions, in fact they would need of the built-up of an area wide H_2 network. Currently, H_2 is primarily applied as a raw material in industrial processes such as materials processing, chemical manufacturing, and many other applications.

For CH_4 production, a further step in power-to-gas technology is the synthesis of H_2 and carbon dioxide CO_2 to methane CH_4 through methanation via the Sabatier reaction. The total efficiency decreases, but it could be advantageous in

16

terms of feeding the produced energy carrier into the gas distribution grid. As the matter of fact, in contrast to the case of H_2, there is not a limitation in amount in the injection of CH_4. The allowed volumetric fraction of H_2 in the gas distribution grid is different in each country (e.g., 5 vol% in Germany). With the methanation, power-to-gas technology also serves for utilization of CO_2 mainly emitted from industrial processes and power plants [23].

Methanol and derived dimethyl ether (DME) are also excellent transportation fuels. They can be utilised in internal combustion engines (ICE) and in direct oxidation methanol fuel cells (DMFC). From another point of view, methanol and DME are good starting materials for producing light olefins, such as ethylene and propylene, and afterward other derived hydrocarbon product. They are the result of the catalytic conversion of CO_2 with H_2 according to the following reaction:

$$CO_2 + 3H_2 \rightleftharpoons CH_3OH + H_2O \qquad (1\text{-}3)$$
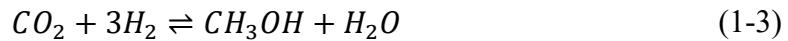
The methanol synthesis is an exothermic reaction that needs of significant quantity of energy. It is also possible to produce methanol from syngas containing CH_4. The process uses copper/zinc oxide-based catalysts, which are extremely active and selective in heterogeneous gas-phase [24].

Another type of synthetic liquid fuel can be obtained using the syngas, produced by Power-to-Gas technology, in the Fischer Tropsch (FT) process. Briefly, the basic idea considers the reverse water-gas shift reaction between H_2, from electrolysis, and captured CO_2, in order to have syngas. Then, via Fischer Tropsch synthesis, syngas is synthesized to liquid hydrocarbons (syncrude), mainly made of alkanes, alkenes, alcohols, carbonyls and carboxylic acids. The synthesis is an energy intense process with a wide variety of products, that must be separated and upgraded. The synthesis reaction is exothermic heterogeneous catalysed (Fe-based and Co-based catalysts) reaction, that can be led both into high temperature and low temperature. When the main products are alkenes or straight run fuels, high temperature FT synthesis is suitable, while low temperature FT is recommended with hydrocarbons products mainly in the range of liquid waxes [25].

Electrolysis technologies

The electrochemical splitting of water into hydrogen and oxygen by supplying electrical (and thermal) energy is given by the following overall reaction:

$$H_2O \xrightarrow[Electrolysis]{} H_2 + \frac{1}{2}O_2 \qquad (1\text{-}4)$$
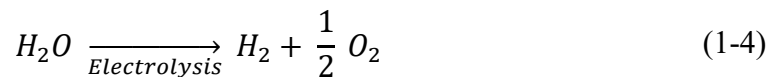
The heat of reaction gives the overall energy demand of reaction ΔH. ΔH can be partly supplied by heat ΔQ, partly provided electrically ΔG, change in Gibbs energy). The overall energy demand ΔH varies only slightly with temperature. Since the part of possible heat integration ΔQ rises with temperature, the minimum electrical demand ΔG must decrease increasing temperature. The main motivation of high temperature electrolysis, that is operated at 700–900 °C, is the possible high heat utilisation of internal losses, besides improved kinetics. Part of the heat demand corresponding to the latent heat of vaporisation is supplied by

feeding water vapour instead of liquid water, as it is the case for low temperature electrolysis (AEL, PEMEL). Thanks to ΔG, supplied electrically, the overall energy demand of the electrolysis reaction ΔH, including heat ΔQ, is obtained. Comparing steam electrolysis to liquid water electrolysis, the minimum electrical energy consumption can be reduced by the heat of evaporation of 41 kJ/mol at ambient pressure.

Thermoneutral voltage is the standard operation mode of high temperature electrolyser. In the cell, that operates at constant temperature, internal heat production is equalised by heat consumption of the electrolysis reaction. Low temperature electrolysers (AEL, PEMEL) operate above the thermoneutral voltage due to high internal losses or overvoltages, that means that cells requiring external cooling of the module to contrast the heating of the electrolysis [26].
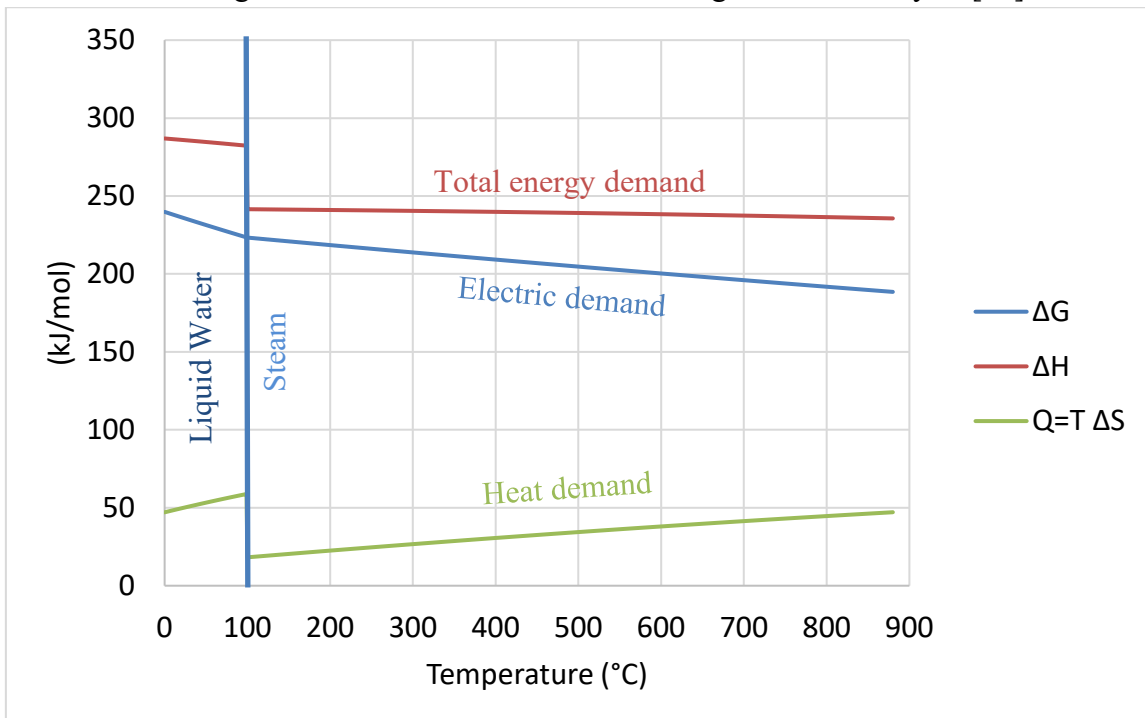
Figure 1-11: Specific energy demand at 1 bar versus temperature

Electrolysis technologies can be grouped into two main categories: low temperature and high temperature. Alkaline and PEM (proton exchange membrane) electrolyzers belong to the first type: their operating temperature usually stays in the range $50 - 80\,°C$. High temperature electrolysis through solid oxide electrolysis cells (SOEC) represents an alternative technology: in this case steam (instead of liquid water) electrolysis is carried out. By using SOEC, the reacting water should be vaporized in a separated device before the electrolysis section. Potential benefits of high temperature electrolysis (HTE) are summarized in the literature.

The SOEC operating temperature stays in the range between 700 and $900\,°C$. Reviews of materials and cell configuration are available in the open literature. Concerning the thermal balance of an SOEC stack, an interesting operating point is thermoneutral voltage: in this condition heat generated via irreversible

18

phenomena equals the thermal energy required for the endothermal steam reduction and the SOEC device can operate isothermally without energy supply/rejection. A deeper investigation of the thermodynamics of high temperature electrolysis can be found in the literature. The coupling between SOEC and methanation seems to be promising due to the use of reaction heat (coming from the methanation reaction) for steam production[8].

Collection and availability of carbon dioxide

Power-to-fuels systems require a carbon source for the fuel synthesis. Therefore, CO_2 availability must be considered as a key point for the feasibility of the process. Carbon dioxide can be collected from exhaust gas in industrial plants for iron/steel and cement production, fossil fuels power plants or refineries [27]. Another non-atmospheric CO_2 source is geothermal vents and geothermal power plants therefore release this stored CO_2 [21]. Industries can represent one of the largest stationary CO_2 sources in the world. However, sequestrated CO_2 should be upgraded in order to remove catalyst poisoning trace components such as sulphur [13]. The main concern is represented by the reduced process efficiency (implying increasing costs) related to the removal of CO_2 from the industries exhaust gases.

Diverse separation techniques can be useful for the separation of CO_2 from gas streams. Different physical and chemical processes including absorption into a liquid solution, adsorption onto suitable solids, cryogenic separation, and permeation through membranes are considered. Absorption/desorption processes using amine solution based, such as monoethanolamine (MEA) and diethanolamine (DEA), are some of the most widely employed for the separation of CO_2 from gas mixtures. The regeneration step requires high energy and limited loadings in amines, due to corrosion problems and amine degradation, are the major drawbacks [24].

CO_2 capture from air can be considered as a future perspective [21], especially considering the high purity of the sequestrated gas. However, at the present state carbon dioxide collection from air seems to be a very expensive process not feasible from an economic standpoint [28]. Removing CO_2 from air was first studied in the 1940s using an alkaline absorbent, such as KOH, $Ca(OH)_2$ and NaOH, that readily react with CO_2 to form carbonates. The, to release CO_2, the absorbent must then be regenerated electrically or thermally. Alternatively, a carbonate solution has been used to absorb CO_2 forming bicarbonate [21].

Biogas-to-biomethane upgrading ([29], [30]) can be also considered as carbon source: if electricity for electrolysis come from RES, the integration with CO_2 collection from biogas plants would lead to a fully renewable power-to-SNG pathway. Biogas is a gaseous mixture produced by methanogenic bacteria through anaerobic digestion of organic matter: it is mainly composed by CH_4 (50-70 vol.-%) and CO_2 (30-50 vol.-%), but there are also trace components as H_2S, water, ammonia, mercaptans, siloxanes etc. In Europe, there is a significant potential of CO_2 from biogas: in 2013 the overall European production was 13379 ktoe [31].

Biogas is usually used for combined heat and power production (i.e., via internal combustion engines), but it could be also directly injected into a methanation reactor after removing the trace components, which can lead to the catalysts poisoning. Alternatively, biogas can be upgraded to biomethane by removing the CO_2, which is the main sub-product of the process and it can be collected, eventually cleaned/purified (trace components may poison the methanation catalyst) and then made available for the methanation process.

1.3 Power to methane

Power to Gas (PtG) appears to be a promising solution in converting excess renewable electricity in an energy carrier. Water electrolysis is used to convert electricity into hydrogen, which unfortunately presents some drawbacks as low energy density, steel embrittlement and challenges in storage/transportation. On the other hand, natural gas has a well-developed distribution grid and mature applications. Therefore, the most feasible solution is to further convert hydrogen in a substitute natural gas (SNG) compliant with the natural gas grid specifications. SNG can be produced by mixing hydrogen with carbon dioxide to carry out the Sabatier reaction (1-1). This concept has also the advantage of recycling CO_2 and potentially preventing global warming[32], [33].

$$CO_2 + 4H_2 \rightleftharpoons CH_4 + 2H_2O \qquad \Delta H_{298K} = -164.9 \ kJ/mol \qquad (1\text{-}5)$$
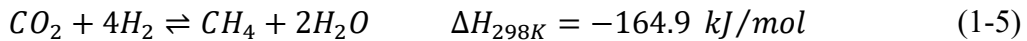
The main reaction that takes place in the methanation module (1-2). This is a well-known reaction that was discovered at the beginning of the 20th century by Paul Sabatier, from whom it takes its name. From a thermodynamic point of view, the reaction is favoured at low temperature and high pressure. In fact, from le Chatelier's principle, for an exothermic and mole reducing reaction operating in these conditions is favourable towards the products of the reaction.

$$CO_2 + 4H_2 \rightleftharpoons CH_4 + 2H_2O \qquad \begin{aligned} \Delta G_{298\,[K]} &= -113{,}2 \left[{kJ}/{mol} \right] \\ \Delta H_{298\,[K]} &= -165{,}0 \left[{kJ}/{mol} \right] \end{aligned} \qquad (1\text{-}6)$$
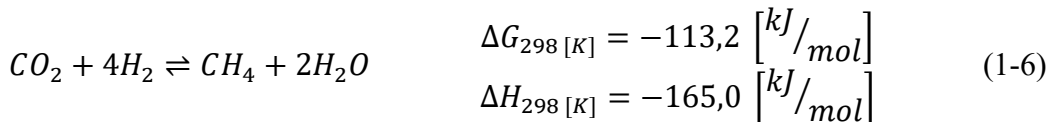
Other reactions that may occur that have been considered during the thermodynamic analysis are: carbon monoxide methanation (1-3) and water gas shift (1-5).

	$\Delta G_{298\,[K]} \left[{kJ}/{mol} \right]$	$\Delta H_{298\,[K]} \left[{kJ}/{mol} \right]$	
$CO + 3H_2 \rightleftharpoons CH_4 + H_2O$	$-141{,}8$	$-206{,}1$	(1-7)
$2CO + 2H_2 \rightleftharpoons CH_4 + CO_2$	$-170{,}4$	$-247{,}3$	(1-8)
$CO + H_2O \rightleftharpoons CO_2 + H_2$	$-28{,}6$	$-41{,}2$	(1-9)
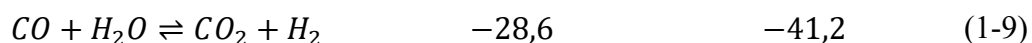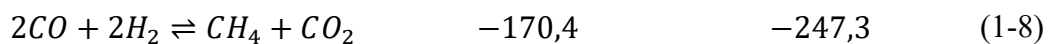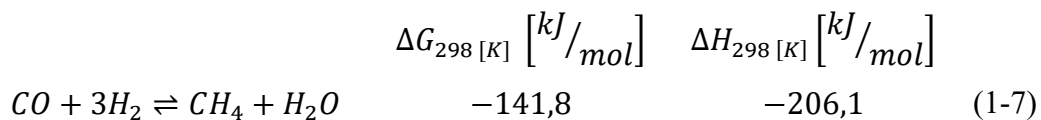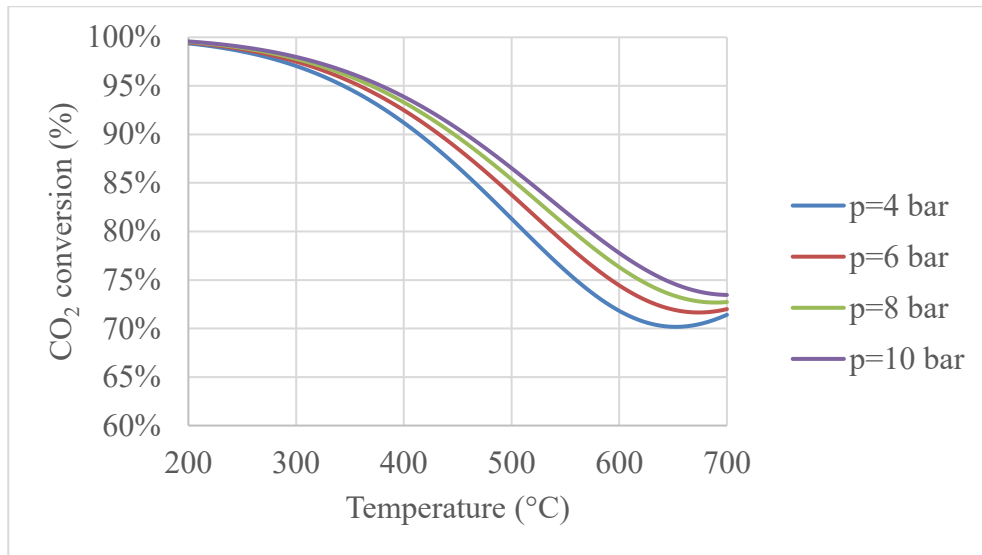
Figure 1-12: CO₂ conversion versus temperature at different total pressure for an H₂/CO₂=4
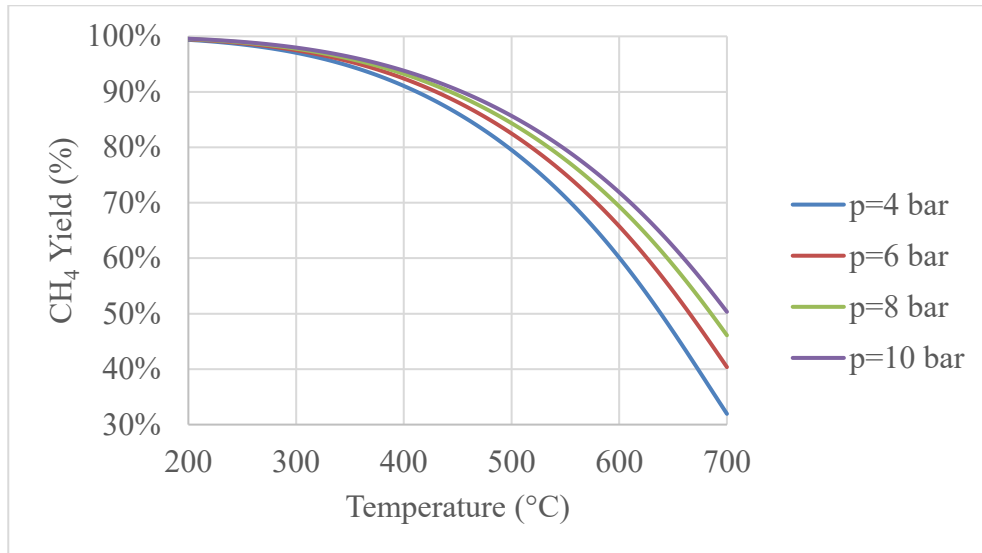
Figure 1-13: Methane Yield versus temperature at different total pressure for an H₂/CO₂=4

PtG has received a lot of interest from the scientific community and industry. The first large scale 6 MW_{el} PtG plant was built in Werlte (Germany) in the Audi e-gas project. The plant uses 3 alkaline water electrolysers of 2 MW each and isothermal fixed bed methanation reactors fed with CO_2 from a nearby biogas plant. The heat generated by the PtG plant is recovered in the biogas plant[22], [34]. Another project called HelmetH built a demo plant using high temperature steam electrolysis. The aim of the project is to demonstrate the high efficiency achievable by coupling the endothermic electrolysis with the exothermic methanation[35]. At least 25 demo projects using CO_2 methanation are reported in literature[22]. However, in none of the 25 demoes, liquefaction of the produced gas is performed. A PtG process using this solution can be deployed in remote areas (e.g. islands), regions not covered by the natural gas distribution grid and off-grid applications.

21

1.3.1 Catalysts for CO_2 methanation

A catalyst suitable for industrial use needs to meet certain cost, activity, selectivity, stability, recovery, reuse, and handling requirements [36]. Group 8, 9, 10 and 11 transition metals have been usually investigated as active compounds for catalytic CO_2 methanation. Nickel and ruthenium-based catalysts produce almost exclusively methane. Reviews of the several catalysts involved in methanation are available in the literature [37]–[39]. Nickel based catalysts are the most common studied for CO_2 methanation because of their high activity and low price [37]. The hydrogenation of carbon dioxide producing methane and carbon monoxide has been widely investigated over Ni/Al_2O_3, which represent a sort of baseline catalyst family for methanation reactions [40].

The support plays a crucial role on the activity, selectivity and stability [41], [42]. In order to improve the catalyst performance, addition of oxides to γ-Al_2O_3 is frequently reported: promoters as CeO_2 ([43], [44]), ZrO_2 ([45]) and TiO_2 ([46]) can enhance the reducibility and the metal dispersion [47]–[49]. Investigations on several composite oxides supported Ni-based catalysts showed superior performance if compared to standard Ni/γ-Al_2O_3 samples.

Another category of catalysts of great interest for methanation is represented by nickel-based hydrotalcites (HTLCs), which are constituted by mixed hydroxides of divalent/trivalent metals and have a layered structure. Calcination of HTLCs is an alternative to traditional chemical and physical methods to produce a wide variety of mixed metal oxide materials. The calcination progressively induces dehydration, de-hydroxylation, and loss of compensating anions and leads to acidic and basic mixed oxides with a high surface area [50]. HTLCs as catalyst precursors gained interest for their activity in carbon dioxide methanation [51]–[55].

Ru-based catalysts for carbon dioxide methanation have been widely studied ([56]–[58]). Ruthenium showed higher activity than nickel, but it is also more expensive. Other metals investigated for CO_2 methanation are rhodium, platinum, palladium, cobalt and magnesium [59]–[63].

1.3.2 Methanation concepts

Almost all technologies have been developed originally to convert the syngas produced by a gasification (of coal or biomass) process, but they can be adapted to convert a generic syngas obtained from electrolysis. Catalytic methanation usually takes place at temperatures above 250 °C. CO_2 methanation recently gained attention due to the interest in chemical storage of surplus electricity through the power-to-gas pathway: carbon dioxide can react with hydrogen coming from electrolysis and no further gas correction/cleaning is required before methanation. Thus, carbon dioxide is converted into methane according to the Sabatier reaction (1-2). Chemical equilibrium of CO_2 hydrogenation reaction is affected by pressure and temperature. Reaction (1-2) is exothermal, thus methane production is favoured at low temperatures. Moreover, there is a mole reduction

between reactants and products: higher pressure values shift the equilibrium conversion towards the products. High reaction temperature may represent a drawback from several standpoints: it limits the thermodynamically achievable conversion and could damage the catalyst via thermal degradation (e.g. nickel sintering). On the other hand, the catalyst could not be active below certain temperature values. The range typically considered for catalytic methanation is 250-600 °C, even though the extreme values are affected by the nature of the catalyst [28], [29].

The high reaction heat makes methanation a challenging process with a long history of research and development. The initial application of methanation was the carbon monoxide removal from syngas in ammonia synthesis [64], [65]. CO methanation gained renewed interest for SNG production from coal gasification during the oil crisis in 1970s ([66]). CO_2 methanation process development started from CO methanation and then followed a separated path due to the different inlet gaseous mixtures. Fixed-bed type represents the most mature (and commercially available) reactor technology. A fixed bed methanation reactor can be adiabatic or cooled. One of the key issues is represented by the temperature control within the catalytic bed: methanation reactions are strongly exothermal and the maximum temperature could be high enough to damage/deactivate the catalyst. If a stoichiometric mixture (H_2=80 vol.-%; CO_2=20 vol.-%) entering at 250 °C is considered, the adiabatic equilibrium temperature is above 800 °C, thus not acceptable for almost all the catalysts. Almost all industrial scale methanation plants involve a series of adiabatic fixed bed reactors: several strategies have been adopted in order to moderate the adiabatic outlet temperature. In several concepts, the outlet gas from the first (or the second) reactor is recycled to the beginning of the line and mixed with fresh reactant: this solution has been adopted by Haldor Topsøe ([67]), Lurgi ([68]) and Conoco Philips ([69]). The second possibility consists in staging (if possible) CO and/or CO_2 injection into the reacting mixture: H_2-excess methanation takes place in the first/second reactor (RMP, [70]). Another option involves steam injection before the first reactor: water addition shifts equilibrium towards the reactants but, on the other hand, acts as a thermal sink limiting the outlet temperature (ICI and Koppers, [66]). Steam can also be used in case of inlet mixture with low H_2/CO or H_2/CO_2 ratio to prevent carbon formation. Methane synthesis can be performed by a once-through method in quasi-isothermal reactors cooled by evaporating water or diathermic oil. Such systems are able to produce SNG with high methane content in one/two catalytic step [71]. In this work the attention was focused on this concept to lower as much as possible the number of reactors and to moderate the temperature peak within the first reactor, when reactants partial pressure (and thus the reaction rate) is greater.

Research efforts focused on the main concern related to fixed bed reactors: the temperature control. To overcome this drawback, structured reactors are under study due to the easier thermal management (the structure improves radial heat transfer) and lower pressure drop [72]. Milli-channel reactors have also been recently analyzed due to their high surface-to-volume ratio. Research activity

focused also on fluidized-bed methanation [73]. These concepts ensure excellent heat removal but the fluidization of catalyst results in high mechanical stress (leading to a shorter lifetime). Some industries and research institutes developed methanation concepts at pilot-scale [74], [75].

Three-phase methanation has been recently investigated at research stage. The attention focused on hydrodynamics, heat transfer and catalyst optimization [76], [77]. In this concept the liquid phase ensures high heat capacity, i.e. an excellent temperature control: the reactor can operate under isothermal condition even in case of load variation. However, cons as gas-liquid mass transfer resistance and evaporation/decomposition of the liquid phase should be considered.

Parts of this chapter were taken from papers where I am co-author [3], [8], [78].

Chapter 2

Process modelling of a Power to liquefied methane plant

In this chapter the process modelling of a Power to Gas methanation plant with the aim of liquefying the product gas obtaining liquefied methane gas (LMG). In the past years, liquid natural gas (LNG) has received a lot of interest as new applications are being studied and developed not only in the niche application of natural gas transportation. These applications can be:

- ➢ Heavy trucks and light-duty freight/passenger vehicles through the L-CNG filling stations concept providing both LNG to trucks and compressed natural gas (CNG) to light vehicles[79], [80].
- ➢ Marine transportation: by substituting diesel powered cargoes with LNG a reduction of 90% of SO_x, 35% NO_x, 29% CO_2, 85% carbon particulate is achievable[81], [82].
- ➢ Fertilizer industry[83].
- ➢ Electricity production[83].

The study was performed on a demo plant built in the framework of the EU funded project Store&GO. The plant has been built in the municipality of Troia (FG), Italy. In this region there is a high concentration of wind and solar production capacity. The demo has a maximum electricity input of 200kW to the electrolysis unit. The block flow diagram of a power to liquid methane plant is reported in Figure 2-1. The plant should have the capacity to both inject the gas in the natural gas grid or liquefy it to produce LNG.

32,8 kg$_{H2O}$/h

200 kW$_{el}$

Electrolyser -46,5 kW$_{th}$

29,2 kg$_{O2}$/h

3,6 kg$_{H2}$/h

20 kg$_{CO2}$/h

6 kW$_{el}$ CO$_2$ capture unit

40,1 kW$_{th}$

Methanation

-22,3 kW$_{th}$ (ζ_{CO2}=95%)

Gas Drying and Compression

Gas separation unit

7,2 kg$_{SNG}$/h

Liquefaction unit

7,2 kg$_{LNG}$/h
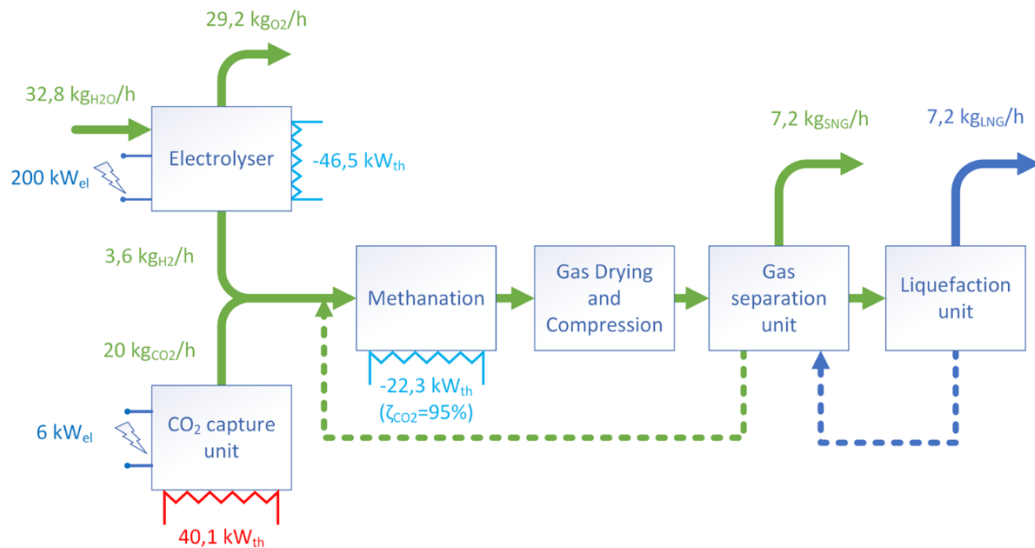
Figure 2-1. Block flow diagram with preliminary mass and energy balance

This chapter is entirely taken from the paper where I am first author [78].

2.1 Model setup

2.1.1 Electrolysis unit

Different technologies of electrolysers can be used to split water into hydrogen and oxygen: alkaline electrolysis cells (AEC), proton exchange membrane electrolysis cells (PEMEC) and solid oxide electrolysis cells (SOEC). The AECs and PEMECs are fed with liquid water and operate at low temperature (<200 °C) while in SOECs steam electrolysis occurs at high temperature (700-900 °C). The most mature and low capital cost electrolysis technology is the AEC [84], but is generally characterized by comparatively lower efficiencies than SOEC and PEMEC. This is also the technology of the electrolyser inherited from the INGRID project.

The AEC unit used in the demo has a power consumption of 4,9 kWh/Nm$^3_{H2}$ (AC power including all the utilities) and this translates to a module efficiency of 71,7% HHV basis (60,7% LHV basis). These units generally work between 50 and 80 °C and can deliver high purity hydrogen up to 15 barg without additional compression. The demo plant's electrolyser module can be fed with up to 200 kW of electricity. This allowed for the evaluation of the hydrogen flowrate and heat production.

2.1.2 Methanation unit

One of the Store&GO project aim is to demonstrate three different CO$_2$ methanation processes: modular milli-structured catalytic methanation reactors, catalytic honeycomb/structured wall methanation reactors and biological methanation. The investigated demo can operate up to 10 bar with the methanation reactor for mainly two reasons: hydrogen is produced up to 15 bar and an additional

compressor will not be available; the milli-structure methanation reactor is built to withstand pressures up to 10 bar. Different reactor configurations that operate at 10 bar were considered:

➢ Series of five adiabatic reactors with intercooling: the equilibrium conversion 96 % is reached at the outlet of the last reactor. The conversion was calculated using equation (2-1). In Figure 2-2 the layout of the five adiabatic reactors is reported along with further details of conversions, temperatures and conversion.
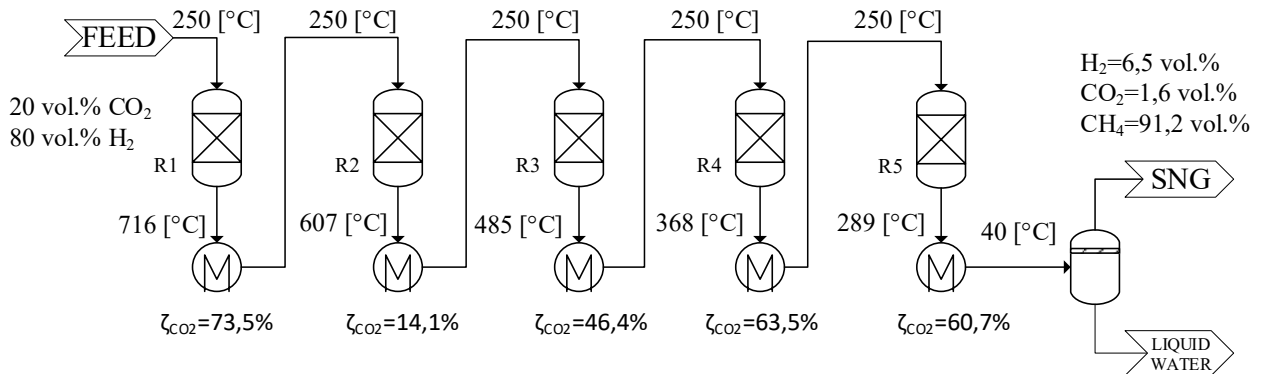
Figure 2-2. Series of five adiabatic reactors with intercooling operating at 10 bar

➢ Adiabatic and isothermal (operating at 280 °C) in series with intercooling and water condensation at 40°C: this configuration reaches a conversion of 99,1%. The layout is represented in Figure 2-3. The temperature at the outlet of the first reactor is higher than 700 °C which is not compatible with most methanation catalysts. This is also a problem for the first configuration.
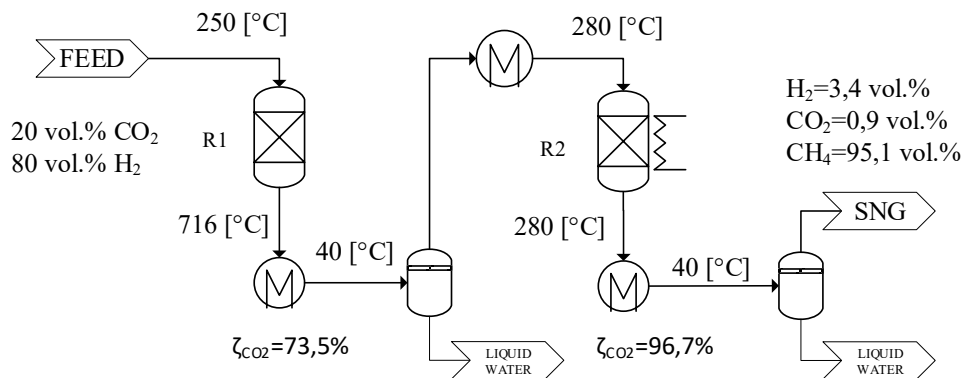
Figure 2-3. Series of an adiabatic and an isothermal reactor with intercooling and water condensation operating at 10 bar

➢ Two isothermal reactors operating at 280 °C in series with intercooling and water condensation at 40 °C reaching 99,8% of conversion (Figure 2-4).

27
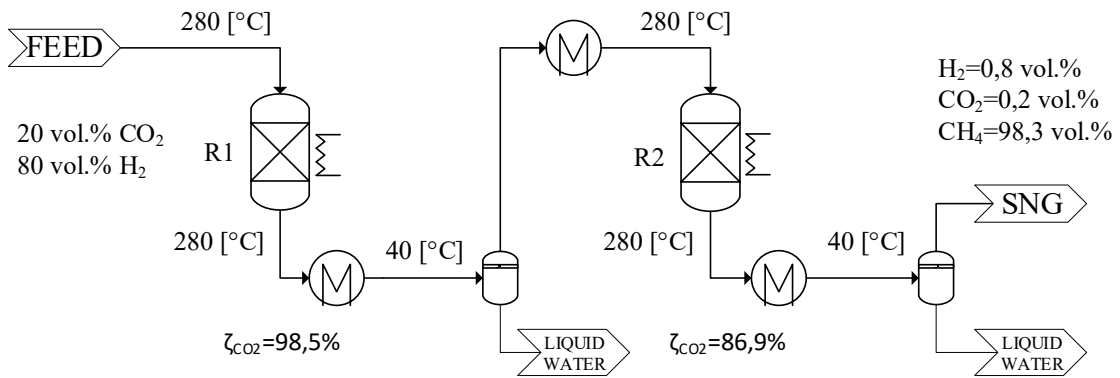
Figure 2-4. Series of two isothermal reactors with intercooling and water condensation operating at 10 bar

$$\zeta_{CO_2} = 1 - \frac{\dot{n}_{CO_2,out}}{\dot{n}_{CO_2,in}} \qquad (2\text{-}1)$$

Even with the highest conversion achievable in the last case the product gas doesn't meet the liquefaction specifications: a gas separation system is therefore needed. A single isothermal methanation reactor configuration for the methanation module was chosen since with this configuration a high conversion is possible and a purification step will be needed anyways. The reactor operates isothermally at 280 °C and at a total pressure between 4 and 10 bar. The pressure at which the reactor operates can vary to compensate the slow catalyst activity decay that may occur during the lifespan of the plant. This will also be object of investigation in the next chapters as well as during the operation of the demo plant. From tests performed on a milli-structured reactor prototype a set of operating conditions have been identified (not reported here) that guarantee a CO_2 conversion of ≥95% at 4 bar. The reactor was simulated as a yield reactor using this last value of conversion.

2.1.3 Gas separation unit

None of the above solutions can give the required gas purity for natural gas grid injection or liquefaction specifics. Therefore, a gas purification unit is required to lower the hydrogen and/or carbon dioxide in the product stream.

For this plant concept, a membrane gas separation was used for the gas separation module to meet the NG grid specifications. Hydrogen is a small, non-condensable gas, which is highly permeable compared to all other gasses. This is particularly true with the glassy polymers primarily used to make hydrogen-selective membranes. Fluxes and selectivity of hydrogen through some of these materials are shown in Table 2-1.

Table 2-1:Hydrogen separation proprieties of a few membranes [85]

Membrane (developer)	Selectivity			Hydrogen pressure normalizedFlux $\left(\dfrac{10^{-6}\ cm^3_{STP}}{cm^2\ s\ cmHg}\right)$
	H_2/CO	H_2/CH_4	H_2/N_2	
Polyaramide (Medal)	100	>200	>200	
Polysulfone (Permea)	40	80	80	100
Cellulose acetate (Separex)	30-40	60-80	60-80	200
Polyimide (Ube)	50	100-200	100-200	80-200

A preliminary design of the gas separation module has been identified by using a shortcut design model developed by Pettersen et al [86] for a hollow fibre module (Figure 2-5) in counter-current operation. A brief explanation of how they've developed their model is summarized here.
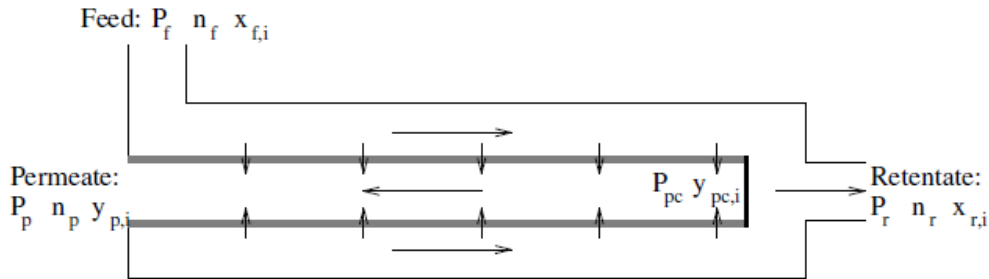
Figure 2-5: Simplified picture of hollow fibre module (from Patterson et al)

According to the solution-diffusion theory for gas separation membranes, the local permeation of gas through a non-porous membrane can be described by Fick's law (2-2).

$$d\dot{n}_\iota = \frac{\mathcal{P}_i\ dA\ (p_{f,i} - p_{p,i})}{d} \qquad (2\text{-}2)$$

Where

$\dot{n}_\iota \rightarrow$ volumetric flow of component i $\left(m^3_{STP}/h\right)$

$A \rightarrow$ membrane area (m^2)

$\mathcal{P}_i \rightarrow$ membrane permeability of component i $\left(m^3_{STP}\ m/m^2\ h\ bar\right)$

$p_{x,i} \rightarrow$ partial pressure of component i in the feed or permeate (bar)
$d \rightarrow$ membrane active phase thickness (m)
The total flow across the membrane is given by equation (2-3)

$$\int d\dot{n}_i = \dot{n}_p\ y_{p,i} \qquad (2\text{-}3)$$

Membrane permeation is a rate-governed process this means that equilibrium is never reached. Rate-governed processes are generally described by relations between a driving force or potential and a flux. Another rate-governed process is

29

the heat transfer in a heat exchanger in which the integral heat transferred is given by equation (2-4).

$$Q = U \, A \, \Delta T_{lm} \tag{2-4}$$

Therefore, the heat exchanger duty is a function of the global heat transfer coefficient U, the area A and the logarithmic mean temperature difference. From Fick's law (2-2) it can be observed that for membrane mass transfer the driving force is given by the difference of partial pressure of the component across the membrane. By resemblance with the heat transfer equation, Pettersen et al [86] proposed to use a similar equation for membrane operations, assuming counter-current flow in the module, and it can be written as follows:

$$\int d\dot{n}_i = Q_i \, A \, \Delta p_{lm,i} \tag{2-5}$$

Where

$Q_i = \mathcal{P}_i/d \rightarrow$ overall permeability constant $m_{STP}^3/(m^2 \, m \, h \, bar)$

$$\Delta P_{lm,i} = \frac{(p_{f,i} - p_{p,i}) - (p_{r,i} - p_{pc,i})}{\ln \dfrac{p_{f,i} - p_{p,i}}{p_{r,i} - p_{pc,i}}} \tag{2-6}$$

The material balance over the membrane module is given by equation (2-7).

$$x_{f,i} = \theta y_{p,i} + (1 - \theta)x_{r,i} \tag{2-7}$$

Where

$\theta = \dfrac{\dot{n}_p}{\dot{n}_f} \rightarrow$ membrane cut ratio

$x_{f,i}, x_{r,i} \rightarrow$

In conclusion, by combining equation (2-5) and (2-7), it was obtained:

$$\dot{n}_f \theta y_{p,i} = Q_i \, A \, \Delta P_{lm,i} \tag{2-8}$$

By using Patterson's approximation of the logarithmic mean and approximating $y_{pc,i} \cong y_{p,i}$:

$$y_{p,i} = \frac{-BB_i + \sqrt{(BB_i)^2 - 4AA_i \, CC_i}}{2AA_i} \tag{2-9}$$

Where:

$$AA_i = \frac{\delta}{3}\left(\frac{2\theta}{R} - \delta\right) + \frac{\theta}{3(1-\theta)}\left(\frac{\theta}{R} + \frac{\theta}{12(1-\theta)} - \delta\right) + \left(\frac{\theta}{R}\right)^2 \tag{2-10}$$

$$BB_i = \frac{x_{f,i}}{3}\left(1 + \frac{1}{1-\theta}\right)\left(\delta - \frac{\theta}{R}\right) + \frac{\theta \, x_{f,i}}{18(1-\theta)}\left(7 - \frac{1}{1-\theta}\right) \tag{2-11}$$

$$CC_i = \left(\frac{x_{f,i}}{6(1-\theta)}\right)^2 (\theta^2 + 12\theta - 12) \tag{2-12}$$

$\delta = P_p/P_f \rightarrow$ transmembrane pressure ratio
$R = A \, P_f Q_i/\dot{n}_f \rightarrow$ dimensionless permeation factor
$d \rightarrow$ membrane active layer thickness (m)
$x_{f,i} \rightarrow$ molar fraction of component i in the feed stream.

Since the sum of the mole fractions must be equal to one $\sum_1^{nc} y_{p,i} = 1$ an implicit function of θ is obtained (2-13).

$$f(\theta) = \sum_{1}^{nc} y_{p,i}(\theta) - 1 = 0 \qquad (2\text{-}13)$$

A numeric resolution must be implemented for this equation to find the membrane cut ratio. The membrane block along with the numeric resolution were implemented in the Aspen process simulator. Sensitivity analysis of the flow sheet was carried out by varying the membrane areas and monitoring the hydrogen content at the outlet.

2.1.4 Liquefaction unit

Mainly three different technologies are available for natural gas liquefaction: cascade, expansion and mixed refrigerant liquefaction processes [87]. The single mixed refrigerant (SMR) liquefaction process seems to be the best choice for small scale liquefaction due its high efficiency and low complexity (i.e., low number of equipment) compared to the other technologies [88]. Hence, this process was selected for the simulation of the liquefaction unit.

The considered SMR system is represented in Figure 2-6. It has a two-stage refrigerant compression section with inter-stage cooling provided by an air-cooler (E-101), a phase separator between the compression stages in case refrigerant condensation occurs (V-100), a pump (P-100) to move the condensate and a second air-cooler (E-102) that partially condensates the vapour stream exiting the second stage of compression. The resulting compressed refrigerant is then sent to the main heat exchanger where it undergoes full condensation followed by an isenthalpic lamination achieved with the lamination valve TV-100. The stream then is used as the main coolant of the process. Meanwhile, the SNG is fed to the unit where it is cooled and condensed at -160 °C. The obtained liquid gas is laminated to the storage pressure of 2 bar enabling the evaluation of the boil-off gas (BOG) stream. Heat recovery is performed before recycling the BOG stream to the process.
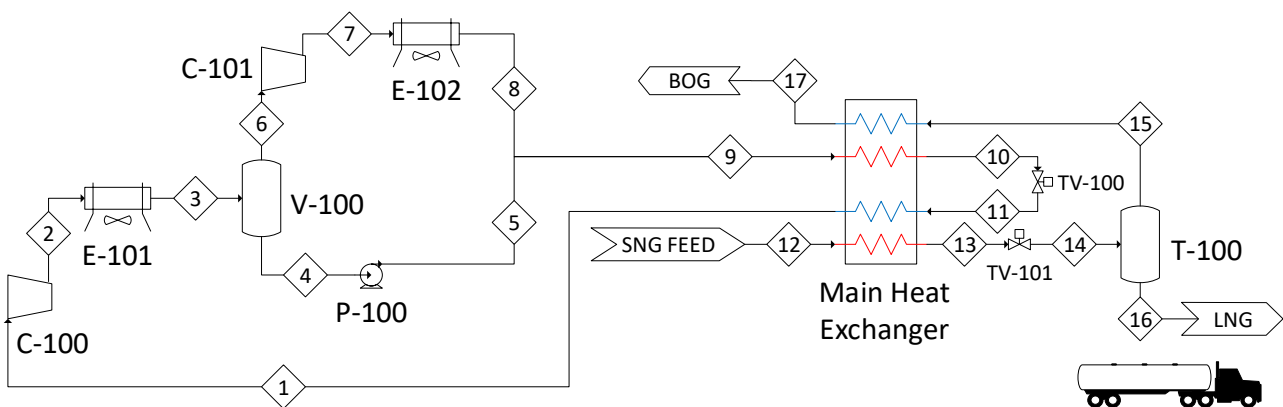
Figure 2-6. Flow diagram of the SMR process

A SMR process uses a mixture of nitrogen and hydrocarbons (C1 to C5) as refrigerant. The composition of the refrigerant has been tuned to follow the same trend of the hot composite curve thus minimizing the required compression work on the refrigerant. The chosen target function to minimize is the total work required for compression (represented by the sum of the duty of C-100, P-100 and C-101)

that depends on the following parameters: refrigerant composition, condensation and evaporation pressure. The optimization of the SMR process involves a nonlinear and strongly coupled system of equations: a robust optimization method is thus required. Different procedures to solve the optimization problem are present in literature as the Box method, the Graphical Targeting Approach, the genetic algorithm (GA) and Derivative-free [89]. In this case the GA was used and implemented according to Cao et al. [90].

For the simulation of this section the following assumptions were made:

➢ No pressure drops in the heat exchangers and phase separators
➢ Refrigerant temperature at main Heat exchanger inlet of 40 °C
➢ The minimum temperature approach between cold and hot streams equal to 3 °C [90], [91]
➢ Null cold box heat leakage
➢ Compressor adiabatic efficiency of 75%
➢ The refrigerant is a mixture of nitrogen, methane, ethane or ethylene, propane or propene and isopentane. The refrigerant mixture composition must be optimized in order to minimize the total work required to perform the liquefaction.

2.2 Results

2.2.1 Model results

The target for the demo plant in terms of electricity to the electrolyser was set equal to 200 kW, resulting in a total hydrogen production of 3.6 kg_{H_2}/h (41.3 $Nm^3_{H_2}$/h). The CO_2 inlet flow was calculated by keeping the stoichiometric ratio (H_2/CO_2=4), including also the non-stoichiometric recycle stream. A CO_2 flow rate of 20 kg_{CO_2}/h (10.3 $Nm^3_{CO_2}$/h) resulted from the simulation. The carbon dioxide capturing unit energy requires 6.0 kW of electricity and 40.1 kW of heat to produce the 20 kg/h CO_2 flow rate. Furthermore, the unit produces CO_2 at near atmospheric pressure requiring compression to the process pressure of 4 bar meaning that an additional compressor is need whose power requirements was estimated in 0.8 kW of electricity (isentropic efficiency 75%). After mixing the H_2, CO_2 and recycle the resulting stream is heated to 280 °C; the calculated duty of the heat exchanger is 5.3 kW. Since the reactor works in isothermal mode, the 21.9 kW of heat produced by the methanation reaction is removed. About 60% of the methanation outlet stream is made of water vapor, the majority of which (97.8%) is separated in an air-cooled condenser that cools the stream to 40°C resulting in a duty of the condenser of 14.8 kW. In order to reach the required specification of <1 ppm_w of H_2O for the liquefaction the stream was further desiccated by using a TSA module.

The dried stream is then compressed to 13 bar,a and sent to the membrane gas separation system. The compressor duty at full capacity is 2.8 kW. Different types of membranes are available for CO_2 separation from natural gas like streams: polymeric, zeolite, carbon molecular sieves, etc. The most used membrane type in

CO_2 gas separation is the glassy polymer category thanks to their selectivity, excellent thin film forming, good mechanical properties and higher permeability to low molecular weight species [92]. In Table 2-2 the most interesting membranes that were used to perform the simulations are reported.

Table 2-2. Tested membranes single gas permeability and ideal selectivity

	Permeability (barrer[a])			Ideal selectivity	
	H_2	CO_2	CH_4	H_2/CH_4	CO_2/CH_4
M1. Cellulose acetate [93]	2.6	9	0.43	6.2	21.1
M2. TBDA1-6FDA-PI [94]	253	155	3.3	76.7	46.9
M3. 6FDA-durene [95]	600	455.8	28.4	21.1	16.1
M4. TR-PBI (450) [96]	1779	1624	35	50.8	46.4

[a] 1 barrer=1×10^{-10} cm$^3_{STD}$ cm s^{-1} cm^{-2} cm$^{-1}_{Hg}$

None of these membranes can reach the required gas purification in one stage of separation. In fact, the cut ratio of the module would be higher than 0.5 creating high recirculation flow rates with a high content of methane. For this application, the M3. 6FDA-durene polyimide asymmetric membrane with an active phase layer thickness of 2 µm was considered.

In Figure 2-7 it can be seen the performance of the separation unit in terms of retentate hydrogen concentration and cut ratio of a one-stage membrane separation module. One stage membrane separation cannot achieve the required hydrogen concentration for natural gas pipeline injection.
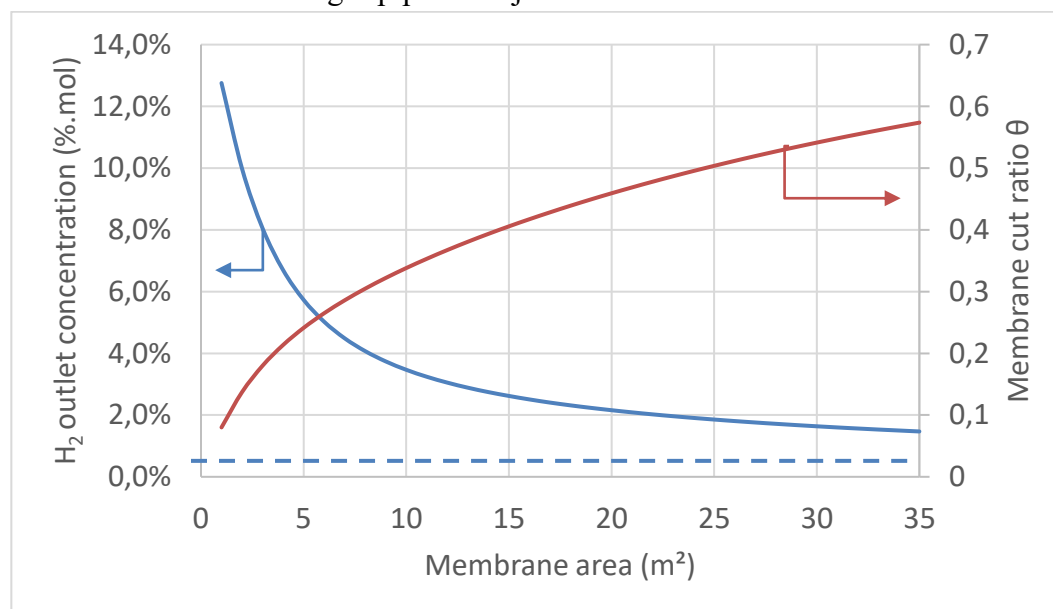
Figure 2-7: One stage membrane separation unit cut ratio and performance versus membrane area. The dashed line represents the H2 concentration target.

To reach the required $0.5\%.vol$ of hydrogen needed for the natural gas pipeline, a two-stage membrane separation system is proposed as shown in Figure 2-8. In this configuration, another membrane unit is added to which the retentate

stream from the first membrane is fed while the permeate stream from this second module is recompressed, cooled and recycled to the first membrane inlet.
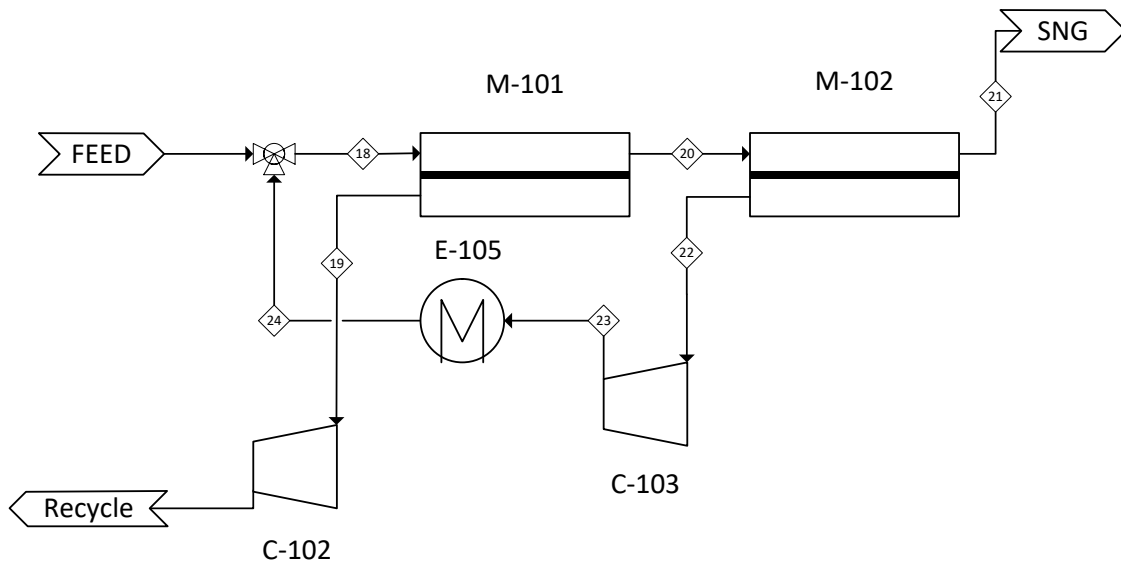
Figure 2-8: Two stage membrane gas separation layout

In Figure 2-8 the module performance is calculated as a function of the areas of the two membranes. With this layout, we can reach the hydrogen concentration target necessary for the natural gas pipeline injection with two modules of $11\ m^2$ of area each.
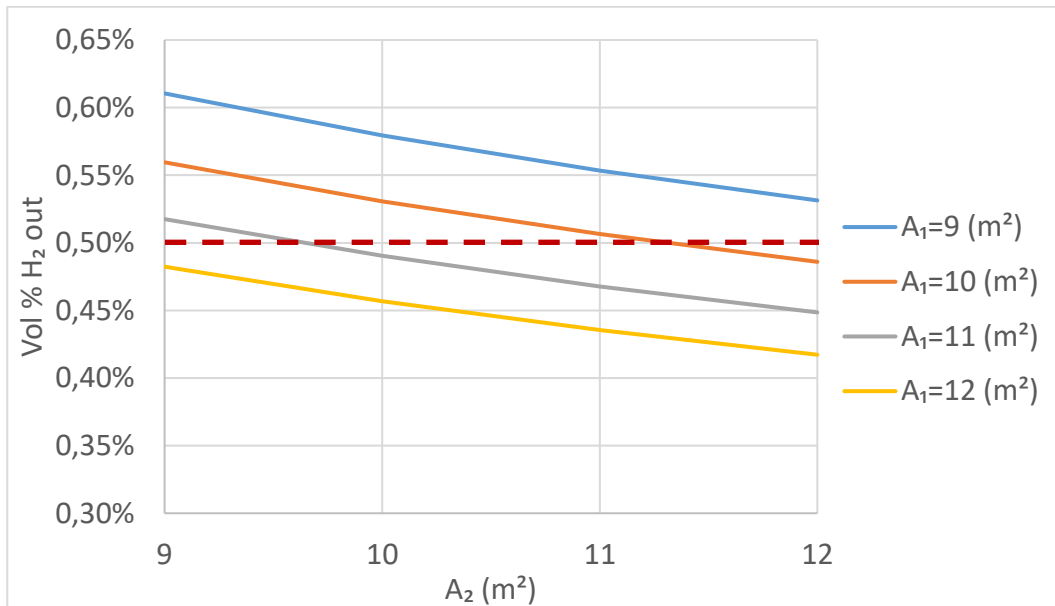
Figure 2-9: Separation unit performance vs membrane areas in a two-stage separation layout (A1 area of the first module; A2 area of the second module)

Therefore, a two-stage system was developed where the permeate from the first module is recirculated to the methanation reactor inlet and the retentate stream is sent to the second module. From the second module, the permeate stream is compressed and sent back to the first stage inlet (Figure 2-8). With this

arrangement, the specification <0.6% of CO_2 is met with two modules of 20 m^2 of active surface area each made of membrane M2 (commercially available modules with equal performance). The cut ratio of membrane separation unit is 0.197 giving a recirculation stream to the methanation unit of 1.8 kg/h. Also H_2 is separated reducing the overall boil-off from the liquefaction stage and mass flow to the unit.

The retentate from the second membrane stage is sent to a TSA polishing unit that lowers the CO_2 content to less than 50 ppm_v. The resulting stream is ready to undergo the liquefaction process.

The optimization of the mixed refrigerant composition and pressures was carried out for the four refrigerant compositions. In Table 2-3 the optimization results are reported. The mole fractions for the low temperature components (N_2 and CH_4) and high temperature components (isopentane) does not change in a sensible manner between refrigerants. The main component in all the mixtures is methane around 41%. The optimum lamination and compression outlet pressures do not change significantly between the different case studies. The lowest specific energy consumption was found for the ethylene-propane containing refrigerants (0.57 kWh/kg_{LNG}). However, it is noteworthy that all the refrigerant compositions are suitable for the liquefaction of SNG with low differences in energy consumption under the assumed conditions (maximum 0.6 kWh/kg_{LNG}). Literature results of SMR systems used to liquefy natural show specific power consumptions lower than the ones found in this application (0.29-0.42 kWh/kg_{LNG} [87], [90], [91]). This difference could be attributed to the difference in composition of the gas that is being liquefied. In this case the gas that we liquefy basically pure methane. On the contrary, natural gas is not made of pure methane: 87-97% methane, 1.5-9% ethane, 0.2-5% nitrogen, 0.1-1.5% propane[97].

Table 2-3. Refrigerant composition, pressures and performance

	Refrigerant composition (%.mol)							P_{11}	P_9	Refrigerant flow	Required work
	N_2	CH_4	C_2H_6	C_2H_4	C_3H_8	C_3H_6	Iso-pentane	bar	bar	$\frac{kg_{REF}}{kg_{LNG}}$	$\frac{kWh}{kg_{LNG}}$
1	13.0	41.3	18.5	-	-	13.1	14.0	3.2	33.4	7.9	0.59
2	12.6	41.6	19.1	-	13.1	-	13.7	3.2	32.1	8.0	0.59
3	12.0	42.1	-	17.9	13.7	-	14.3	3.4	32.6	7.9	0.57
4	13.9	39.6	-	14.5	-	18.8	13.2	3.3	33.3	8.1	0.60

Figure 2-10 the composite curves and the temperature difference between the hot and cold side are reported. The plots are relative to the optimized mixtures shown in Table 2-3. In all four mixtures the temperature difference curves have two main peaks. The right peak at high temperature is caused by a phase change in the cold stream, which is converted from liquid to vapor that has a lower heat capacity than the liquid. The left peak at low temperature is caused by a phase change in the hot stream, which is converted from vapor to liquid that has a higher heat capacity. Two pinch points are present in all four cases: one at low temperature (145 K, when the liquefaction of the methane stream starts) and one at high temperature (313 K).

The refrigerant that better glides the cold composite to the hot composite curve is the ethylene-propane giving a lower mean temperature difference causing the slightly lower energy requirement. However, a lower average temperature difference also means that a greater heat exchange area might be required, translating in an increased cost.
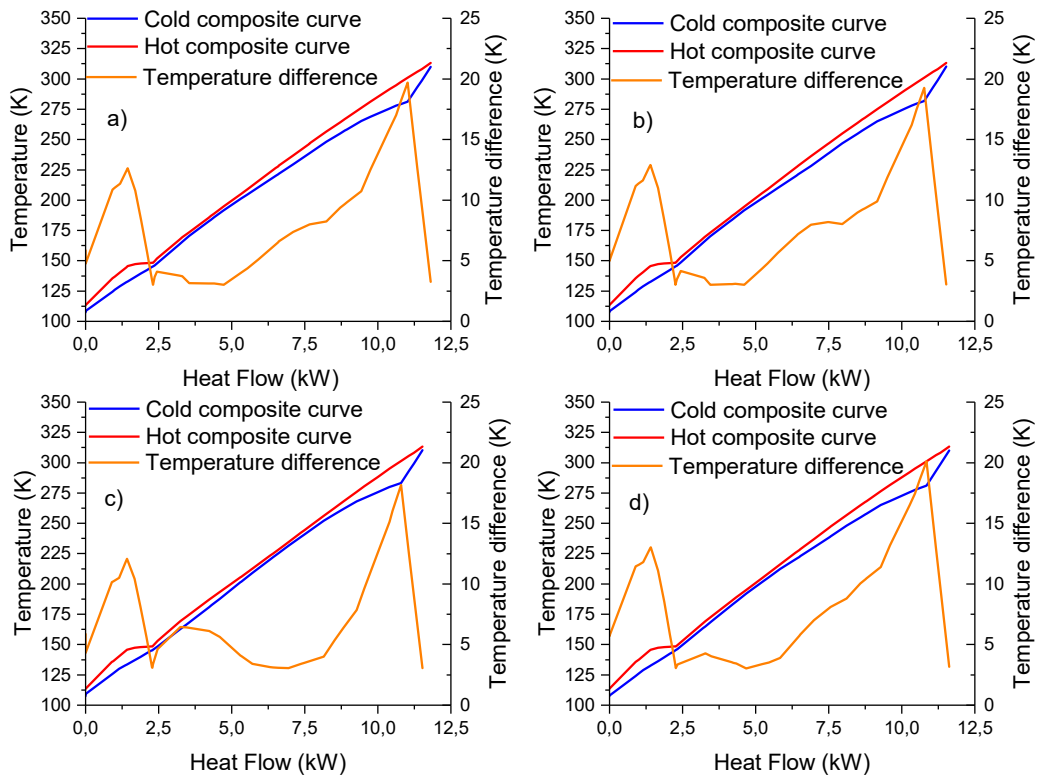
Figure 2-10. Composite temperature curves and temperature difference for the optimized refrigerant composition a) Ethane-Propane, b) Ethane-Propene, c) Ethylene-Propane and d) Ethylene-Propene

Two different scenarios arise in the management of the recycle streams: a) recirculation of the membrane first stage permeate and the boil-off stream directly to the methanation reactor; b) recirculation of the boil-off with the second stage membrane permeate to the membrane inlet compressor.

With the second arrangement, the recirculation of a methane rich and high flow rate stream to the methanation reactor inlet is avoided, lowering the possibility of carbon deposition, while the composition of the membrane feed is marginally altered.

In Figure 2-11 the complete process flowsheet diagram and in Table 2-4 the associated stream table are reported.
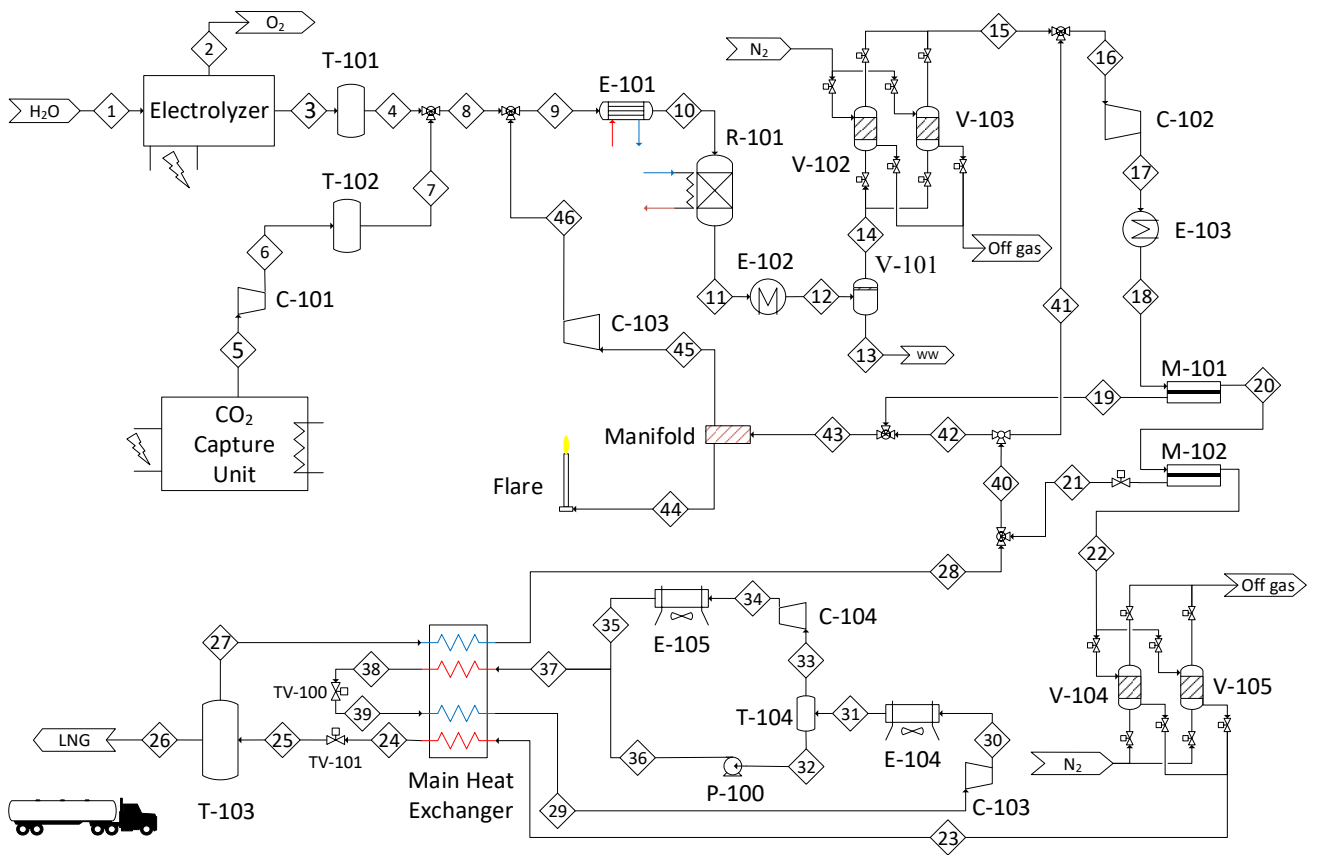
Figure 2-11: Process flow diagram

Table 2-4. Stream table of the process recycle scheme A (omitted null or least important streams)

	Mole fraction (%.mol)				Total Flow		Temperature	Pressure	Vapor
	CO₂	CH₄	H₂	H₂O	(kmol/h)	(kg/h)	(°C)	(bar)	Fraction
1	0.0%	0.0%	0.0%	100.0%	1.81	32.6	75.0	15.0	0.00
4	0.0%	0.0%	100.0%	0.0%	1.81	3.6	20.0	5.0	1.00
5	100.0%	0.0%	0.0%	0.0%	0.45	20.0	20.0	1.0	1.00
7	100.0%	0.0%	0.0%	0.0%	0.45	20.0	20.0	5.0	1.00
9	19.6%	1.8%	78.6%	0.0%	2.42	25.5	20.6	5.0	1.00
10	19.6%	1.8%	78.6%	0.0%	2.42	25.5	260.0	4.0	1.00
11	1.6%	32.6%	6.3%	59.5%	1.52	25.5	280.0	2.0	1.00
12	1.6%	32.6%	6.3%	59.5%	1.52	25.5	40.0	2.0	0.42
14	3.7%	78.1%	15.0%	3.2%	0.63	9.5	40.0	2.0	1.00
15	3.9%	80.6%	15.5%	0.0%	0.61	9.2	40.0	2.0	1.00
16	4.0%	78.4%	17.6%	0.0%	0.70	10.3	38.7	1.2	1.00
18	4.0%	78.4%	17.6%	0.0%	0.70	10.3	35.0	13.2	1.00
19	13.2%	27.4%	59.4%	0.0%	0.16	1.8	35.0	1.2	1.00
20	1.3%	93.3%	5.4%	0.0%	0.55	8.5	35.0	13.1	1.00
21	6.3%	67.4%	26.3%	0.0%	0.07	1.0	35.0	1.2	1.00
22	0.6%	97.0%	2.4%	0.0%	0.48	7.6	35.0	13.0	1.00
23	0.0%	97.6%	2.4%	0.0%	0.47	7.4	35.0	13.0	1.00
24	0.0%	97.6%	2.4%	0.0%	0.47	7.4	-160.0	13.0	0.01

25	0.0%	97.6%	2.4%	0.0%	0.47	7.4	-162.5	2.0	0.04
26	0.0%	99.9%	0.1%	0.0%	0.45	7.2	-162.5	2.0	0.00
27	0.0%	48.4%	51.6%	0.0%	0.02	0.2	-162.5	2.0	1.00
28	0.0%	48.4%	51.6%	0.0%	0.02	0.2	20.0	2.0	1.00
41	4.8%	62.9%	32.3%	0.0%	0.09	1.2	31.6	1.2	1.00
46	13.2%	27.4%	59.4%	0.0%	0.16	1.8	40.0	5.0	1.00

2.2.2 Heat integration and process efficiency

The electrolyser heat is not useful to the process since it is generated at a low temperature of (75-80 °C) hence no heat recovery is feasible for the plant needs. Since the methanation reaction is highly exothermic part of the produced heat is supplied to the feed stream, to meet the required temperature at the reactor inlet of 260 °C, while the remaining part is sent to the CO_2 capturing unit. In Figure 2-12 the Sankey diagram for the energy and mass balance is reported for stationary operation. By using this system integration layout ~41% of the heat required by the CO_2 capturing unit is coming from excess heat produced by the methanation reactor.

The overall plant efficiency was evaluated using the approach found in [98]. The overall plant efficiency and overall energy utilization factor were calculated with equations (2-14) and (2-15).

$$\eta_{0.0.a} = \frac{\dot{E}_{ch,2.2,out}}{\dot{E}_{th,1.4,in} + \dot{Q}_{1.2,in,a} + \dot{Q}_{2.0,in,a} + P_{1.1,a} + P_{2.1,a}} \cdot 100 \qquad (2\text{-}14)$$

$$\Theta = \left(1 - \frac{\dot{Q}_{1.0,out} + \dot{Q}_{2.0,out}}{\dot{E}_{th,1.4,in} + \dot{Q}_{1.2,in,a} + \dot{Q}_{2.0,in,a} + P_{1.1,a} + P_{2.1,a}}\right) \cdot 100 \qquad (2\text{-}15)$$

Where $\dot{E}_{ch,2.2,out}$ is the energy associated to the LNG product stream calculated as LNG flowrate multiplied by its higher heating value, $\dot{E}_{th,1.4,in} = 0$ is the convective flow of thermal energy associated with the feed of water to the electrolyser, $\dot{Q}_{1.2,in,a} = \dot{Q}_{2.0,in,a} = 0$ is the heat demand by the electrolyser and methanation units, $P_{1.1,a}$ and $P_{2.1,a}$ are the electricity demand by the electrolyser and the rest of the units, $\dot{Q}_{1.0,out}$ and $\dot{Q}_{2.0,out}$ are usable heat rejected by the electrolyser and methanation units.

The resulting overall plant efficiency of the demo is η=46,3% and an overall energy utilization factor Θ=75,2%, The main loss is due to the electrolyser module accounting for ~24% of efficiency reduction.

Water produced from the methanation unit and CO_2 capturing unit could be used with little to no purification as part of the feed to the electrolyser accounting for the total amount of water needed.
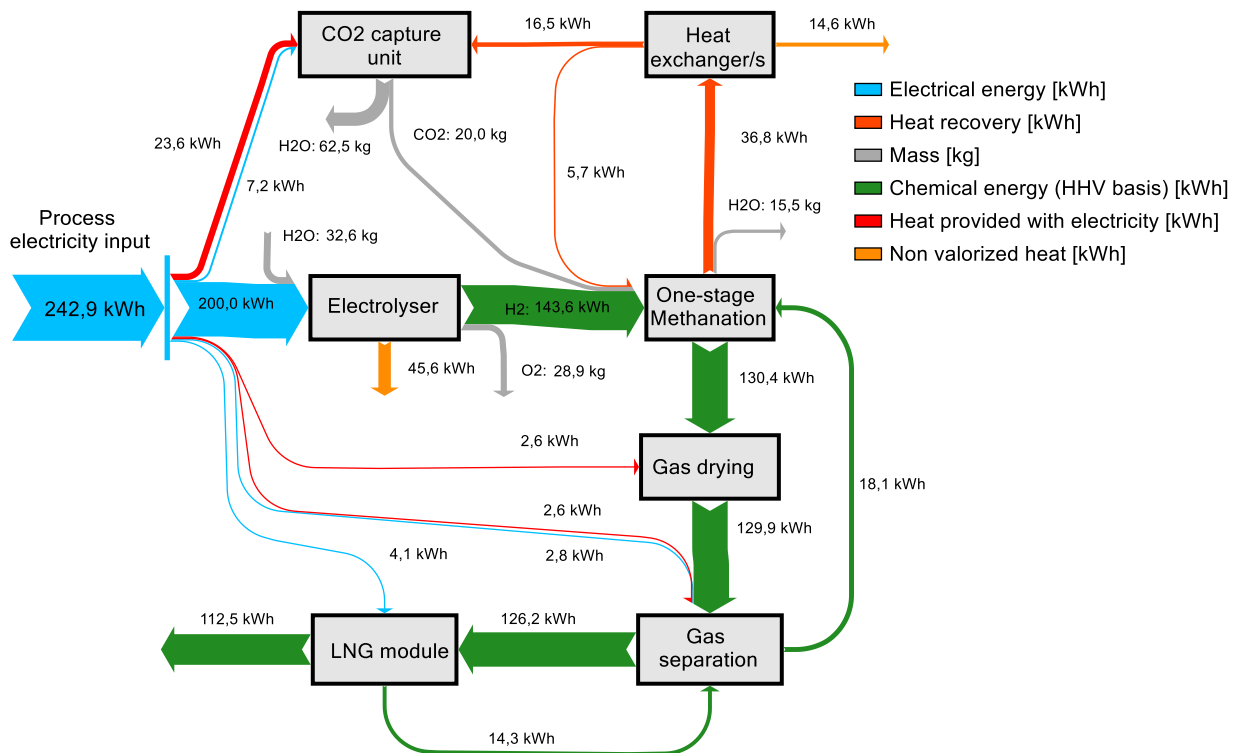
Figure 2-12. Energy and mass balance Sankey diagram

2.2.3 Beyond the Store&GO project

One limiting factor in the application of PtG technologies is the electrolysis. As previously mentioned, the most mature and cost effective (in terms of investment and maintenance cost per kW installed) is the AEC. Generally commercially available AEC units operate at temperature below 100 °C but also higher temperature are being studied [99]–[101]. A higher working temperature of the electrolyser module would have an increase in efficiency (i.e. electrolyte ohmic resistance reduction and reaction kinetics improve with temperature increase [26], [102]) and may allow to recover and use the produced heat. With the resulting heat recovery, the requirements of the CO_2 capture and for the two TSA units would be satisfied, potentially increasing process efficiency to 52.6% (considering the same electric to H_2 conversion efficiency) and the overall energy utilization to 85.3%. In Figure 2-13 the revised Sankey diagram with the new improved concept is reported.
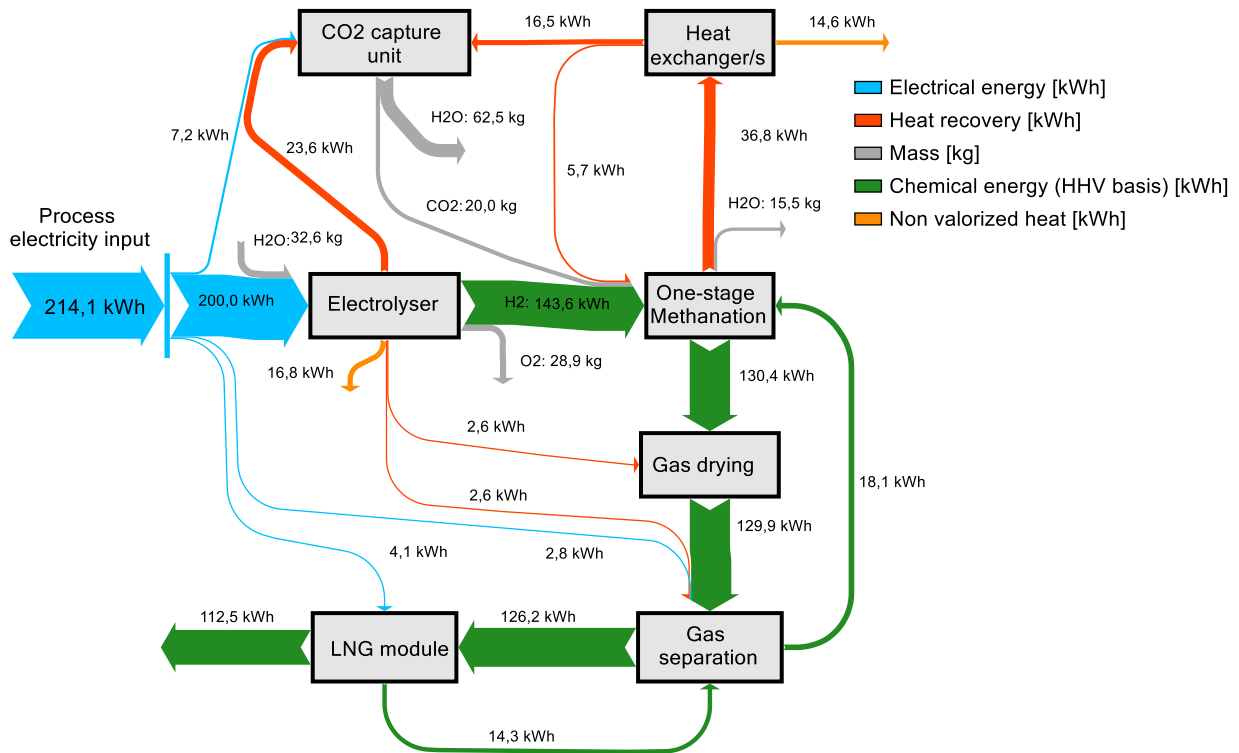
Figure 2-13. Energy and mass balance Sankey diagram for an improved concept

2.3 Carbon deposition map

It was also considered the possibility of carbon deposition and the reactions that may occur are reported below.

$$\Delta G_{298\,[K]}\left[\frac{kJ}{mol}\right] \qquad \Delta H_{298\,[K]}\left[\frac{kJ}{mol}\right]$$

$$2CO \rightleftharpoons C + CO_2 \qquad\qquad -119{,}7 \qquad\qquad -172{,}4 \qquad (2\text{-}16)$$

$$2H_2 + C \rightleftharpoons CH_4 \qquad\qquad -50{,}7 \qquad\qquad -74{,}8 \qquad (2\text{-}17)$$

$$CO + H_2 \rightleftharpoons C + H_2O \qquad\quad -91{,}1 \qquad\qquad -131{,}3 \qquad (2\text{-}18)$$

$$CO_2 + 2H_2 \rightleftharpoons C + 2H_2O \qquad -62{,}5 \qquad\qquad -90{,}1 \qquad (2\text{-}19)$$
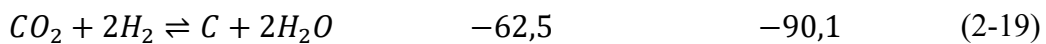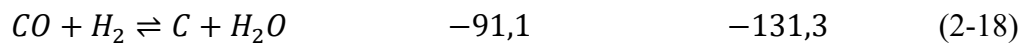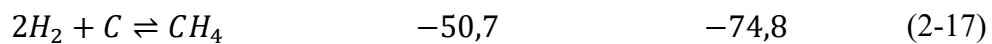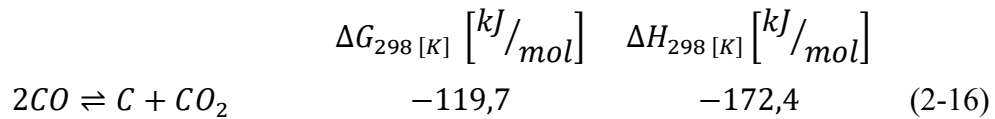
One of the main deactivation mechanisms in CO or CO_2 methanation processes is the formation of solid carbon on the catalyst. A thermodynamic analysis over a large range of compositions was performed to predict whether solid carbon formation is feasible and carbon deposition boundaries were identified in representative temperature $(250 \div 650\ °C)$ and pressure $(4 \div 10\ bar)$ ranges that may be encountered in methanation process.

The species that are involved in the reaction system are generally CO_2, H_2, CH_4, H_2O, CO and solid carbon. In the range of operating conditions that were considered here, higher molecular mass hydrocarbons formed are in parts per million range and were neglected in the study. The effect of neglecting these components were quantified by Tevebaugh et al [103] in their study and it has been seen that in the worst case the difference is of 1%.

The analysis was carried out by calculating the chemical equilibrium of the system using the Gibbs free energy minimization method. The thermodynamic

40

proprieties of pure components have been calculated by using data from NIST chemistry webbook and a Matlab® program for equilibrium calculations has been written for this purpose.

According to Frick et al [104] in the range of operating conditions considered the most likely species of carbon is graphitic carbon instead of amorphous carbon. Therefore, only graphitic carbon was considered in the following calculations. The results of the calculations are represented by means of ternary diagrams of C-H-O for an easy and immediate interpretation as suggested by Frick et al [104] and Tevebaugh et al [103] and they are summarized as follows in Figure 2-14.
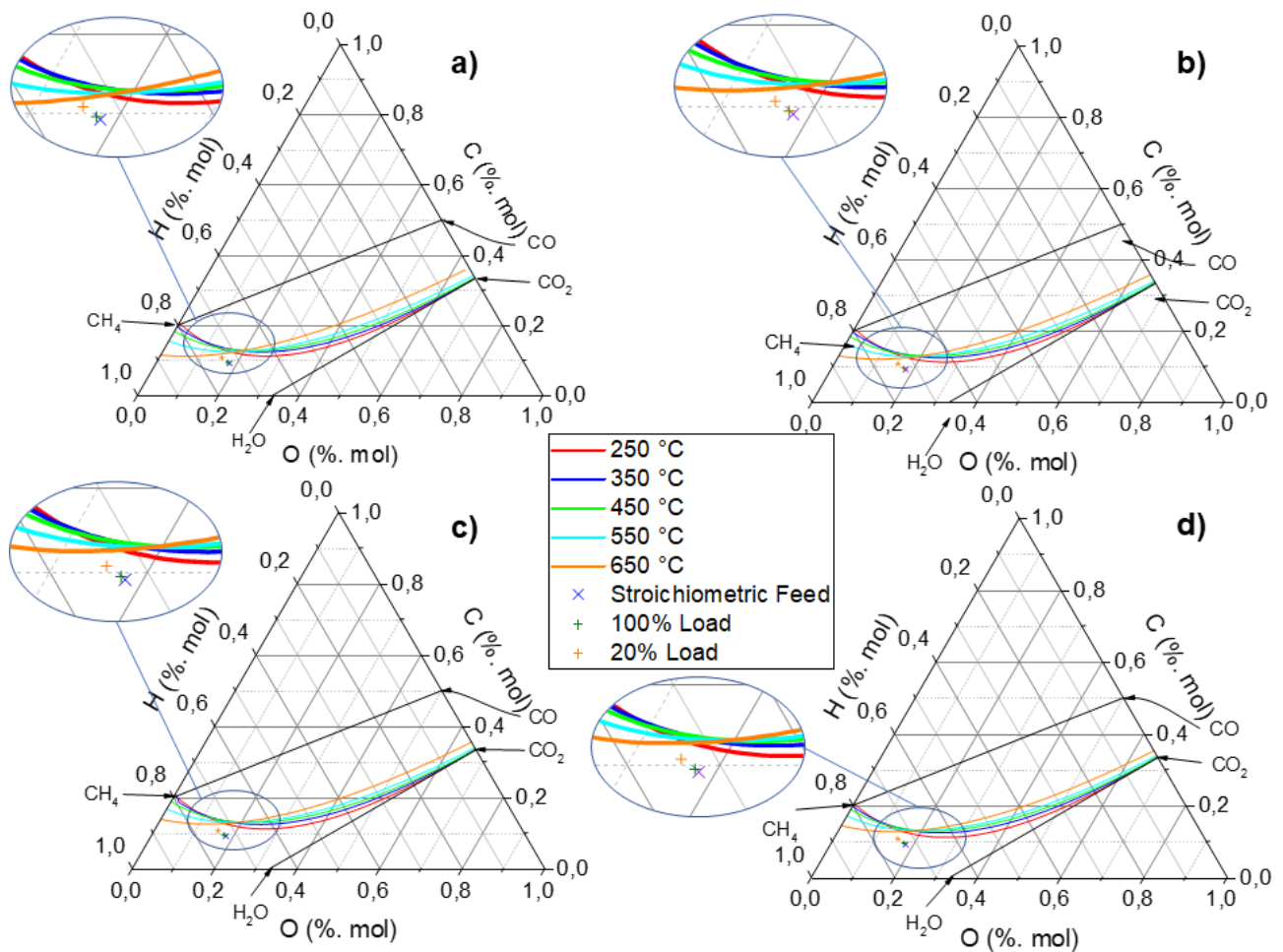
Figure 2-14. C-H-O ternary diagram at: a) 4 bar, b) 6 bar, c) 8 bar and d) 10 bar of total pressure

From the results, at low total pressure and at high temperature the carbon deposition boundary is very close to the feed of the methanation reactor. This may cause solid carbon formation and carbon deposition in a refrigerated fixed bed reactor because in this type of reactors there is a steep temperature profile and the maximum temperature that can be reached is in the neighbourhood of $600\,°C$. This issue can be avoided by recirculating water vapour to the reactor inlet moving the feed towards the stoichiometric concentration at the expense of increased compression cost and thermodynamic equilibrium. At higher pressure the carbon boundary move away from the operating condition and this problem should not present itself (at least from a thermodynamic standpoint).

41

Chapter 3

Kinetic and aging modelling

This chapter deals with the experimental observation of a commercial methanation catalyst deactivation behaviour during operation. Very few studies investigate the stability of the catalyst in real operating conditions. Bartholomew et al. [105], [106] have studied the metallic surface area loss in hydrogen and hydrogen/water atmosphere. They have found that loss of nickel surface area is caused support collapse and nickel particle growth. Sehested et al. [107], [108] have performed a similar study for steam reforming nickel supported catalysts. None of these studies supplied operando CO_2 methanation performance. Rostrup-Nielsen et al. [109] have studied the sintering of a commercial nickel based catalyst for methanation of CO at high temperature (600-700 °C). The study was conducted on catalyst samples from a pilot plant that operated for over 8000 h long tests. Abellò et al. [54] have performed long term tests (500 h) and up to 500°C on highly loaded nickel catalysts. They found that the catalyst maintains its activity and selectivity with little nickel particle growth. Koschany et al. [110] observed a strong deactivation on a co-precipitated nickel catalyst in a 320 h long test carried out at 380 °C. They have also reported a correlation between the particle average size and the weight time yield. Furthermore, they did not observe any correlation with the BET surface area. A recent study by Ewald et al. [111] has analysed with great detail the cause of methanation nickel based catalysts between 300 and 350°C and in tests up to 168 h long. They have found that sintering of the of nickel particles is the main cause of deactivation for co-precipitated samples. For the impregnated samples both the surface area and nickel particle growth were the main cause of deactivation. They have also fitted activity data with a power low model in isothermal conditions. None of the above studies have provided a complete methanation kinetic model containing both the intrinsic kinetic model and the aging behaviour. This is a crucial aspect in order to be able to correctly design a reliable methanation reactor system.

The experiments were carried out in lab scale test rig in process relevant conditions of temperature and pressure (i.e. 5 bar and 270-500 °C). The aged samples were then characterized in terms of total surface area (BET), X-ray powder diffractometry (XRD) and temperature programmed combustion (TPC) in order to determine the aging cause.

The intrinsic kinetics of the catalyst was determined from a separate set of experiments meant to evaluate the catalyst activity. Special care was taken in order to avoid the degradation of the catalyst during these experiments. This was achieved by measuring at regular intervals the activity of the catalyst and comparing it with the same test formerly performed. Different kinetic rate expressions were proposed based from literature and derived from different reaction mechanism by using LHHW approach. The resulting kinetic parameters were determined by using a least squares regression algorithm. The models were distilled to the best performing ones by parameter sensitivity analysis and by comparing the mean squared errors (MSE).

Finally, an aging model was proposed, and the parameters of this model have been determined by using the aging data. Thus, a complete kinetic model was obtained describing both the intrinsic kinetics of the catalyst and the aging behaviour.

3.1   Experimental setup

Both catalytic activity and catalyst aging experiments were carried out on a newly designed test unit allowing operation up to 500°C and 30 bar (Figure 3-1). All the involved gases come from pure gas bottles. The individual gases are mixed in the correct proportion using for each gas a dedicated mass flow controller. A 4-way valve system allows for the feed mixture to be analysed before switching it to the reactor. The reactor is made of a stainless-steel tube with an inner diameter of 8 mm. Inside the reactor a 1/8-inch thermocouple well is placed that allows for the measurement of the reaction temperature along the axis of the fixed bed by moving the thermocouple. The reactor is heated by an electrical heating jacket controlled using a thermocouple placed on the reactor outer wall or the inner thermocouple. The product gas coming out of the reactor is cooled to room temperature and water is condensed and collected inside a tank. The pressure inside the unit is maintained to the desired value by a back-pressure controller and two more pressure transducers are used to monitor the pressure at reactor inlet and outlet. Different safety valves are placed on the gas lines in order to guarantee safe operation. The gases are analysed using a multi-channel Emerson X-Stream gas analyser equipped with non-dispersive infrared (NDIR) sensors for CO, CO_2 and CH_4 and a thermal conductivity (TCD) detector for H_2 measurements. Each measurement channel was calibrated ('zero' and 'span' calibration) using certified bottled gas/es mixtures. An optional Agilent 7890B gas chromatograph was used to identify eventual reaction by products. The GC is equipped with a HP-PLOT/Q column (30 m length, 530 μm diameter and 40 μm film thickness) and a HP-PLOT Molesieve column (30 m length, 530 μm diameter and 50 μm film

thickness) connected in series. Two detectors also connected in series, a TCD and a flame ionization detector (FID), complete the GC setup.
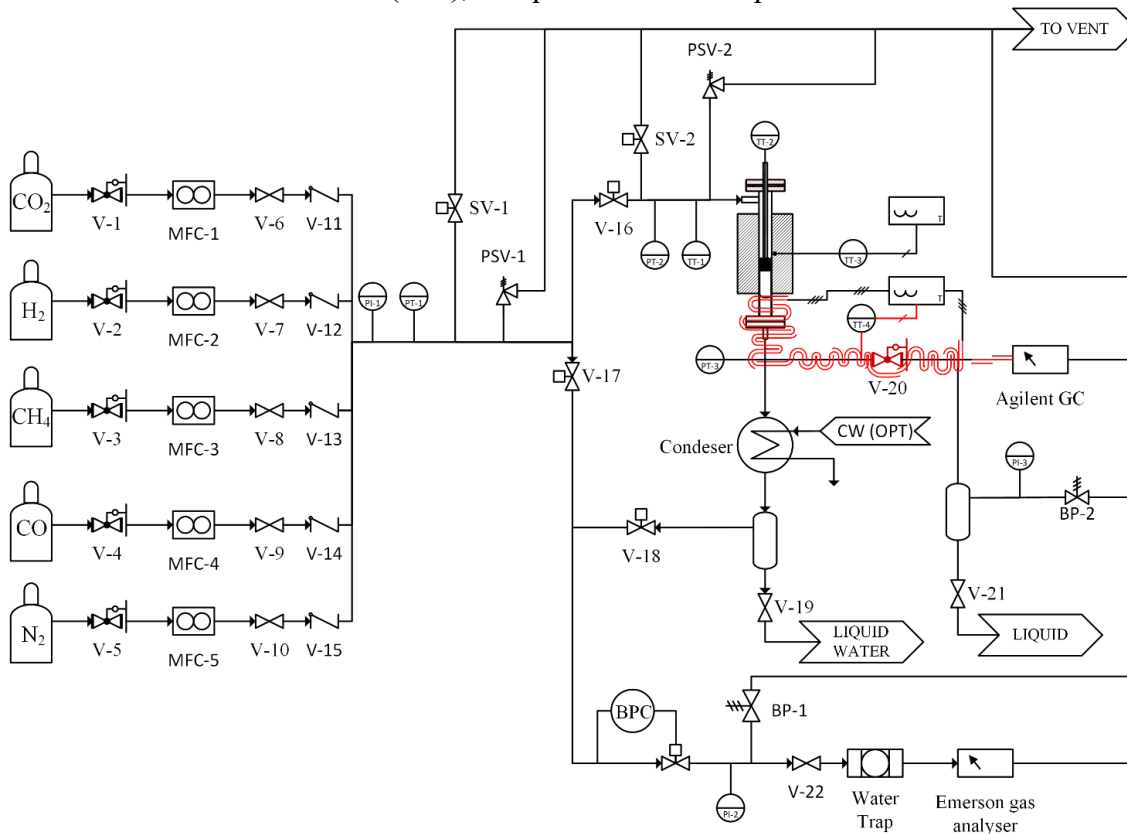
Figure 3-1: Pressurized catalytic testing setup

The activity tests used for the intrinsic kinetic model parameter regression were performed on 75 mg catalyst samples. In order to further reduce the risk of being in diffusion regime instead of kinetic regime, the catalyst sample was crushed and sieved to obtain a granulometry between 106 and 212 μm. For fluid dynamic reasons the catalyst was diluted in a 1 to 5 ratio with silicon carbide. The aging tests were performed on 200 mg unaltered catalyst samples in order to have the closest representation of the behaviour of the catalyst inside the real reactor. Two feed compositions were tested during the aging experiments: in the first case a $CO_2/H_2/N_2$=16/64/20 gas mixture is fed to the reactor while in the second case 6% of methane was added. These two compositions were identified through the process modelling of a methanation line with gas separation and recycling. The simulations and results are reported in a previous study [78]. The test matrix is summarized in Table 3-3.

Both temperature and product gas composition were logged during the whole test length at regular time intervals. Prior to the kinetic measurements the catalyst is stabilized over one night by keeping it on stream. The catalyst is stabilized at the maximum operating temperature of the kinetic tests.

The aged samples were characterized in terms of BET surface area, pore volume and mean pore diameter using N_2 adsorption isotherms. The measurements were carried out using a Micrometrics TriStar II 3020. Prior to the

45

measurements the samples were degassed at 200°C under nitrogen flow for two hours.

Carbon deposition is thermodynamically unfavoured in the testing conditions[78], [104]. However, absorbed carbon species could form as reaction intermediates (see step 5b in Table 3-4). This could lead to carbon deposition caused by difference in generation and consumption rates. Therefore, a temperature programmed combustion was performed on the aged catalysts. The catalyst samples were placed in a U tube quartz reactor and degassed from adsorbed CO_2 at 400 °C for 30 minutes under nitrogen flow. Afterwards the samples were cooled down to ambient temperature. The combustion was performed by feeding the reactor with a gas stream containing 2% of O_2 in nitrogen and heating the system with a 5°C/min ramp up to 800°C. The outlet gas composition was monitored with the same Emerson X-Stream 5 channel gas analyser.

3.2   Catalyst aging tests

The tests were performed on a commercial Ni/Al_2O_3 based catalyst with a nickel loading that ranges between 14-17 wt.%. The proprieties of the catalyst are summarized in Table 3-1.

Table 3-1: Catalyst proprieties [112], [113]

Propriety	Value
Catalyst density (ρ_p)	1274 kg m^{-3}
Specific surface area	222 m^2 g^{-1}
Mean pore diameter (d_{pore})	8.2×10^{-9} m
Granulometry	300±400 μm (340 median)
Catalytic bed porosity (ε_b)	0.41
Internal porosity (ε_p)	0.59
Equivalent catalyst thermal conductivity (k_e)	0.67 W m^{-1} K^{-1}
Catalyst heat capacity (Cp_s)	1063 J kg^{-1} K^{-1}

The catalyst is pre-reduced by the manufacturer for a quicker reaction start-up and to allow a lower activation temperature procedure. Before the tests, the catalyst samples were activated in situ at 260 °C for 5 h with a 30% H_2 in N_2 gas flow. The aging tests were performed on 200 mg unaltered catalyst samples in order to have the closest representation of the behaviour of the catalyst inside the real reactor. Two feed compositions were tested during the aging experiments: in the first case (Test 1) a $CO_2/H_2/N_2$=16/64/20 gas mixture is fed to the reactor while in the second case (Test 2) a 59.2 % H_2, 14.8% CO_2, 6% of methane and 20% N_2 was used. These two compositions were identified in with the process modelling done the previous chapter. The test matrix is summarized in Table 3-2. Both temperature and product gas composition were logged during the whole test length at regular time intervals.

Table 3-2: Aging tests matrix

Aging tests	
Space velocity	$150\ l_{STP}\ g_{cat}^{-1}\ h^{-1}$
Temperature	270, 380, 425 and 500 °C
Total pressure	$5\ bar_{abs}$
Feed composition	64% H_2, 16% CO_2 and 20% N_2 59.2% H_2, 14.8% CO_2, 6% CH_4 and 20% N_2
Test length	~100 h

In Figure 3-2 and Figure 3-3 the CO_2 conversion and CH_4 yield are reported for the aging tests carried out at various temperatures and feed compositions. On the one hand, the tests carried out at low temperature (270°C) have not shown, within experimental error, a methane yield (or CO_2 conversion) variation during the ~100 h long aging run. On the other hand, the tests carried out at higher temperatures have shown a decrease both in terms of methane yield and reaction temperature. The observed methane yield loss is due to two non-independent phenomena. During the aging process the aging of the catalyst causes the reduction of the conversion rate. Therefore, also the heat production reduces translating in the reduction in the catalytic bed temperature. Hence, this causes an amplification of the observed methane yield reduction caused by both the catalyst aging and the decrease in reaction temperature. This occurs because the controlled temperature is that of the oven in which the reactor is placed.

The tests aged with 6% of methane in the feed gave similar results compared to the ones aged without methane in the feed. Therefore, the presence of methane in the feed stream does not affect the catalyst stability. The CO_2 conversion and CH_4 yield loss at the end of the aging tests is summarized in Table 3-3. The decay of the CO_2 conversion and CH_4 yield follow similar trends at a first glance. A light increase in the CO yield was also observed during the aging tests. This could be caused by selectivity change of the catalyst but also by the loss of activity of the catalyst and operating conditions (carbon monoxide could be an intermediate in the reaction mechanism).

In Figure 3-3 c and d, at the end of the aging run, the temperature was raised back to the initial value in order to observe the real loss in catalytic activity, not biased by a lower reaction temperature. By imposing the initial temperature for the test at 425°C, the effect of the temperature drop on the yield was removed, which halved the yield loss. The test at 500°C appears not to be affected by the temperature drop and no yield increase was observed when the temperature was restored to the initial value. This is probably due to the proximity of the equilibrium.
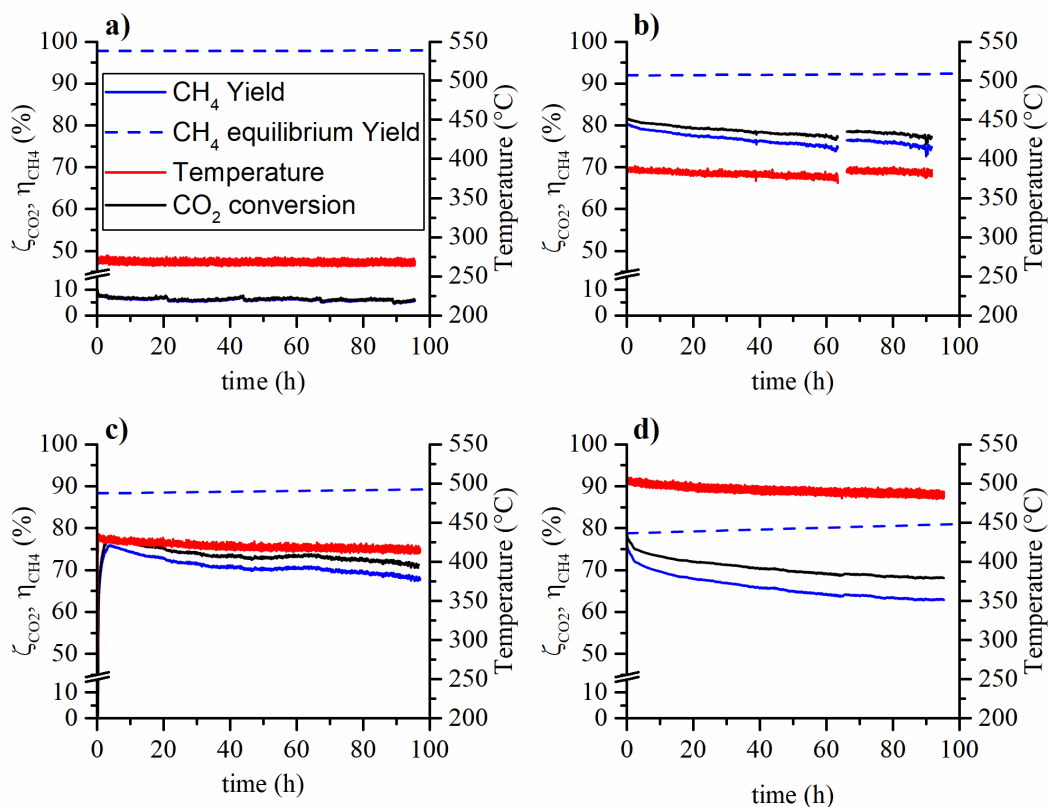
Figure 3-2: Aging tests at 5 bar, weight hourly space velocity (WHSV)=150 l$_{STP}$ g$_{cat}^{-1}$ h^{-1}, feed composition 16% CO$_2$, 64% H$_2$ and 20% N$_2$ and a) 270 °C, b) 380 °C, c) 425°C and d) 500°C
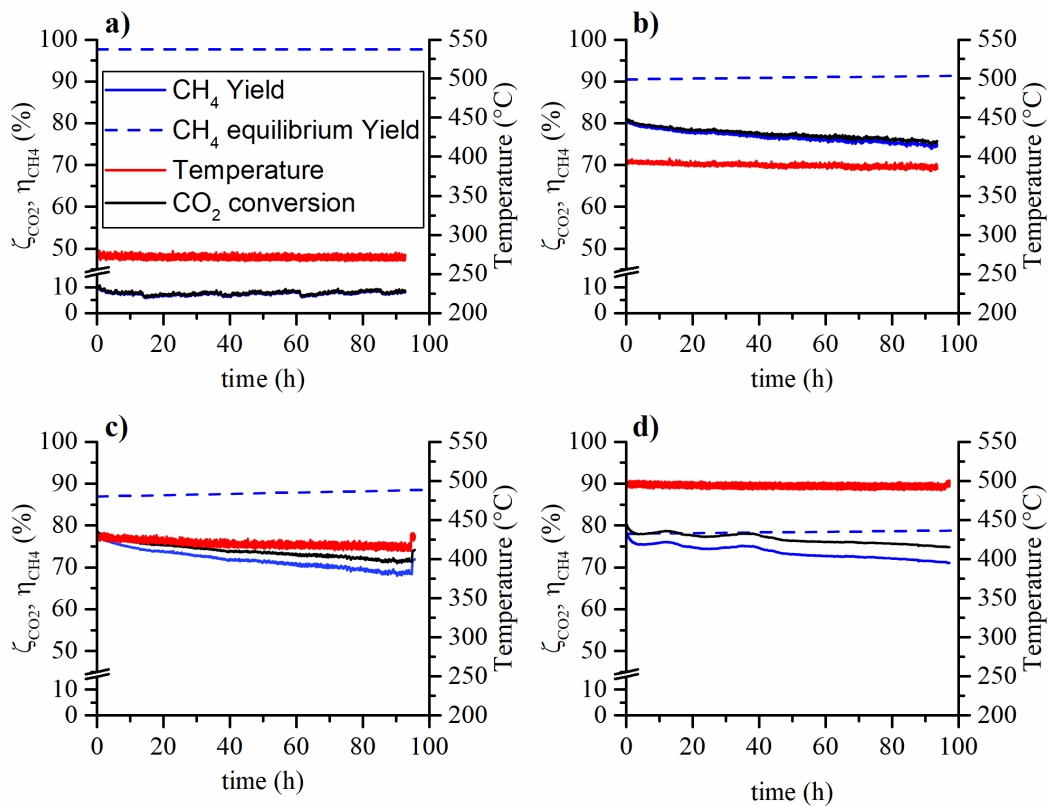
Figure 3-3: Aging tests at 5 bar, WHSV=150 l$_{STP}$ g$_{cat}^{-1}$ h^{-1}, feed composition 14.8% CO$_2$, 59.2% H$_2$, 6% CH$_4$ and 20% N$_2$ at 5 bar and a) 270 °C, b) 380 °C, c) 425°C and d) 500°C

Temperature (°C)	Test 1			Test 2		
	CO_2 conversion	CH_4 yield	CO yield	CO_2 conversion	CH_4 yield	CO yield
270	0%	0%	0%	0%	0%	0%
380	-4%	-5%	+1.1%	-5%	-5%	+0.4%
425	-6%	-7%	+1.4%	-9% (-4%) [a]	-8% (-4%)[a]	+1.7% (+1.1)[a]
500	-7%	-10%	+2.2%	-6%[b]	-7%[b]	+1.1%[b]

[a] the value between brackets represents the real variation measured after restoring the initial temperature

[b] the test was near equilibrium conditions

An ON-OFF run was conducted at 425°C in order to asses if the shutdown and start-up of the reaction has any influence on the catalyst performance. A total of 12 on-off switches were carried out during a 100h long run. In Figure 3-4 the results are reported in terms of normalized methane yield define as the ratio between the yield at time t and the yield at the beginning of the run. No difference was observed between the straight run and the ON-OFF test. Therefore, the aging process is not influenced by the transients generated with the repeated start-up and shutdown of the reaction and it can be concluded that aging depends on the time on stream and reaction conditions only.
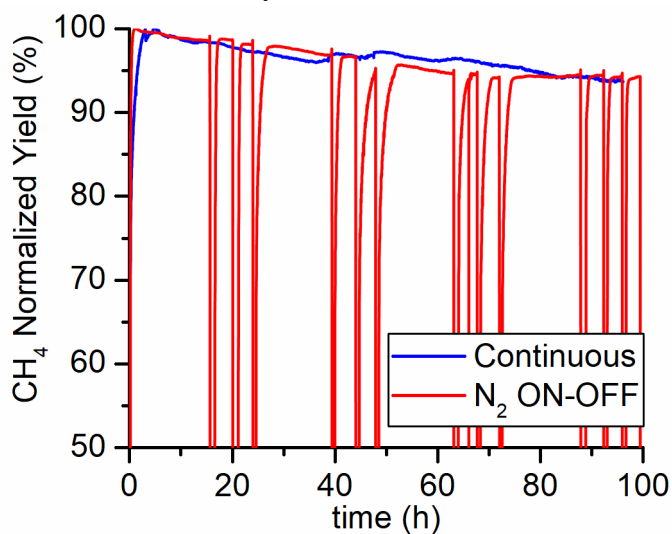
Figure 3-4: : Continuous versus ON-OFF 100 h test carried out at 425°C, 5 bar, feed flow rate of 150 $l_{STP} \, g_{cat}^{-1} \, h^{-1}$ and composition CO₂/H₂/N₂=4/16/5. Nitrogen was used to flush the reactor during the OFF phases.

3.2.1 By-products

The main by-product of the CO_2 methanation is carbon monoxide that can form through the reverse water gas shift reaction. In Figure 3-5 the CO yield evolution during the 100h long test is reported. As the catalyst ages an increased selectivity towards carbon monoxide is observed.
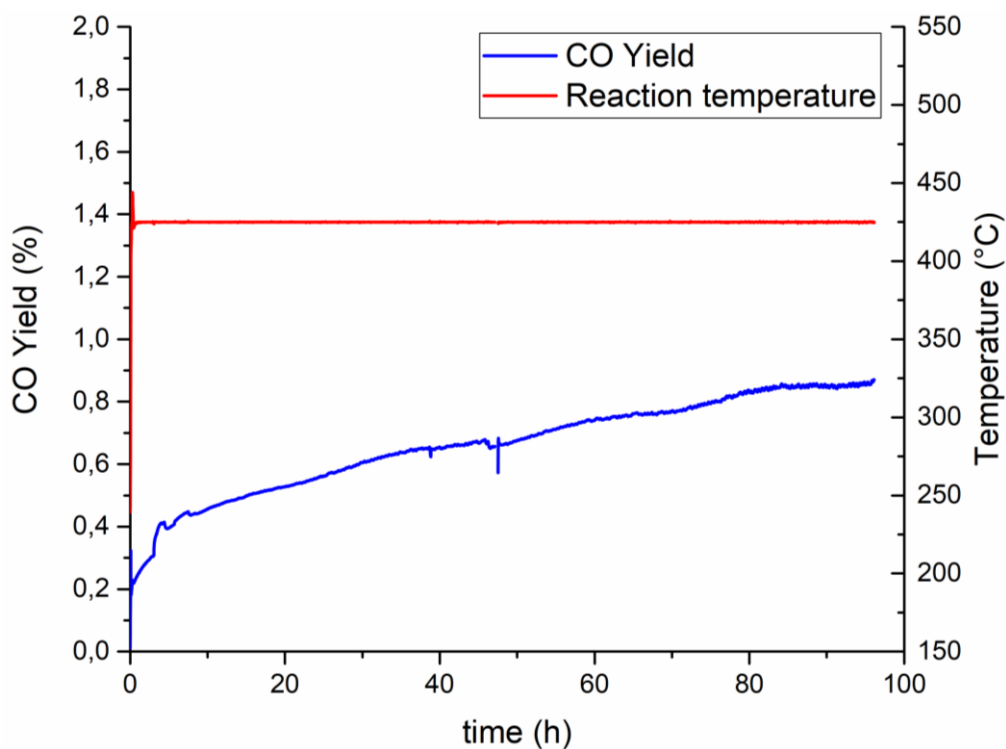
Figure 3-5: CO yield evolution during the 100h long test carried out at 5 bar, 425 °C and $CO_2/H_2/N_2$=16/64/20

In order to identify other reaction by-products an optional Agilent 7890B gas chromatograph was used. With the GC the gas is sampled directly from the reactor outlet through a heated sampling line. This allows for the analysis of the gas without condensing the water and other eventual condensable components. The GC is equipped with a HP-PLOT/Q column (30 m length, 530 µm diameter and 40 µm film thickness) and a HP-PLOT Molesieve column (30 m length, 530 µm diameter and 50 µm film thickness) connected in series. Two detectors connected in series, a TCD and a flame ionization detector (FID), complete the GC setup. A complex analysis method was implemented to be able to identify the following compounds: CO_2, H_2, H_2O, N_2, CH_4, CO, ethane, propane, butane, ethylene, propylene, acetylene, methanol, and dimethyl ether. Helium was used as carrier gas with a flow rate of 7 ml/min. The analysis was performed according to a temperature program that ranged between 50 and 230 °C, with different heating and cooling rates of the oven, in order to correctly separate the different components. The GC was calibrated with certified bottled gas mixtures from the previously mentioned provider. In Figure 3-6 the two chromatograms obtained for a sample during the 100h test are reported. On the FID channel the hydrocarbons are measured while on the TCD the other gases.

50
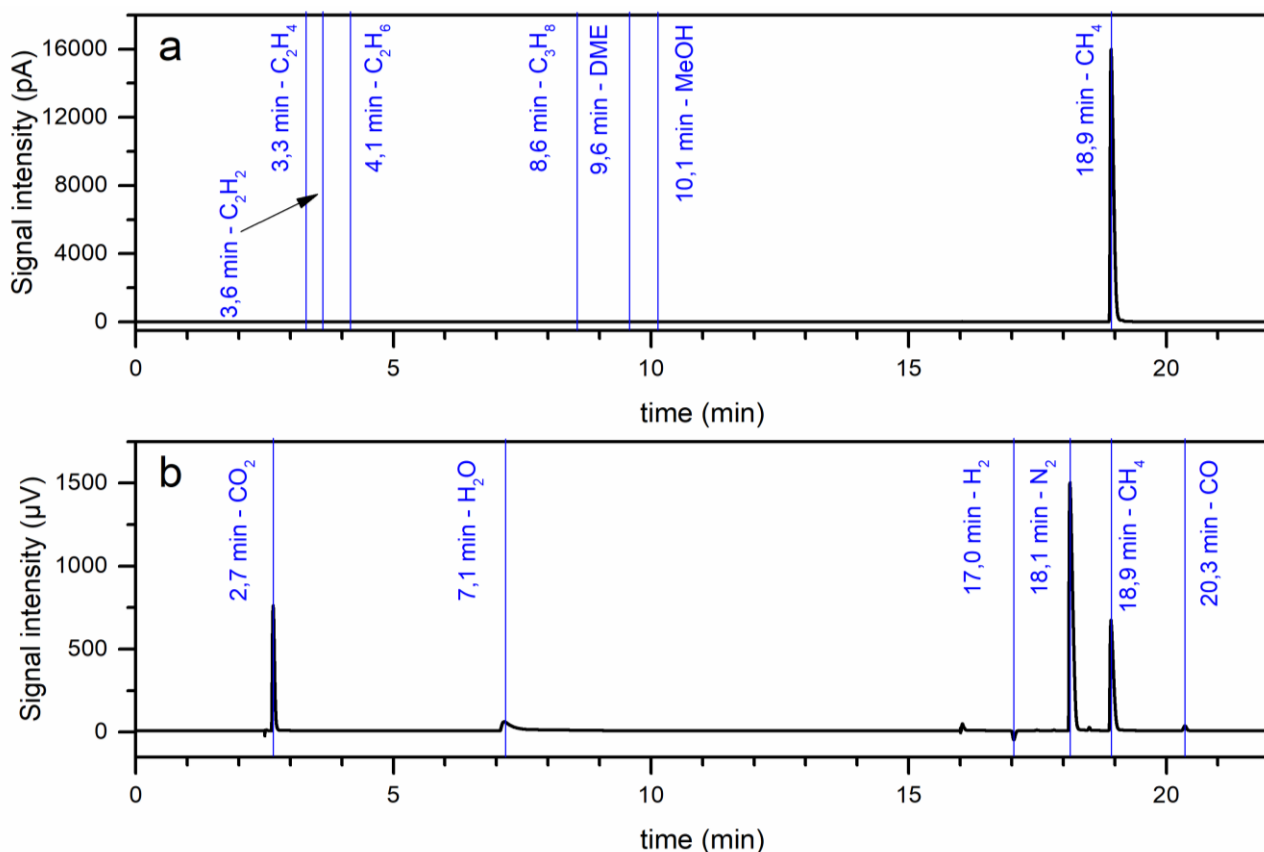
Figure 3-6: GC chromatogram of a sample during the 100h long test a) FID signal and b) TCD signal

The analysis with the GC revealed that ethane is also a reaction by-product. The amount of ethane produced is around three orders of magnitude less than CO (1100 ppm of CO versus 4 ppm of ethane after 2 hours of operation) resulting in a selectivity less than 0.1% towards ethane. Ethane yield increases when pressure is increased while a maximum of selectivity is reached at 350°C (Figure 3-7 a). An increase of the ethane concentration during the 100h test was observed passing from 4 ppm to 8 ppm (Figure 3-7 b).
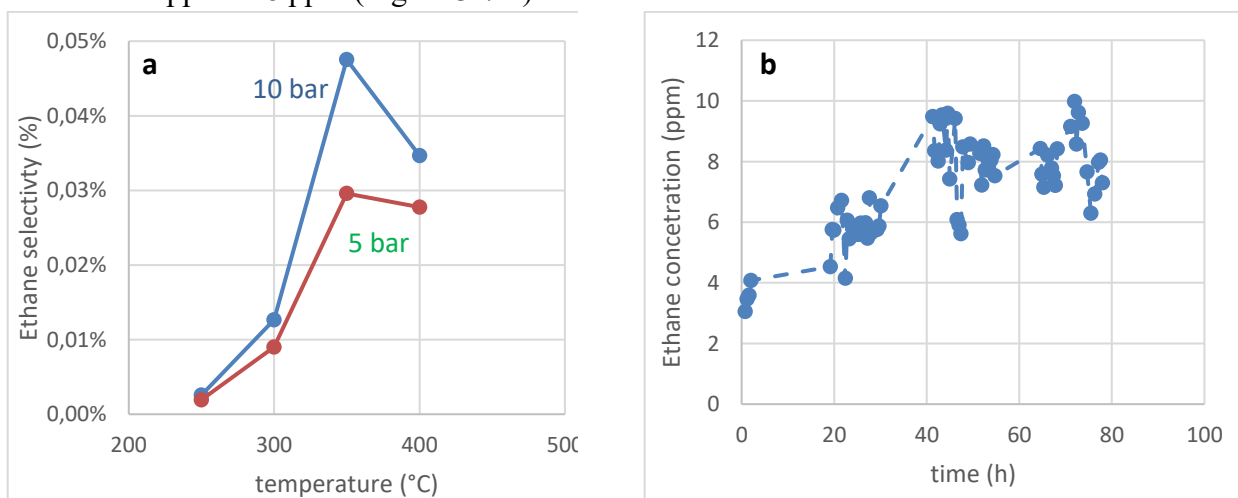
Figure 3-7: a) ethane selectivity during an activity test carried out at 5 and 10 bar, GHSV=100000h^{-1} CO$_2$/H$_2$/N$_2$=16/64/20; b) ethane evolution during the 100h long test

The product water was also analysed for components that may form during the reaction and condensate along with water (i.e. formic acid, methanol). Water samples were collected, from the water collection tank of our test rig, every 12 h during the long-term tests. The samples were then analysed in with our Shimatzu Priminence high precision liquid chromatography system (HPLC). The HPLC is equipped with a Rezex ROA-Organic acid H+ (8%) column (300 mm length, 7.8 mm diameter) and a refractive index detector (RID). The mobile phase is made of 0.005 N sulfuric acid (Sulfric Acid HPLC grade from Sigma-Aldrich diluted in Milli-Q water). The analysis was carried out in isothermal conditions at 50°C with a mobile phase flow rate of 0.7 ml/min. The quantitative analysis was performed using homemade standard solutions of the analyte diluted in Milli-Q water.

In Figure 3-8 one of the analysis results using the HPLC is reported. The first peak is due to the water present in the sample. At the elution time of formic acid and methanol no peaks were observed on the RID sensor. The two peaks around the methanol elution time were associated to carbonate and bicarbonate species caused by CO_2 solubilization in the product water. Methanol was observed in the product water at temperatures for tests carried out below 300°C and in none of the tests at higher temperature. The concentration was near the limit of sensitivity of the instrument at around 10 ppm of methanol. Formic acid was never observed in the testing conditions and no other peaks were observed. Therefore, it can be safely concluded that formic acid and methanol do not form during the aging process as a by-product.
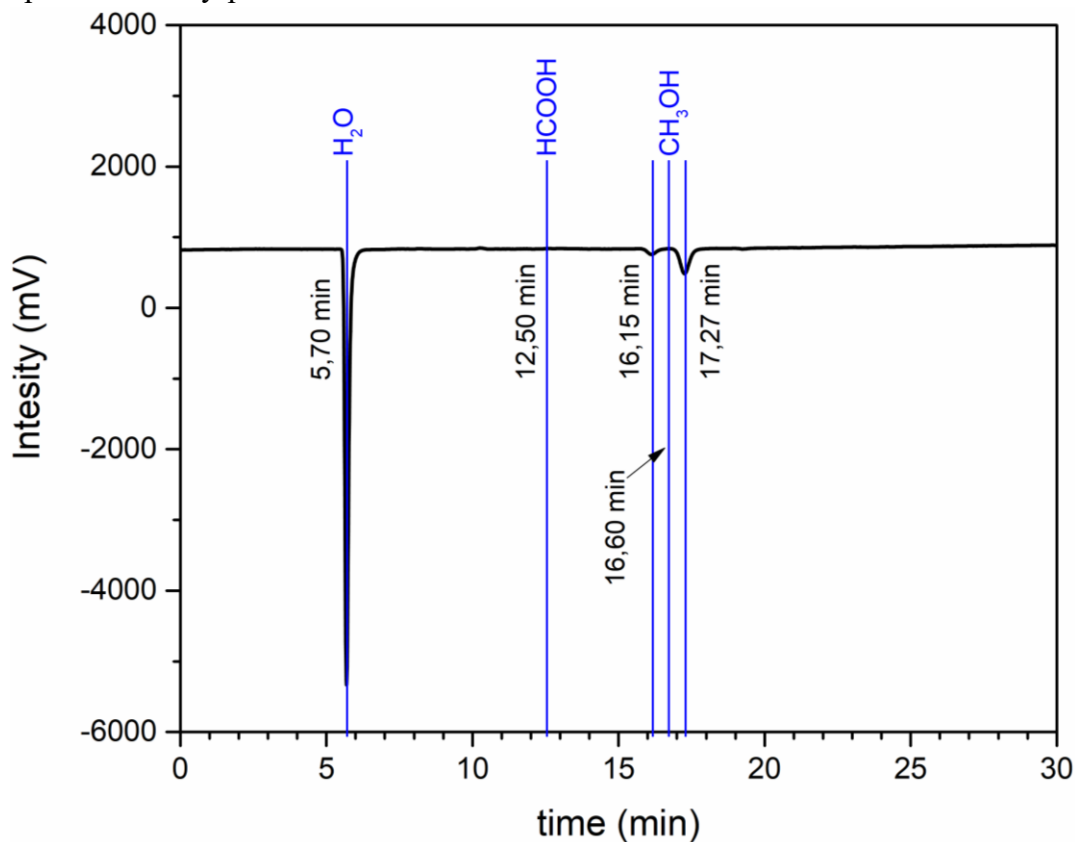
Figure 3-8: HPLC chromatogram of a water sample during the 100h long test

3.2.2 Aged samples characterization

At this point a more in-depth analysis of the exhaust catalyst was performed. The techniques that were used are:

- ➢ Temperature programmed combustion to investigate the possible formation of carbon deposition formed due to kinetic reasons.
- ➢ X-ray powder diffractometry was used to identify if the formation of nickel aluminates ($NiAl_2O_4$) causes the loss of nickel active phase
- ➢ Total surface area and porosimetry measurements were used to investigate if sintering of the support could lead to a loss in the active phase.

Temperature Programmed Combustion (TPC)

The first deactivation mechanism considered is carbon deposition. This phenomenon produces solid carbon on the catalyst surface and blocking pores causing the isolation of the active phase from the reagent gasses. The thermodynamic analysis excluded the possibility of solid carbon formation but, it still may occur for kinetic reasons if the reaction mechanism contemplates the formation of carbonium phases as reaction intermediates. The exhaust catalysts were tested using a temperature programmed combustion (TPC). The procedure consists in following steps:

1. 100 mg of exhaust catalyst is weight and placed inside a quartz tube reactor.
2. The reactor is placed inside an oven and connected to the gas lines.
3. A feed stream containing 2% of O_2 in nitrogen is fed to the reactor.
4. The oven is set to perform a heating ramp of 5 °C/min from room temperature to 800 °C.
5. The exhaust gas is analysed by an online gas analyser monitoring the amount of combustion products in the outlet stream (only CO_2 and no CO is formed because excess oxygen is fed).

The results of the TPC on the catalysts used in the methane fed long-term runs are reported in Figure 3-9 a. It can be observed the CO_2 evolution trend related to the reactor temperature. The procedure initially applied did not have a surface cleaning step causing the release of chemisorbed CO_2 residue from the long-term test. In fact, the amount of CO_2 released up to 400 °C is inversely proportional to the temperature at which the long-term test was performed. The temperature range in which this occurs was also investigated with a CO_2-temperature programmed desorption (TPD) reported in Figure 3-9 b. The initial part of the curve represents the physisorbed CO_2 release while the peak around 250 °C is the chemisorbed CO_2 being released.

The carbon deposited on the catalyst surface generally starts to oxidize at temperatures higher than 450 °C [114], [115]. In our case very small amounts of CO_2 is present in the exhaust stream at temperatures above 450 °C.
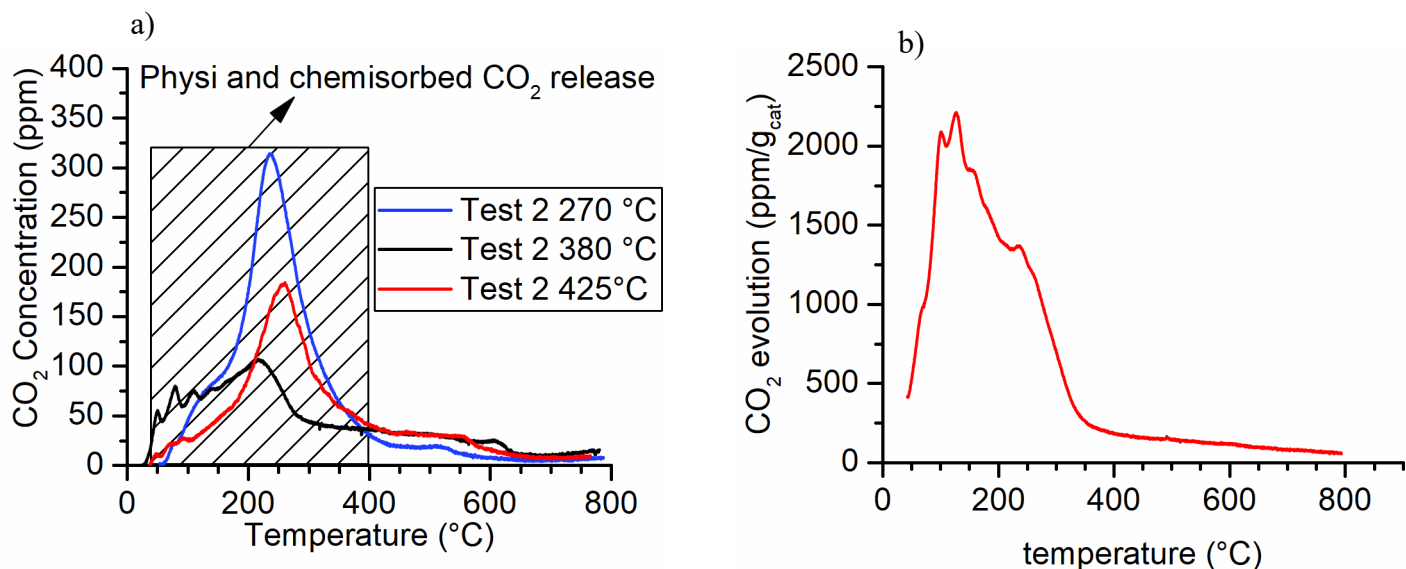
Figure 3-9: a) TPC of the exhaust catalyst from the long-term tests with methane in the feed b) CO_2 - TPD

In order to be able to quantify the amount of CO_2 generated during the oxidation portion a pre-treatment to clean the catalyst surface from physisorbed and chemisorbed CO_2. The analysis protocol implemented consists in heating the sample to 400 °C and keeping it in nitrogen flow for 30 minutes. Afterwards the sample is cooled to room temperature and the TPC can be applied as previously done. The full procedure is reported in Figure 3-10. By performing these steps, the CO_2 measured during TPC should be related only to carbon deposition. In Figure 3-11 the results are reported and it can be observed that the CO_2 evolution at temperatures lower than 400 °C has been greatly reduced thanks to the pre-treatment. However, a small quantity is still present especially on the low temperature long-term sample.
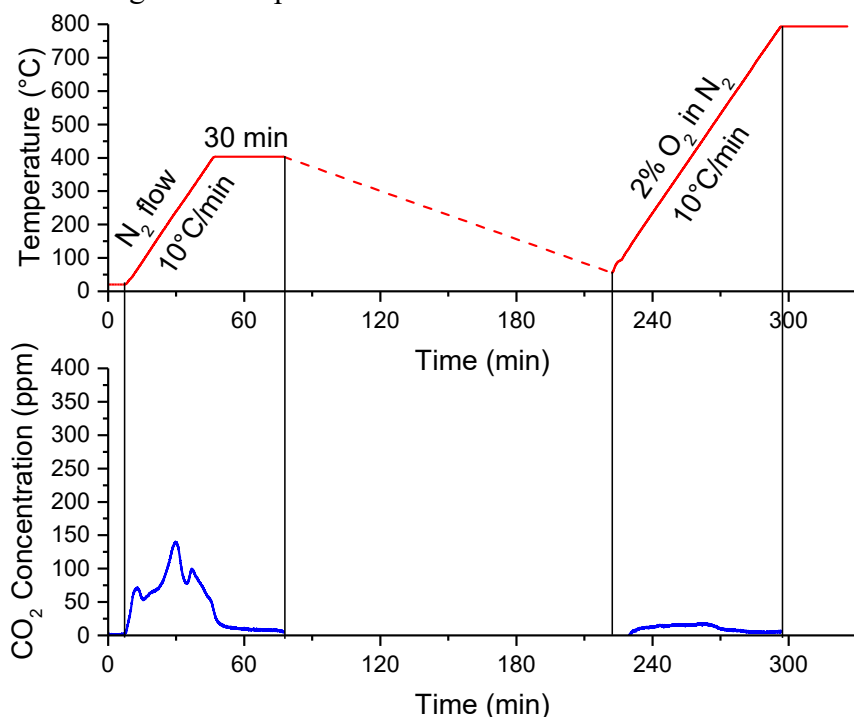
Figure 3-10: TPC procedure with pre-treatment
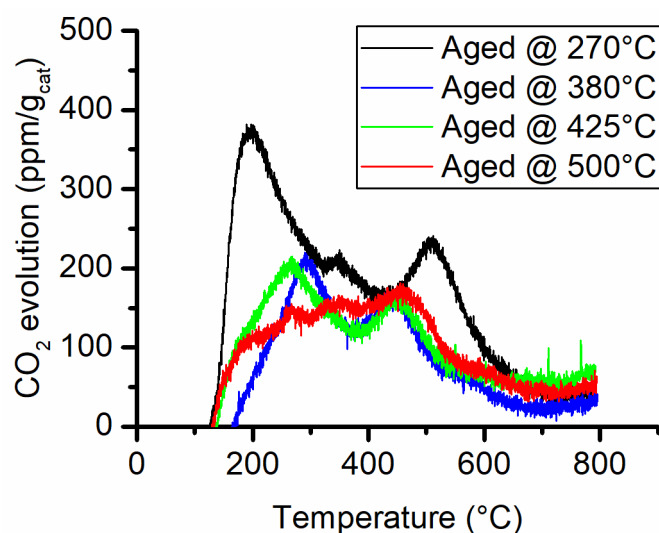
Figure 3-11: TPC test 1 with pre-treatment

The comparison of the TPC results with the CO_2-TPD (Figure 3-9 b) does not reveal a substantial increase in the CO_2 generation at temperatures higher than 400 °C (pretreatment temperature): this means that such a CO_2 emission cannot be attributed to the oxidation of eventual coke deposits. Furthermore, carbon deposits on Ni/Al_2O_3 catalysts generally starts to oxidize at temperatures above 500°C [116]–[118]. Therefore, the CO_2 evolution peaks below 500°C are probably caused by leftover carbonates decomposing. From the analysis of the curves in Figure 3-11, the main contribution to CO_2 emissions occurs below 500°C, therefore attributed to the desorption of CO_2, while above this limit the oxidation of negligible quantities of contaminating organic material, occurring during catalyst manipulation, might explain the observed phenomenon. The total amount of CO_2 generated was calculated by integrating the desorption curves and all the CO_2 formed was supposed to be caused by carbon deposition (worst case scenario). The results are reported in Table 3-4. The amounts are ridiculously low to explain the observed deactivation. Another important parameter reveals that the amount of equivalent carbon (calculated as the sum of CO_2 and CH_4 fed to the reactor) that encountered the catalyst and converted to solid carbon is less than 1 part per million. This allows us to exclude with a great degree of certainty as the main deactivation process and further investigation is required.

Table 3-4: TPC Test 1 quantitative analysis

Test	Solid carbon yield vs equivalent carbon in contact	Carbon to catalyst ratio
(°C)	($g_{to\ C}/g_{C\ in\ contact}$)	(mg $_C$/g $_{cat}$)
275	$5.2 \cdot 10^{-7}$	1.21
380	$2.6 \cdot 10^{-7}$	0.62
425	$3.2 \cdot 10^{-7}$	0.77
500	$3.1 \cdot 10^{-7}$	0.74

X-ray diffractometry

The catalyst samples were analysed through x-ray diffraction using Cu Kα radiation (X'Pert Philips PW3040 diffractometer, 2θ range = 5-90°, step size = 0.013°, counting time at 0.2 s/step). The peaks obtained through XRD pattern were compared with the reference patterns from the Powder Diffraction Files by International Centre of Diffraction Data (ICDD) database. Prior to the analysis the samples had to be crushed in order to obtain a powder. When analysing the small particle (~300μm) the counts of the XRD were too poor to conclude anything.

The reference patterns used to compare are the same used in a recent study on nickel based catalyst [111] and these are:

> ➢ Metallic nickel: Ni → 01-087-0712
> ➢ Nickel oxide: NiO → 01-078-0429
> ➢ Gamma alumina: γ-Al_2O_3 → 96-201-5531
> ➢ Nickel Aluminium Oxide: $NiAl_2O_4$ → 00-010-0339

In Figure 3-12 the XRD patterns of two aged samples and the reference fresh just activated sample are reported. The main reflection peaks of the reference patterns are all near one another, especially those of γ-Al_2O_3 and $NiAl_2O_4$. For the fresh and activated sample the peaks corresponding to the NiO persist (2θ=62.9°). The low activation temperature is not sufficiently high to reduce entirely nickel from oxide to metallic state. This aspect was also corroborated by the H_2-TPR analysis performed on the fresh catalyst (see Appendix). About 22% of the total hydrogen uptake takes place during the activation procedure. This corresponds to the same fraction of reduced nickel. The aged catalyst samples carried out at higher temperatures with respect to the activation temperature presented a reflection at 2θ=51.9° that was attributed to metallic Ni. The oxide reduction to the metal form is caused by the high content of hydrogen present in the gas stream during the methanation process. Furthermore, this peak is not present in the freshly activated sample and could be a sign of Ni crystallite growth with consequent loss of dispersion and nickel exposed surface. The peak of γ-Al_2O_3 at 2θ=66.6° becomes less intense in the in samples aged at high temperature. This can be an indication of evolution of the alumina support, that partially turns into Ni aluminate, with consequence the loss the porous structure of the support. Moreover, a secondary peak assigned to $NiAl_2O_4$ can be observed at 2θ=65.5°.

Due to the high overlapping of the peaks the semi-quantitative analysis was not successful and is not reported.
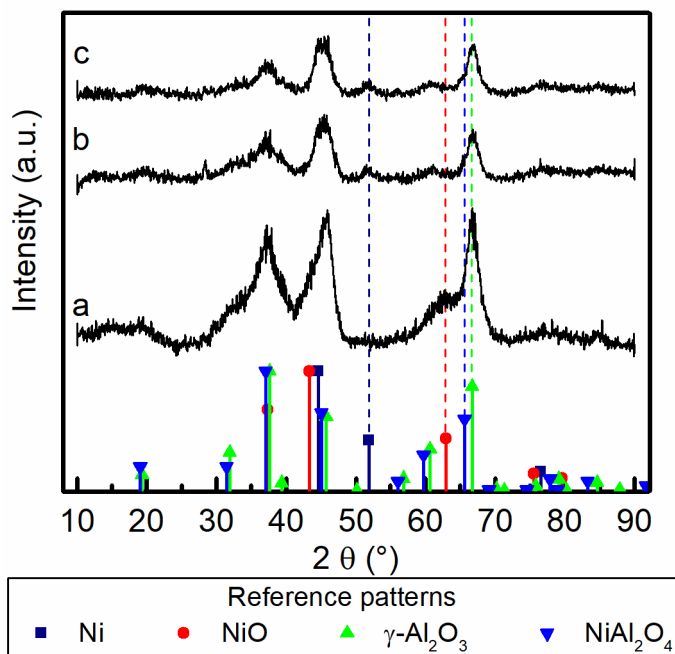
Surface area and porosimetry

The surface area of the catalyst samples was determined using the Brunauer-Emmett-Teller (BET) theory with N$_2$ adsorption isotherms. The isotherm measurements were carried out using a Micrometrics TriStar II 3020. Prior to the measurements the samples were degassed at 200°C under nitrogen flow for two hours prior to the adsorption measurements.

The N$_2$ adsorption isotherms obtained for the samples are reported in Figure 3-14. The samples have a Type IV isotherm, typical of mesoporous materials. The fresh, fresh reduced and aged at 270°C have a hysteresis resembling an H-2 type. Generally, H$_2$ hysteresis loops are ascribed to materials without a well-defined porous structure[119]. The Barrett-Joyner-Halenda (BJH) method was used to evaluate the pore size distribution [120]. In Figure 3-15 the pore distribution is reported. It was determined that the average pore dimension increases from ~6 nm to ~12 nm and complete loss of the micropores.

The surface area analysis, pore volume and average pore width are reported in Table 3-2. The surface area of the reduced sample and the fresh sample does not change within error. The sample aged at 270°C also does not show a decrease in surface area. This is also in agreement with the activity trend that remains constant during the entire duration of the test. The surface areas of the samples aged at higher temperature exhibit a significant decrease as the temperature of the aging test increases. The possible causes for this important reduction of surface area could be fouling and pore occlusion caused by carbon deposition or sintering of the support. The results from the TPC analysis did not reveal carbon deposition whatsoever. Hence, the cause of such an important decrease in surface area can

only be caused by the catalyst support sintering. In this case the support is incorporating the nickel active phase by surface rearrangement and pore closing. Furthermore, Bartholomew et al.[105], [106] have demonstrated that water increases highly the collapse of alumina support. These conditions are obtained in the high CO_2 conversion tests carried out at high temperature.

<p align="center">Table 3-5: Surface area and average pore width</p>

Sample	BET surface area[a] (m^2/g_{cat})	Pore volume[b] (cm^3/g_{cat})	Average pore width[c] (nm)
Fresh	221.8±5.1	0.44	6.2
Fresh after reduction	217.9±5.0	0.46	6.5
Aged @ 270°C	207.3±5.9	0.42	6.3
Aged @ 380°C	165.6±3.8	0.43	8.4
Aged @ 425°C	144.3±4.0	0.46	9.9
Aged @ 500°C	112.6±4.6	0.40	12.6

[a] BET fit for $0.05<p/p^0<0.35$
[b] single point pore volume evaluation at $p/p^0=0.99$
[c] calculated using BJH algorithm applied to the desorption branch of the isotherm
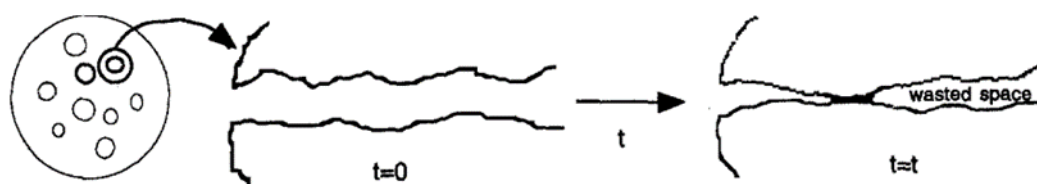
<p align="center">Figure 3-13: Representation of pore closing aging</p>
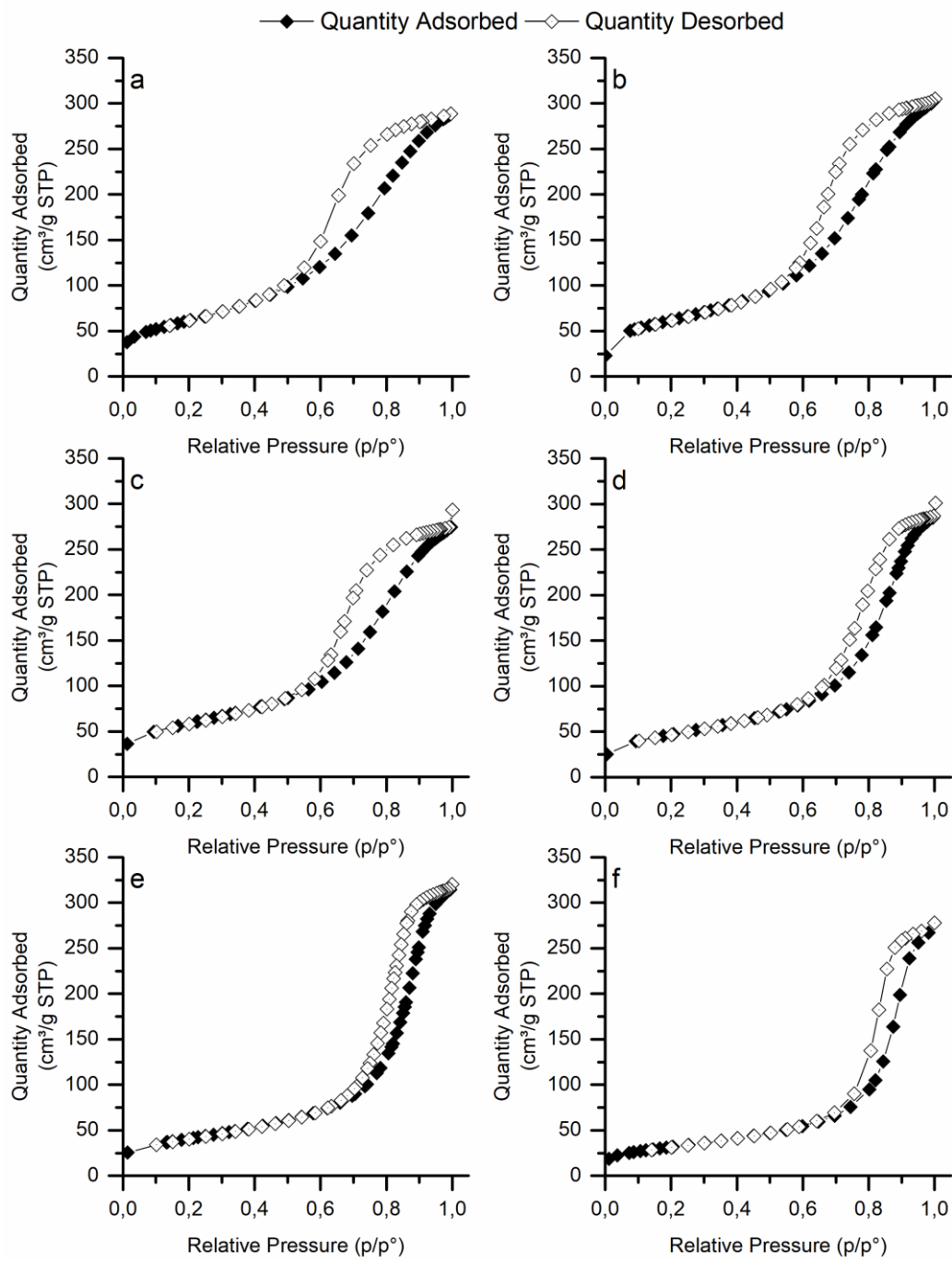
Figure 3-14: Nitrogen adsorption isotherms for the a) fresh sample, b) fresh reduced, c) aged @270°C, d) aged @ 380°C, e) aged @ 425°C and f) aged @ 500°C
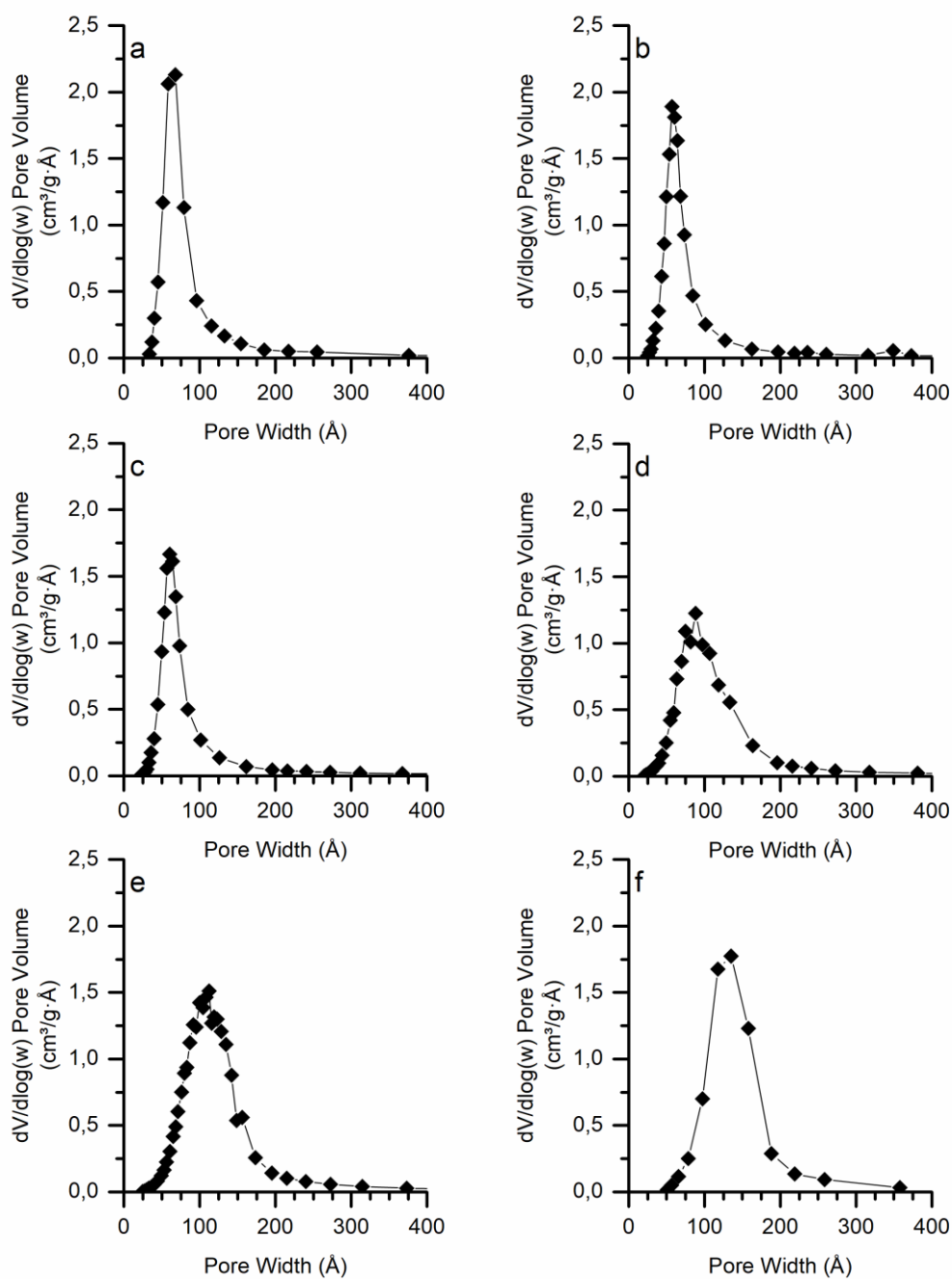
Figure 3-15: BJH desorption pore-size distribution curves for the a) fresh sample, b) fresh reduced, c) aged @ 270°C, d) aged @ 380°C, e) aged @ 425°C and f) aged @ 500°C

3.3 Catalyst activity measurements and kinetic modelling

The activity tests used for the intrinsic kinetic model parameter regression were performed on 75 mg catalyst samples. In order to further reduce the risk of being in diffusion regime instead of kinetic regime, the catalyst sample was crushed and sieved to obtain a granulometry between 106 and 212 μm. For fluid dynamic reasons the catalyst was diluted in a 1 to 5 ratio with silicon carbide.

Prior to the kinetic measurements the catalyst was stabilized over one night by keeping it on stream at the maximum operating temperature of the kinetic tests. The test matrix is summarized in Table 3-6.

<p align="center">**Table 3-6: Kinetic test matrix**</p>

Kinetic tests	
Space velocity	400, 600 and 800 l_{STP} g_{cat}^{-1} h^{-1}
Temperature	250, 300, 350 and 400 °C
Total pressure	5, 7.5 and 10 bar
Feed composition	H_2/CO_2=3.5-5.33

3.3.1 Computational method

An ideal plug flow reactor model was used to integrate the kinetic model. The mass balance is represented through the system of differential equations (3-43).

$$\frac{d\dot{n}_i}{dm} = \sum_{j=1}^{n_r} \nu_i R_j \tag{3-1}$$

Where $\dot{n}_i$ is the mole flow rate of species i, m is the mass of catalyst, ν_i is the stoichiometric coefficient of the component in reaction j, and R_j is the reaction of the key component j. By solving the mass balance, the methane and carbon monoxide yields can be calculated using equations (3-44) and (3-45).

$$\eta_{CH_4} = \frac{\dot{n}_{CH_4,out} - \dot{n}_{CH_4,in}}{\dot{n}_{CO_2,in} - \dot{n}_{CO_2,out}} \tag{3-2}$$

$$\eta_{CO} = \frac{\dot{n}_{CO,out} - \dot{n}_{CO,in}}{\dot{n}_{CO_2,in} - \dot{n}_{CO_2,out}} \tag{3-3}$$

The regression was performed by minimizing the sum of squared residuals of the methane and CO yields (3-46).

$$obj_s = \sum_{j=1}^{n_t} \left(\left(\eta_{CH_4,exp,j} - \eta_{CH_4,mod,j} \right)^2 + \left(\eta_{CO,exp,j} - \eta_{CO,mod,j} \right)^2 \right) \tag{3-4}$$

The parameter estimation procedure was carried out using MATLAB with the Statistics and Machine Learning Toolbox™. The procedure involved firstly the use of the genetic algorithm for an initial estimate of the model parameters and successively the use of the nonlinear fitting routines for the final minimization.

Local sensitivity analysis was performed in order to evaluate the behaviour of the objective function near the nearby the determined minima and to investigate the sensitivity of the model to the single parameters. The sensitivity analysis was evaluated by perturbating one parameter at a time in a ±25% range from the optimum value. For every perturbation of the parameter values the objective function is re-evaluated.

Different kinetic expressions were fitted to the experimental data. Since the amount of CO measured during the experimental campaign is not negligible, the kinetic model must account for its formation. The same approach was used for the derivation of the kinetic model is found in literature [3], [110], [121].

3.3.2 Power law model

A system of two power laws describing the CO_2 methanation and reverse water gas shift was the starting point of the kinetic study (3-4) and (3-5).

$$r_{CO_2-meth} = k_{CO_2-meth}\, p_{CO_2}^{\alpha_{CO_2-meth}} p_{H_2}^{\beta_{CO_2-meth}} \left(1 - \frac{P_{CH_4}P_{H_2O}^2}{P_{CO_2}P_{H_2}^4 K_{eq,CO_2-meth}}\right) \quad (3\text{-}5)$$

$$r_{RWGS} = k_{RWGS}\, p_{CO_2}^{\alpha_{RWGS}} p_{H_2}^{\beta_{RWGS}} \left(1 - \frac{P_{CO}P_{H_2O}}{P_{CO_2}P_{H_2} K_{eq-RWGS}}\right) \quad (3\text{-}6)$$

The kinetic constants are expressed as Arrhenius type:

$$k_X = k_\infty \exp\left(-\frac{E_A}{RT}\right) \quad (3\text{-}7)$$

In order to reduce the correlation between preexponential factor and activation energy during the fitting procedure, equation (3-6) was reparametrized as follows:

$$k_X = k_{\infty,T_{ref}} \exp\left(\frac{E_A}{RT}\left(\frac{1}{T_{ref}} - \frac{1}{T}\right)\right) \quad (3\text{-}8)$$

The equilibrium constants were evaluated using thermodynamic data from the NIST Chemistry WebBook [122]. The constants are evaluated using equation (3-8).

$$K_X = \exp\left(-\frac{\Delta G_X(T,p_0)}{RT}\right) \quad (3\text{-}9)$$

The number of parameters that must be estimated for each power law equation are four: the preexponential factor and the activation energy in the Arrhenius term and the two orders of reaction for CO_2 and H_2.

The parity plot of the PL kinetics in Figure 3-16.a reveals a good fit for the methanation methane yield with an $\bar{R}^2$ of 0.984. The parameters of the power law kinetic model are reported in Table 3-7. The apparent activation energy of 86.2 kJ/mol is in line with literature values for nickel based catalysts [3], [110]. The negative exponent of the partial pressure of hydrogen in the RWGS reaction is reasonable because CO yield diminishes as the H_2 to CO_2 ratio in the feed increases.
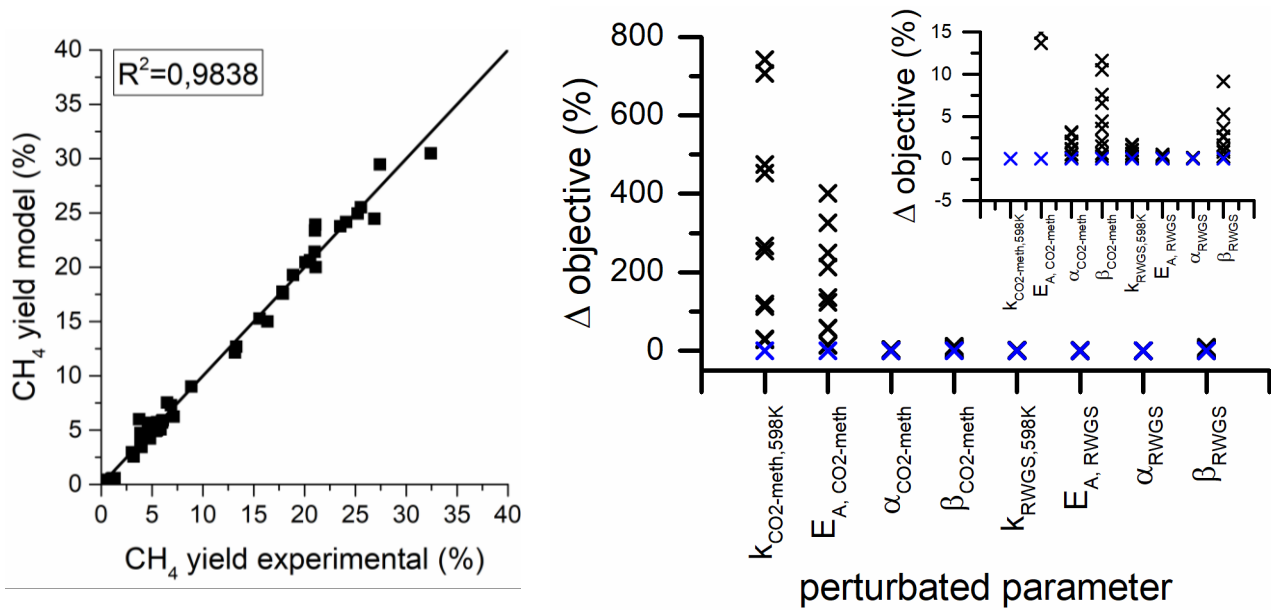
Figure 3-16: a) parity plot for the power law kinetic models and b)Parameter sensitivity analysis for PL kinetic model (blue symbols represents the 0% variation)

Table 3-7: Power law expressions regression results

Parameters	CO_2 methanation	RWGS
$k_{X,598K}$ $(mol\ bar^{\alpha_X + \beta_X} g_{cat}^{-1}\ s^{-1})$	$8.243 \cdot 10^{-5}$	$3.407 \cdot 10^{-5}$
$E_{A,X}$ $(kJ\ mol^{-1})$	86.2	64.2
α_X (-)	0.194	0.783
β_X (-)	0.083	−1.376

In Figure 3-16.b the sensitivity analysis carried out on the parameters of the power law model is represented. The objective function is the most sensitive to the preexponential factor and activation energy of CO_2 methanation. The variation of the exponents of H_2 partial pressure in both reaction rates has a variation of the objective function. While variation of the exponents of the CO_2 partial pressures have the smallest effect on the objective function in both CO_2 methanation and RWGS rates.

3.3.3 Langmuir-Hinshelwood-Hougen-Watson (LHHW) models

The LHHW models were derived from two mechanisms proposed in literature and summarized in Table 3-4. Both mechanisms have in common many elementary steps. The difference is in the steps that converts adsorbed CO. On one hand, in mechanism the adsorbed CO species are hydrogenated in step 4.a to form carbon-hydroxyl COH or formyl HCO intermediates. Afterwards, the oxygen gets removed from these intermediates in step 5.a and further hydrogenated to methane in step 6.a. On the other hand, in mechanism b the adsorbed CO is converted in adsorbed carbon in step 4.b and further hydrogenated to methane. Both these mechanisms were successfully used to formulate rate equations that described the CO_2 methanation [3], [110], [121].

Table 3-8: Reaction mechanism proposed in literature

Meccanismi a		Meccanism b	
1.a	$H_2 + 2* \rightleftharpoons 2H*$	1.b	$H_2 + 2* \rightleftharpoons 2H*$
2.a	$CO_2 + 2* \rightleftharpoons CO* + O*$	2.b	$CO_2 + 2* \rightleftharpoons CO* + O*$
3.a	$CO* \rightleftharpoons CO + *$	3.b	$CO* \rightleftharpoons CO + *$
4.a	$CO* + H* \rightleftharpoons CHO* + *$	4.b	$CO* + * \rightleftharpoons C* + O*$
5.a	$CHO* + * \rightleftharpoons CH* + O*$	5.b	$C* + H* \rightleftharpoons CH* + O*$
6.a	$CH* + 3H* \rightleftharpoons CH_4* + 3*$	6.b	$CH* + 3H* \rightleftharpoons CH_4* + 3*$
7.a	$CH_4* \rightleftharpoons CH_4 + *$	7.b	$CH_4* \rightleftharpoons CH_4 + *$
8.a	$O* + H* \rightleftharpoons OH* + *$	8.b	$O* + H* \rightleftharpoons OH* + *$
9.a	$OH* + H* \rightleftharpoons H_2O* + *$	9.b	$OH* + H* \rightleftharpoons H_2O* + *$
10.a	$H_2O* \rightleftharpoons H_2O + *$	10.b	$H_2O* \rightleftharpoons H_2O + *$

The general form of LHHW rate equations have the following form (3-9):

$$rate = \frac{k \cdot DF}{(AD)^n} \tag{3-10}$$

Where k is the kinetic term and depends on the rate determining step, DF is the driving force and represents the distance from the thermodynamic equilibrium, AD is the adsorption group that depends on the most abundant surface intermediates and the exponent n is an integer. The rate equations were derived using the same approach found in [123].

The derivation of the rate equation that resulted giving the best fit. Derivation of the CO_2 methane rate using mechanism 2 with rate determining step 4 and MASI $CO*$, $H*$ e H_2O*.

➤ The reaction rate of methane production will be equal to:

$$\frac{dCO_{2,meth}}{dt} = r_4 = k_4(CO*)(*) \tag{3-11}$$

➤ Step 1.a in quasi equilibrium:

$$k_1 P_{H_2}(*)^2 \cong k_{-1}(H*)^2 \Rightarrow (H*) = \sqrt{K_1 P_{H_2}}(*) \tag{3-12}$$

➤ Step 2.a in quasi equilibrium:

$$k_2 P_{CO_2}(*)^2 \cong k_{-2}(CO*)(O*) \Rightarrow (CO*) = \frac{K_2 P_{CO_2}(*)^2}{(O*)} \tag{3-13}$$

➤ Step 3.a in quasi equilibrium:

$$k_3(CO*) \cong k_{-3}P_{CO}(*) \Rightarrow (CO*) = \frac{1}{K_3}P_{CO}(*) \tag{3-14}$$

➤ Steady state approximation for O* species:

$$\frac{d(O *)}{dt} = 0 \cong r_2 + r4 - r10$$
$$= k_2 P_{CO_2}(*)^2 - k_{-2}(CO *)(O *) + k_4(CO *)(*) \qquad (3\text{-}15)$$
$$- k_{10}(O *)(H *) + k_{-10}(OH *)(*)$$

➤ CO production is low compared to CH_4 production → Reaction 3.a is shifted to the left → $r_2 \cong r_4$:

$$k_2 P_{CO_2}(*)^2 - k_{-2}(CO *)(O *) \cong k_4(CO *)(*) \qquad (3\text{-}16)$$

➤ Step 10.a:

$$r_{10} = k_{10}(O *)(H *) - k_{-10}(OH *)(*) \qquad (3\text{-}17)$$

➤ For the steady state approximation → $r_{10} = r_{11}$. Furthermore, it is assumed that the equilibrium of r_{11} is shifted to the right therefore this reaction can be treated as irreversible:

$$k_{10}(O *)(H *) - k_{-10}(OH *)(*) = k_{11}(OH *)(H *) \qquad (3\text{-}18)$$

➤ In Step 10.a the direct and reverse reactions are assumed to be large compared to the net rate → quasi equilibrium for Step 10.a:

$$k_{10}(O *)(H *) \cong k_{-10}(OH *)(*) \Rightarrow (OH *) = \frac{K_{10}(O *)(H *)}{(*)} \qquad (3\text{-}19)$$

➤ Equation (3-14) becomes:

$$0 = 2\, r_4 - r_{11} = 2k_4(CO *)(*) - k_{11}(OH *)(H *)$$
$$= 2k_4(CO *)(*) - \frac{K_{10}k_{11}(O *)(H *)^2}{(*)} \qquad (3\text{-}20)$$

➤ From equation (3-19) and (3-10) the expression for $(O *)$ is found:

$$(O *) = \frac{2k_4(CO *)(*)^2}{K_{10}k_{11}(H *)^2} = \frac{2k_4(CO *)}{K_1 K_{10}k_{11}P_{H_2}} \qquad (3\text{-}21)$$

Substituting equation (3-20) in (3-12) the concentration of CO can be evaluated:

$$(CO *) = \frac{K_1 K_2 K_{10}k_{11}P_{CO_2}P_{H_2}(*)^2}{2k_4(CO *)} \Rightarrow (CO *)$$
$$= \left(\frac{K_1 K_2 K_{10}k_{11}}{2k_4}\right)^{0.5} P_{CO_2}^{0.5}P_{H_2}^{0.5}(*) \qquad (3\text{-}22)$$

➤ Substituting the result of equation (3-21) in equation (3-20) $(O *)$ is obtained:

$$(O*) = \frac{2k_4}{K_1 K_{10} k_{11} P_{H_2}} \left(\frac{K_1 K_2 K_{10} k_{11}}{2k_4}\right)^{0.5} P_{CO_2}^{0.5} P_{H_2}^{0.5} (*)$$

$$= \left(\frac{2K_2 k_4}{K_1 K_{10} k_{11}}\right)^{0.5} \frac{P_{CO_2}^{0.5}}{P_{H_2}^{0.5}} (*) \tag{3-23}$$

➤ Balance of active sites considering the MASI:

$$(*)_{TOT} = (*) + (CO*) + (H*) + (H_2O*) \tag{3-24}$$

➤ Step 12.a in quasi equilibrium:

$$k_{12}(H_2O*) = k_{-12} P_{H_2O}(*) \Rightarrow (H_2O*) = \frac{1}{K_{12}} P_{H_2O}(*) \tag{3-25}$$

➤ The concentration of free active sites (*) is:

$$(*)_{TOT} = (*) + \left(\frac{K_1 K_2 K_{10} k_{11}}{2k_4}\right)^{0.5} P_{CO_2}^{0.5} P_{H_2}^{0.5}(*) + \frac{1}{K_3} P_{CO}(*)$$

$$+ \sqrt{(K_1 P_{H_2})}(*) + \frac{1}{K_{12}} P_{H_2O}(*) \tag{3-26}$$

$$(*) = \frac{(*)_{TOT}}{1 + \left(\frac{K_1 K_2 K_{10} k_{11}}{2k_4}\right)^{0.5} P_{CO_2}^{0.5} P_{H_2}^{0.5} + \frac{1}{K_3} P_{CO} + \sqrt{(K_1 P_{H_2})} + \frac{1}{K_{12}} P_{H_2O}} \tag{3-27}$$

➤ Substituting equation (3-21) and (3-26) in equation (3-10) we obtain:

$$R_{CO_2-meth}$$

$$= \frac{k_4 \left(\frac{K_1 K_2 K_{10} k_{11}}{2k_4}\right)^{0.5} P_{CO_2}^{0.5} P_{H_2}^{0.5} (*)_{TOT}}{\left(1 + \left(\frac{K_1 K_2 K_{10} k_{11}}{2k_4}\right)^{0.5} P_{CO_2}^{0.5} P_{H_2}^{0.5} + \frac{1}{K_3} P_{CO} + \sqrt{(K_1 P_{H_2})} + \frac{1}{K_{12}} P_{H_2O}\right)^2} \tag{3-28}$$

➤ Considering the thermodynamic equilibrium in equation (3-27) and renaming some groups the final expression is obtained:

$$R_{CO_2-meth} = \frac{k_{CO_2-meth} P_{CO_2}^{0.5} P_{H_2}^{0.5} \left(1 - \frac{P_{CH_4} P_{H_2O}^2}{P_{CO_2} P_{H_2}^4 K_{eq,CO_2-meth}}\right)}{\left(1 + \sqrt{K_{H_2} P_{H_2}} + K_{CO} P_{CO} + \sqrt{K_{MIX} P_{CO_2} P_{H_2}} + K_{H_2O} P_{H_2O}\right)^2} \tag{3-29}$$

Derivation of the RWGS rate using mechanism a with rate determining step 2.a (adsorption of CO₂) and MASI $CO*$, $H*$ e H_2O*.

➤ The reaction rate of methane production will be equal to:

$$\frac{dRWGS}{dt} = r_2 = k_2 P_{CO_2}(*)^2 \tag{3-30}$$

➤ Substituting equation (3-21) in (3-29):

$$r_{RWGS} = \frac{k_{RWGS}P_{CO_2}\left(1 - \dfrac{P_{CO}P_{H_2O}}{P_{CO_2}P_{H_2}K_{eq-RWGS}}\right)}{\left(1 + K_{H_2}P_{H_2}^{0.5} + K_{H_2O}P_{H_2O} + K_{CO}P_{CO} + K_{MIX}P_{CO_2}^{0.5}P_{H_2}^{0.5}\right)^2} \tag{3-31}$$

Summarizing:

$$R_{CO_2-meth} = \frac{k_{CO_2-meth}\,P_{CO_2}^{0.5}P_{H_2}^{0.5}\left(1 - \dfrac{P_{CH_4}P_{H_2O}^2}{P_{CO_2}P_{H_2}^4 K_{eq,CO_2-meth}}\right)}{\left(1 + K_{H_2}P_{H_2}^{0.5} + K_{CO}P_{CO} + K_{MIX}P_{CO_2}^{0.5}P_{H_2}^{0.5} + K_{H_2O}P_{H_2O}\right)^2} \tag{3-32}$$

$$r_{RWGS} = \frac{k_{RWGS}P_{CO_2}\left(1 - \dfrac{P_{CO}P_{H_2O}}{P_{CO_2}P_{H_2}K_{eq-RWGS}}\right)}{\left(1 + K_{H_2}P_{H_2}^{0.5} + K_{H_2O}P_{H_2O} + K_{CO}P_{CO} + K_{MIX}P_{CO_2}^{0.5}P_{H_2}^{0.5}\right)^2} \tag{3-33}$$

The LHHW kinetic rate that was chosen for fitting the kinetic data is represented in equations (3-34) and (3-35). These rates were determined assuming as rate determining step 4.a in the mechanism in Table 3-8 for the CO_2 methanation reaction and step 2.a for the RWGS reaction rate. Adsorbed hydrogen, CO and hydroxyls were considered as the most abundant surface intermediates. This kinetic model was readapted from a previous study with the addition of the RWGS reaction with a LHHW derived equation [3].

$$r_{CO_2-meth} = \frac{k_{CO_2-meth}\,P_{CO_2}^{0.5}P_{H_2}^{0.5}\left(1 - \dfrac{P_{CH_4}P_{H_2O}^2}{P_{CO_2}P_{H_2}^4 K_{eq,CO_2-meth}}\right)}{\left(1 + \sqrt{K_{H_2}P_{H_2}} + \sqrt{K_{MIX}P_{CO_2}P_{H_2}} + K_{OH}\dfrac{P_{H_2O}}{\sqrt{P_{H_2}}}\right)^2} \tag{3-34}$$

$$r_{RWGS} = \frac{k_{RWGS}P_{CO_2}\left(1 - \dfrac{P_{CO}P_{H_2O}}{P_{CO_2}P_{H_2}K_{eq-RWGS}}\right)}{\left(1 + \sqrt{K_{H_2}P_{H_2}} + \sqrt{K_{MIX}P_{CO_2}P_{H_2}} + K_{OH}\dfrac{P_{H_2O}}{\sqrt{P_{H_2}}}\right)^2} \tag{3-35}$$

The fitting parameters are reported in Table 3-9, the parity plot in and the sensitivity analysis is reported in Figure 3-17. A good agreement can be observed in Figure 3-18 between the LHHW model and the experimental CO_2 conversion and CH_4 yield.

Table 3-9: LHHW kinetic parameters

Parameter	Value
$k_{CO_2\text{-meth},598K}$ $\left(\text{mol g}_{cat}^{-1}\text{ bar}^{-1}\text{s}^{-1}\right)$	1.816
E_{A,CO_2meth} $\left(\text{kJ mol}^{-1}\right)$	99.0
$K_{H_2,598K}$ $\left(\text{bar}^{-1}\right)$	$2.373\cdot10^3$
$\Delta H_{H_2}\left(\text{kJ mol}^{-1}\right)$	17.5
$K_{OH,598K}$ $\left(\text{bar}^{-0.5}\right)$	$3.256\cdot10^2$
$\Delta H_{OH}\left(\text{kJ mol}^{-1}\right)$	6.9

$K_{MIX,598K}$ (bar^{-1})	$4.196 \cdot 10^3$
$\Delta H_{MIX}(kJ\ mol^{-1})$	-54.5
$k_{RWGS,598K}$ $(mol\ g_{cat}^{-1}\ s^{-1})$	0.2071
$E_{A,\ RWGS}$ $(kJ\ mol^{-1})$	71.8
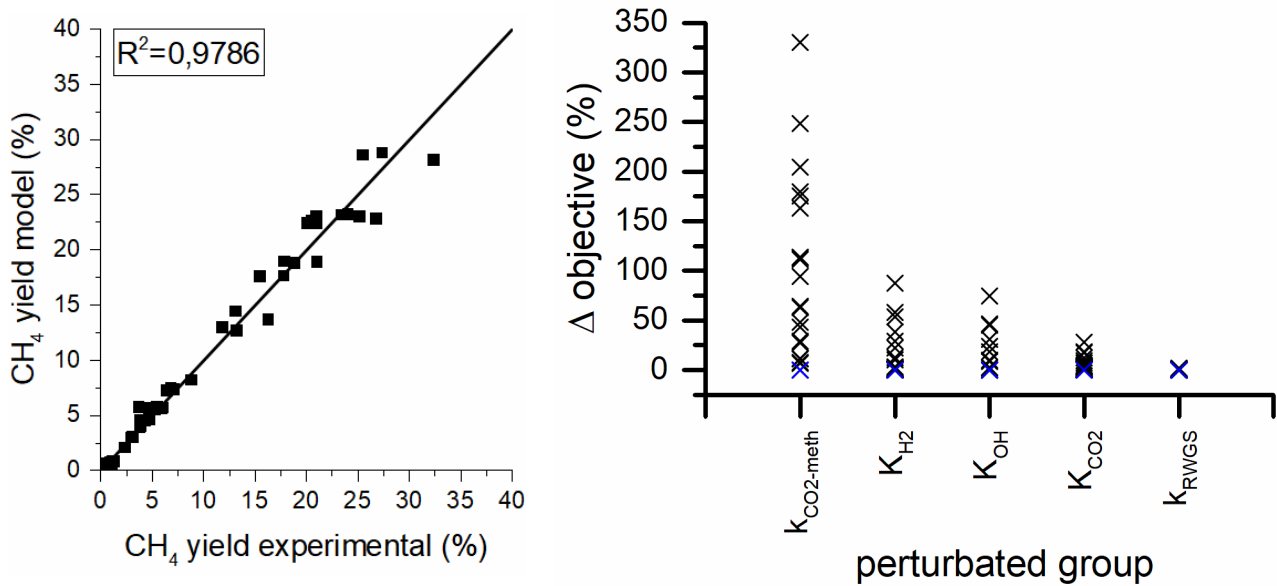
Figure 3-17: a) Parity plot for the power LHHW model and b) parameter sensitivity analysis (blue symbols represents 0% variation)
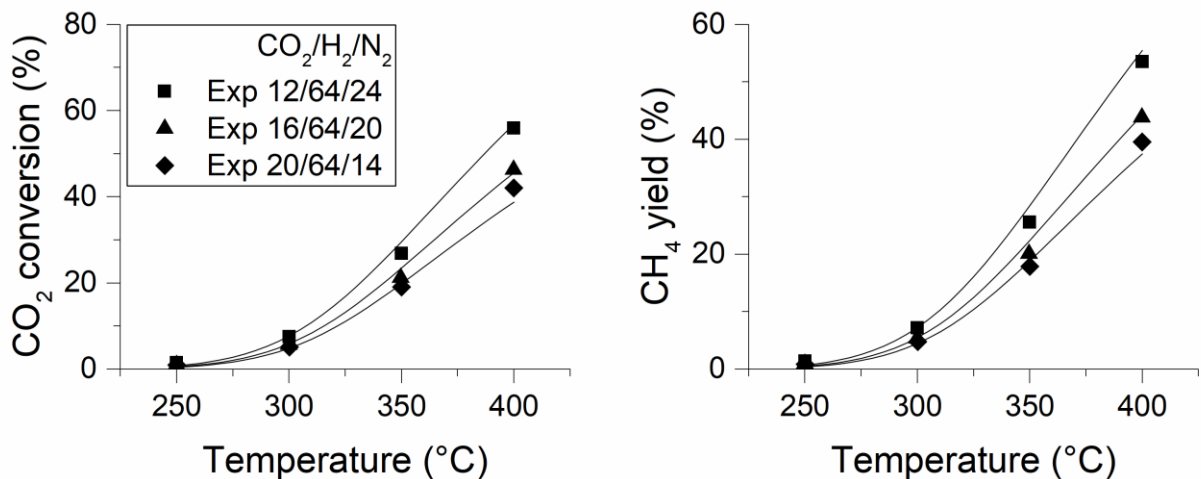
Figure 3-18: CO₂ partial pressure effect: experimental vs model (continuous curves)

3.4 Catalyst aging analysis

When performing the analysis of catalyst activity decay, we can divide the reactions in two categories: separable kinetics (3-36) and non-separable kinetics (3-37). In separable kinetics the aging contribution is separable from the rate

contribution. Variable separability allows to study the activity decay independently from the reaction kinetics [124].

$$r' = a(t, T, C) \cdot r'(T, C) \tag{3-36}$$

$$r' = r'(t, T, C) \tag{3-37}$$

Variable separability is assumed for the problem at hand. The activity of the catalyst can be defined as follows:

$$a = \frac{rate\ at\ time\ t}{rate\ of\ the\ fresh\ catalyst} = \frac{r(t)}{r_0} \tag{3-38}$$

Generally, the activity decay rates have a power law form. According to Levenspiel [125] there are four types of decay rates:

> Parallel decay rate when two reaction occur in parallel: A→R; A→P↓. In the first reaction our desired product is obtained while in the second reaction an undesired product that causes the deactivation is obtained.

$$\begin{cases} -r_A' = a k' C_A^n \\ -\dfrac{da}{dt} = k_d C_A^m a^d \end{cases} \tag{3-39}$$

> Series decay rate when two reactions occur in series: A→R→P↓. In this case the intermediate is our desired product. The undesired product is the deactivation agent and is generated from the desideria intermediate.

$$\begin{cases} -r_A' = a k' C_A^n \\ -\dfrac{da}{dt} = k_d C_R^m a^d \end{cases} \tag{3-40}$$

> Side-by-side decay rate when a poison is for exampled present in the feed stream: A→R; P→P↓.

$$\begin{cases} -r_A' = a k' C_A^n \\ -\dfrac{da}{dt} = k_d C_P^m a^d \end{cases} \tag{3-41}$$

> Concentration independent decay rate. In this case the decay rate only depends on the temperature.

$$\begin{cases} -r_A' = k' C_A^n a \\ -\dfrac{da}{dt} = k_d a^d \end{cases} \tag{3-42}$$

Where d is called the order of deactivation, m measures the concentration dependency and k_d is the decay constant. The decay constant is generally expressed as an Arrhenius term $k_d = k_{d,0} \exp(E_d/RT)$ with E_d the decay activation energy. In some cases, deactivation can be caused by both reactants and products.

In this case two activity runs were performed on a fresh catalyst sample and on the same sample aged at 425 °C for 100 h. The activity tests were performed at 5 bar with a feed composition $CO_2/H_2/N_2=16/64/20$ and in a temperature range between 250° and 350°C. The data were obtained under differential reactor conditions.

In an Arrhenius term the preexponential factor is proportional to the number of active sites while the activation energy depends on the reaction mechanism. Therefore, in an Arrhenius plot the eventual loss of active sites would result in a parallel translation of the curve while a change in the reaction mechanism would change the slope of the curve. Two simple first order kinetic model rate was used to interpolate the activity data: one for the fresh (3-43) and one for the aged sample (3-44).

$$r'_f = k'_{0,f} \exp(E_{a,f}/RT) C_{CO_2} \tag{3-43}$$
$$r'_a = k'_{0,a} \exp(E_{a,a}/RT) C_{CO_2} \tag{3-44}$$

The Arrhenius plot and the regression results are reported in Figure 3-19. Two parallel curves were obtained with basically the same activation energy (R^2 close to unity for both curves). This means that the reaction mechanism does not change, and the deactivation is caused by a loss of active sites.

	$k_\infty (m^3/h/g_{cat})$	$E_A (kJ/mol)$
Fresh	$1.4 \cdot 10^7$	87.1 ± 0.4
Aged	$9.3 \cdot 10^6$	87.3 ± 0.6
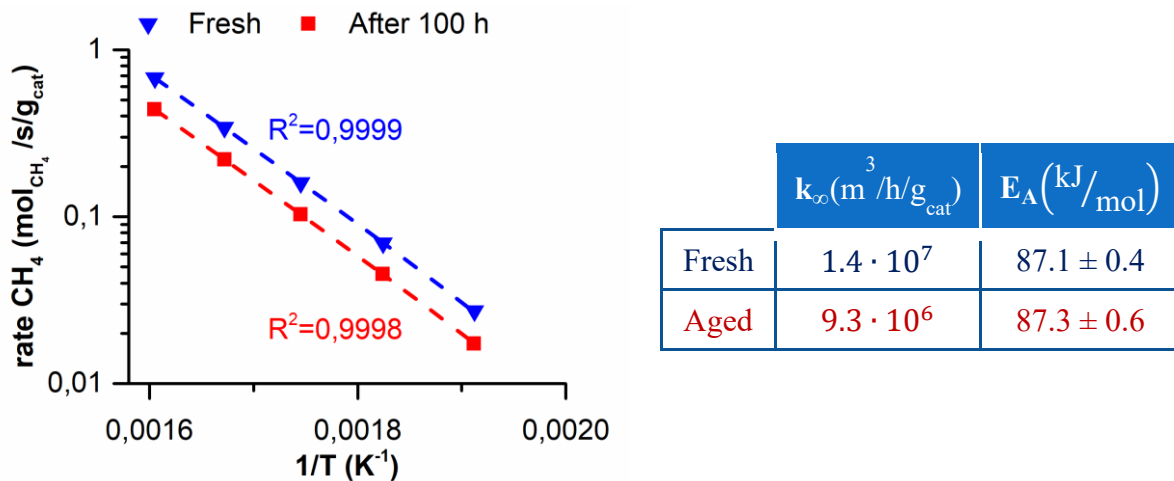
Figure 3-19: Arrhenius plot and regression results with two first order rate equations for the fresh and aged activity runs

The same procedure was then repeated with the exception that the regression was performed with the same activation energy represented by equations (3-45) and (3-46). This allowed to estimate all tree parameters in the same run ($k'_{0,f}$, $k'_{0,a}$ and E_a).

$$r'_f = k'_{0,f} \exp(E_a/RT) C_{CO_2} \tag{3-45}$$
$$r'_a = k'_{0,a} \exp(E_a/RT) C_{CO_2} \tag{3-46}$$

In Figure 3-20 the regression results are reported. Also, in this case the R^2 is basically equal to unity giving a perfect fit of the data. The activation energies in both cases are in line with literature values for Ni based catalysts 80-110 kJ/mol [110].
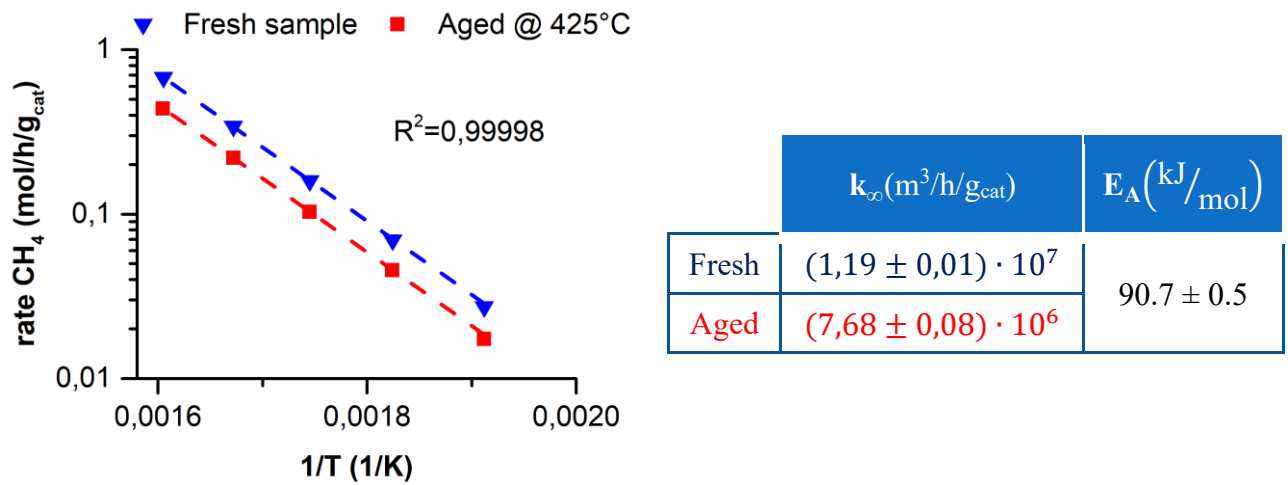
Figure 3-20: Arrhenius plot and regression results with two first order rate equations with the same activation energy for the fresh and aged activity runs

At this point the ratio of the two preexponential factors was compared to the ratio of the surface areas of fresh and aged samples:

$$\frac{k_a}{k_f} = \frac{7.68 \cdot 10^6}{1.19 \cdot 10^7} = 0.65 \tag{3-47}$$

$$\frac{BET_{aged@425°C}}{BET_{fresh\&reduced}} = \frac{144.3}{217.9} = 0.66 \tag{3-48}$$

The two ratios are basically identical. This means that the reduction of the active sites is directly proportional to the surface area reduction further supporting the thesis that total surface area loss is the main cause of aging. Furthermore, even if other deactivation phenomena occur (i.e. nickel particle sintering) the main one is by far the collapse of the support.

With this last result in mind the same analysis was carried out on the data obtained during the long-term tests. This time the data was obtained in a reactor operating in integral mode and therefore the procedure is slightly different. A first order kinetic rate that considers the distance from equilibrium was used (3-49). The regression was performed on the fresh sample and at the end of the run. Since the temperature varies during the test a mean temperature value was used for the equilibrium composition calculation. The results are reported in Table 3-10. The ratio between the fresh and aged kinetic constants was compared with the ratio of the surface areas. A very good agreement was obtained also in this case.

$$-r_{CO_2} = k_{cin}(T)\left(C_{CO_2} - C_{CO_2,eq}\right) \tag{3-49}$$

Subsequently, a first order deactivation rate was used to determine the characteristic time of deactivation (3-50).

$$-\frac{da}{dt} = k_d(T)\,a \xrightarrow{integral\ form} a = a_0 e^{-k_d t} = a_0 e^{-\frac{t}{\lambda}} \tag{3-50}$$

71

	$\dfrac{BET\ area(100h)}{BET\ area(0h)}$	$a(100h) = \dfrac{k_{cin,T}(100h)}{k_{cin,T}(0h)}$	$\lambda\ (h)$
Fresh reduced	1.00	1.00	-
100h @ 280°C	0.95	1.00	-
100h @ 380°C	0.76	0.76	459
100h @ 425°C	0.66	0.68	278
100h @ 500°C	0.52	0.52	183

Finally, an independent decay rate was used to model the deactivation rate (3-51).

$$-\frac{da}{dt} = k_{a,T_{ref}}\ exp\left(\frac{E_{A,a}}{R}\left(\frac{1}{T_{ref}} - \frac{1}{T}\right)\right) \cdot a^m \qquad (3\text{-}51)$$

The three parameters that the fitting procedure determines are the preexponential factor ($k_{a,T_{ref}}$), the activation energy ($E_{A,a}$) and the exponent m. The LHHW kinetic rate obtained in section 3.3.3 was used to describe the intrinsic kinetics. The catalyst aging rate was determined using the data from the aging tests carried out at 380°C, 425°C and 500°C. The only test that was excluded from the dataset was the run with 6% of methane in the feed because it was at equilibrium for half the test. The dataset was reduced by sampling the data with a sampling time step of 5h. The CO_2 conversion and temperature were averaged with ±30 minutes interval around the sampling point. This procedure reduced the number of points to a more manageable amount. In Table 3-11 the fitting parameters are reported and Figure 3-21 the corresponding parity plot.

Table 3-11: Aging kinetics parameters

Parameter	Value
$k_{a,673.15K}\left(h^{-1}\right)$	$9.6 \cdot 10^{-3}$
$E_{A,a}\left(kJ/mol\right)$	61.3
m	13.11
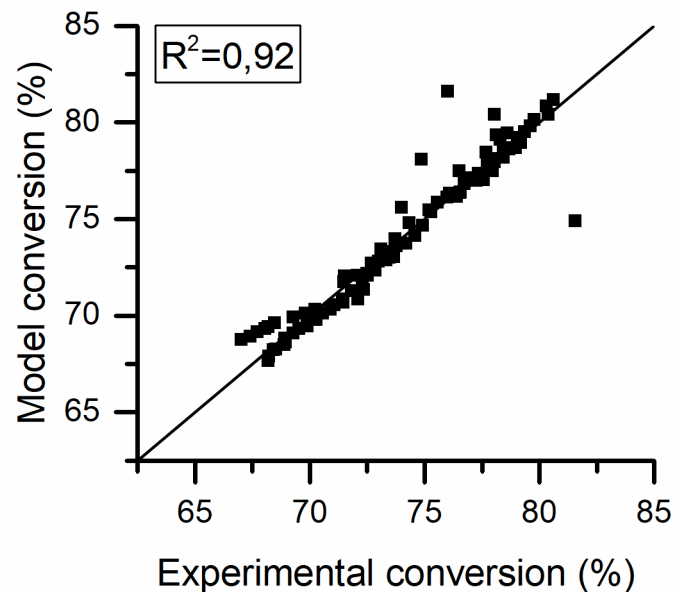
Figure 3-21: Parity plot for aging kinetics

According to literature the exponent m can assume values between 3 and 15 for supported Ni catalyst sintering rates [126], [127]. This is in line with the value that was found in this study. However, being the deactivation an empiric law, the fitting parameters do not have any physical meaning. Therefore, any consideration on the values assumed by the parameters can be misleading. The aging law that was obtained here can be used in a reactor model to give some insight on the possible behaviour of the reactor in time. This would allow the designer to put in place different strategies to slow the aging process, and/or by allowing higher flexibility on the operating conditions to limit the aging effect on the process performance (i.e. temperature and pressure).

Chapter 4

Reactor modelling

In this chapter the modelling of a multichannel methanation reactor designed to treat a 10 Nm^3/h of CO_2 and 40 Nm^3/h is carried out (the size of the plant simulated in Chapter 2). Firstly, the impact on the performance to different operating parameters and geometry has been investigated in order to improve the heat management and conversion rate of the design. Secondly the effect of catalyst aging was included in order to evaluate the effect on the reactors ability to maintain the conversion over time. The simulations were carried out using COMSOL Multiphysics simulation software.

This part was carried out within the collaboration with the French Commissariat à l'énergie atomique et aux énergies alternatives (CEA) in Grenoble.

4.1   General considerations

The level of mathematical detail that can be included in the analysis depends on the level of understanding of the physical and chemical processes that occur in a reactor. Furthermore, it also depends on the end use of the model and this generally is a balance between value and cost. Models may be used for analysing data, reactor scale-up, estimating steady state performance, dynamic behaviour of the reactor (i.e. simulating start-up and shutdown) and system control. A very elaborate model is justifiable when the operating conditions are particularly critical for the process performance, safety or to explore uncertainties not easily or cost-effectively investigated through experimentation.

One of the key aspects of modelling is to derive the appropriate momentum, mass and energy conservation equations that describe the reactor behaviour. The general form of the mass balance equation of the general species i con be summarized as follows:

$$\begin{bmatrix} species\ i \\ inlet\ flowrate \end{bmatrix} - \begin{bmatrix} species\ i \\ outlet\ flowrate \end{bmatrix} + \begin{bmatrix} generated \\ species\ i \\ per\ unit\ of\ time \end{bmatrix}$$
$$= \begin{bmatrix} accumulated \\ species\ i \\ per\ unit\ of\ time \end{bmatrix} \tag{4-1}$$

The general form of the energy balance equation con be summarized as follows:

$$\begin{bmatrix} energy\ introduced \\ per\ unit\ of\ time \end{bmatrix} - \begin{bmatrix} energy\ removed \\ per\ unit\ of\ time \end{bmatrix}$$
$$+ \begin{bmatrix} energy\ generated \\ per\ unit\ of\ time \end{bmatrix} = \begin{bmatrix} energy\ generated \\ per\ unit\ of\ time \end{bmatrix} \tag{4-2}$$

The resolution of the system of balance equations provide the outputs of the model.

4.1.1 Polytropic fixed bed reactor modelling

Highly exothermic reactions can be conducted in multitube cooled fixed bed reactors in order to intensify the heat removal. In this reactor design the tubes are filled with catalyst and are surrounded by the coolant (Figure 4-1).
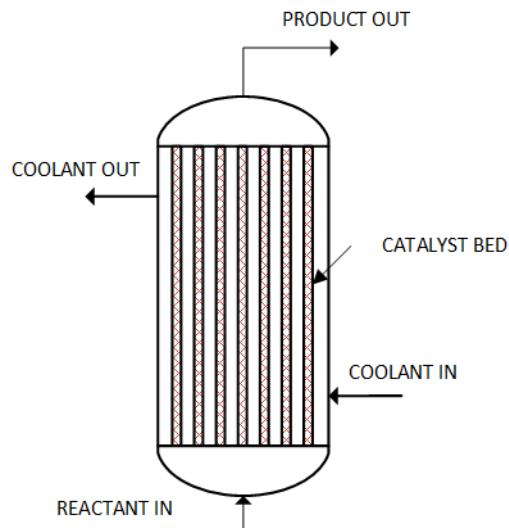
Figure 4-1: Multitube cooled fixed bed reactor

The design of a nonisothermal fixed bed reactor requires the simultaneous resolution of the mass and energy balance (Figure 4-2). If the reaction taking place is exothermic, the temperature profile inside the reactor will have a maximum. In case of an adiabatic reactor the maximum temperature will be reached at the outlet. If the reactor is cooled, then the maximum will generally be within the reactor. In this case the position of the maximum temperature is called the hot spot of the reactor. In some cases, the temperature of the hot spot could be extremely sensitive to the operating conditions (i.e. feed rate, feed temperature and coolant, pressure, etc).
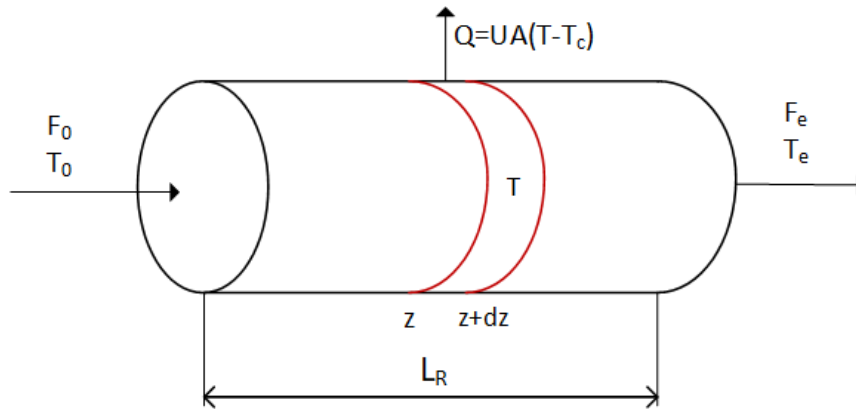
Figure 4-2: Tubular reactor/channel with wall heat exchange

The general steady state mass and heat balance for a tubular reactor is represented by equations (4-3) and (4-4).

$$\dot{m}\frac{dw_i}{dz} = v_{i,j}r_j\, S \tag{4-3}$$

$$\dot{m}C_p dT = r_j\Delta H_{r,j}\, dV + UA\,(T_c - T) \tag{4-4}$$

Where $\dot{m}$ is total mass flow rate, w_i is the mass fraction of component i, $v_{i,j}$ is the stoichiometric coefficient of component i in reaction j, r_j is the reaction rate and S is the reactor cross section. The heat generation term is $G(T) = r_j\Delta H_{r,j}\, dV$ and the heat rejection term is $R(T) = UA\,(T_c - T)$. In the next few paragraphs the considerations are made for a cooled CSTR, but similar considerations hold true also for PFR (a PFR can be simulated as CSTRs in series)[124].

The heat rejection term R(T) is equal to the product between the heat exchange coefficient, the heat exchange area and the temperature difference between coolant and reactor temperature. Therefore, the rejection term has linear characteristic with respect to the reactor temperature (Figure 4-3 left). The slope of the curve is determined by the product UA. An increase in the feed composition would result in a simple translation of the curve towards higher temperatures.

On the other hand, the generation term G(T) is directly related to the reaction rate. The reaction rate is exponentially dependent on the activation energy and reaction temperature. In Figure 4-3 (right) the dependency of the heat generation term on the temperature and activation energy is shown. A higher activation energy would lead to a steeper generation curve. Varying the operating parameters (i.e. space velocity, pressure, etc) could lead to a similar generation curve.
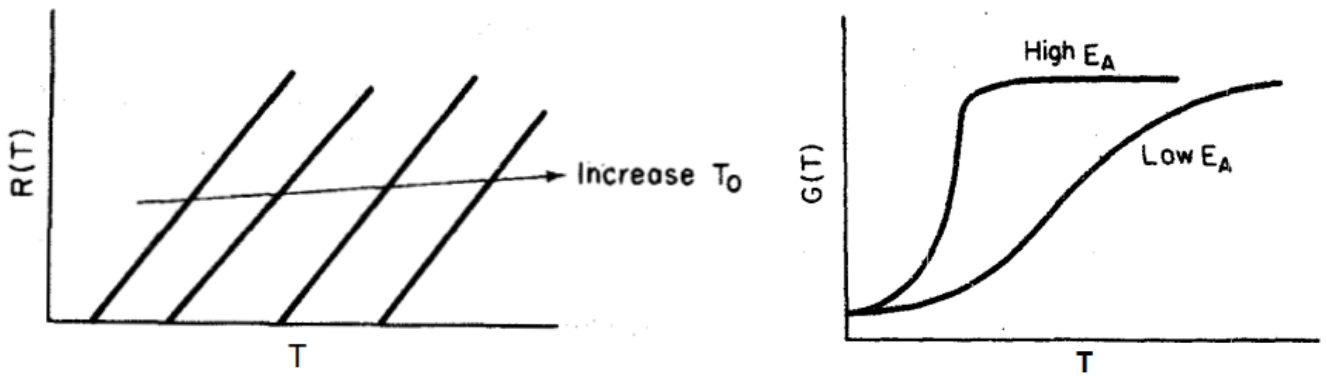
Figure 4-3: (left) Heat removal as a function reaction temperature and increasing feed/coolant temperature. (right) Heat generation as a function of reaction temperature.

The intersection point between the heat generation G(T) and the heat rejection R(T) curves determines the steady state operation condition. In certain operating conditions more than one intersection between the curves may occur giving rise to a multiple number of steady states. In Figure 4-4 the passage from single steady state to multiple steady states is shown by increasing the operating temperature. It can be observed that if the reactor starts operating at temperature T_a the operating point would be 1. As the temperature is increased to T_b the possible steady states become 2 (intersection 2 and 3) and to T_c they become 3 (intersection 4, 5 and 6 with 5 instable). The steady state at which the reactor operates from T_a to T_e would be 1, 2, 4, 7 and 10. When the reactor temperature surpasses T_e the possible steady state becomes again only one. This would lead to a jump in the reactor hot spot temperature. If the procedure is performed backwords the behaviour would similar only this time the succession of steady states would be 12, 11, 9, 6 and 3. The jump would take place at coolant temperature lower than T_b.
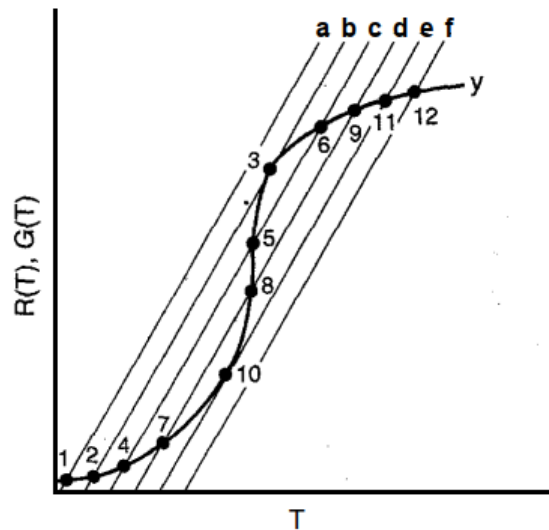
Figure 4-4: Multiple steady states by varying the feed temperature

This generate a hysteresis in the operating conditions and an area of temperatures where the reactor cannot operate. Furthermore, a slight oscillation in the operating conditions near the transition between one steady state to another could lead to a jump in the operating condition. The control of the system in these

conditions is basically impossible to perform. The hysteresis generated is also called ignition-extinction temperature curves Figure 4-5.
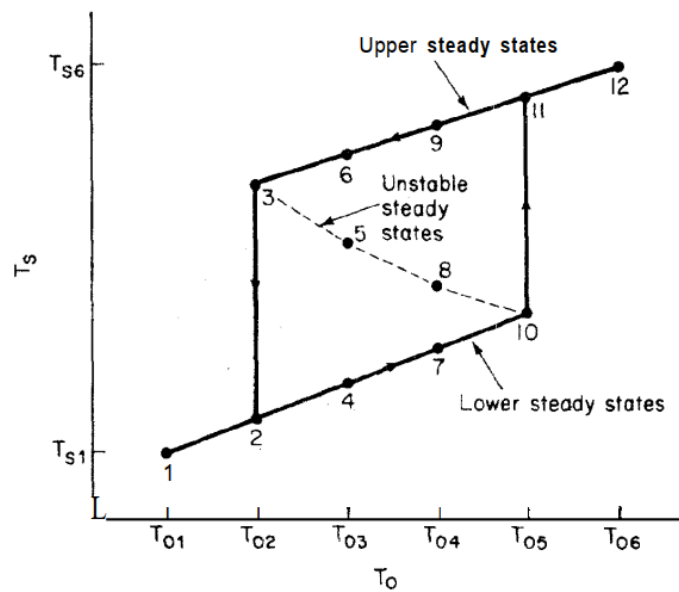
Figure 4-5: Steady state temperature versus feed temperature hysteresis (ignition-extinction temperature curves)

In Figure 4-6 the parameter sensitivity of a fixed bed CO_2 methanation reactor was investigated[128]. In this example the axial temperature profile was evaluated for small increments of the coolant temperature (T_c). At T_c=279°C a modest hot spot temperature increases of 11°C is obtained. In case T_c is increased to 282°C the peak temperature at the centre of the reactor becomes more pronounced with an increase of 30°C. With another increase of T_c to 285°C a huge jump in the peak temperature is obtained with a maximum of 690°C. The hot spot is localized towards the inlet of the reactor where basically the reactants are fully converted. The rest of the bed does not have reactants and the temperature drops to T_c.
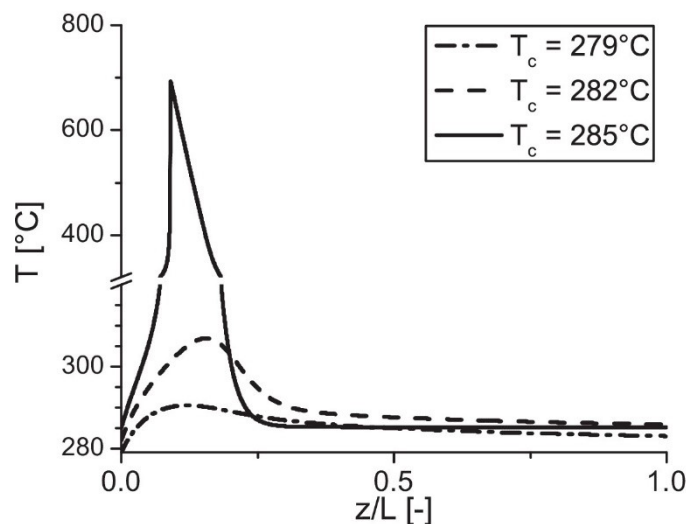
Figure 4-6: Parameter sensitivity of a CO_2 methanation reactor [128]

The reactor is very sensible to the inlet/coolant temperature between 282 and 285°C where the ignition point is occurring (also called runaway zone in case the

79

peak temperature is dangerous or undesirable). As for the CSTR case present earlier this zone is characterized by an abrupt transition of the hot spot temperature to extremely high temperature as in this case.

4.2 Model formulation

4.2.1 Mass balance

Reactor level mass balance

At the reactor scale the mass balance was represented through equation (4-5):

$$\frac{\partial(\rho_f \omega_i)}{\partial t} + \nabla \cdot (\rho_f \omega_i \mathbf{u}) = -\nabla \cdot \mathbf{j}_i + s_i \tag{4-5}$$

Where ρ_f is the density of the fluid, **u** is the velocity vector, ω_i, **j**$_i$ and s_i are, respectively, the mass fraction, the dispersive flux and source term of component i. The boundary conditions for the mass balance equations are the following:

$$z = 0, \forall t: \qquad\qquad -\mathbf{n} \cdot (\mathbf{j}_i + \rho_f \omega_i \mathbf{u}) = \frac{\dot{m}_{0,i}}{A_c} \tag{4-6}$$

$$z = L_R, \forall t: \qquad\qquad -\mathbf{n} \cdot \mathbf{j}_i = 0 \tag{4-7}$$

Where L_R is the reactor length, **n** is the unitary vector perpendicular to the surface, $\dot{m}_{0,i}$ is the mass flow rate of component i at the reactor inlet and A_c is the cross-section area of the reactor.

The mass dispersion flux **j**$_i$ was expressed using Fick's law:

$$\mathbf{j}_i = \rho_f \mathbf{D}_{d,i} \cdot \nabla \omega_i \tag{4-8}$$

Where **D**$_{d,i}$ is the dispersion tensor taking into account anisotropic behaviour of dispersion.

The molar dispersion tensor for an axisymmetric problem has two components:

$$\mathbf{D}_{d,i}^* = \begin{pmatrix} D_{d,i,ax}^* & 0 \\ 0 & D_{d,i,rad}^* \end{pmatrix} \tag{4-9}$$

These two components can be expressed as empirical functions of two particle Peclet numbers:

$$\frac{\varepsilon_b}{Pe_{m,(axial\ or\ radial)}} = \frac{\gamma_1 \varepsilon_b}{Pe_m} + \gamma_2 \tag{4-10}$$

Where γ_1 and γ_2 are two empirical constants and the two Peclet numbers are defined as follows:

$$Pe_{m,(axial\ or\ radial)} = \frac{d_p u}{D_{d,(ax\ or\ rad),i}^*} \tag{4-11}$$

$$Pe_m = \frac{d_p u}{D_{m,i}^*} \tag{4-12}$$

A comparison of a few correlations for axial dispersion was presented by Delgado et al. and is reported in Figure 4-7. These correlations were obtained on spherical particle beds with diameter ranging between 0.5 and 5 mm. The aspect ratio of the bed (ratio of the diameter of the tube and particle) was higher than 12.

In can be observed that for $Pe_m \leq 1$ all the compared correlations are equivalent. At higher Peclet numbers the authors proposed correlations in the form of equation (4-9).
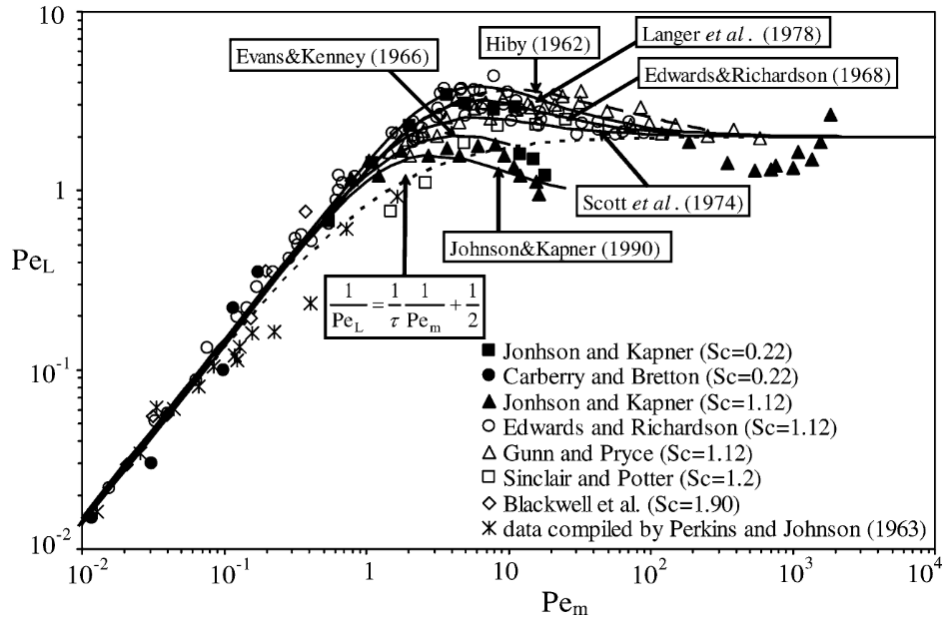
For this model the radial mass dispersion coefficient was calculated using Gunn's correlation [130] while the axial dispersion was calculated using Edward and Richardson's correlation [131]:

$$\frac{D_{i,rad}^*}{D_{i,m}^*} = \frac{\varepsilon_b}{1.91} + \frac{Re_p Sc}{11 - 4\exp\left(-\frac{7}{Re_p}\right)} \tag{4-13}$$

$$\frac{D_{i,ax}^*}{D_{i,m}^*} = 0.73\varepsilon_b + 0.5\left(1 + \frac{9.49\varepsilon_b}{Re_p Sc}\right) Re_p Sc \tag{4-14}$$

The dispersion tensor obtained with the previous correlations is expressed in terms of molar basis. The mass transport of species as formulated (4-5) requires the dispersion coefficients to be on mass basis. For a binary mixture the dispersion matrix would have been identical. This is not true for a mixture of more than two component. In order to convert from molar to mass basis the average mixture approximation was used. The mixture with this approximation is viewed as binary mix between the component of interest and a pseudo component with the average proprieties of the mixture. The mass dispersive flux can thus be written as follows:

$$j_i = \frac{\overline{MM}}{MM_i} j_i^* = \frac{1 - \omega_i}{1 - x_i} j_i^* \tag{4-15}$$

The source term in equation (4-5) was expressed as follows:

$$s_i = k_{i,s}\left(C_{i,s}^S - C_{i,f}^B\right) \cdot a_s(1 - \varepsilon_b) \cdot M_i \tag{4-16}$$

Where $k_{i,s}$ is the mass exchange coefficient, $C_{i,s}^S$ is the concentration of component i on the surface of the solid, $C_{i,f}^B$ is the concentration of component i in

the bulk of the fluid, a_s is the specific surface area of the catalyst, ε_b is the porosity of the fixed bed and M_i is the molar mass of component i. The mass transfer coefficient is generally expressed using empirical correlation expressed in function of particle Sherwood, Reynolds and Schmidt numbers of the following form:

$$Sh_p = \frac{k_{i,s}d_p}{D_i} = a\,Re_p^m\,Sc_p^n \tag{4-17}$$

Where the constants a, m and n can be found in literature [131], [132]. For this study the mass transfer coefficient was estimated using Satterfield's correlation[133]:

$$k_{i,s} = \frac{0.36}{1-\varepsilon_b}Sc^{-0.67}Re_p^{-0.36}u \tag{4-18}$$

Catalyst level mass balance

The pellet level mass balance was represented with the following equation:

$$\frac{\partial C_{i,s}}{\partial t} + \frac{1}{r^2}\frac{\partial}{\partial r}\left(-r^2 \mathcal{D}_{e,i}\frac{\partial C_{i,s}}{\partial r}\right) = \rho_s \sum_j a \cdot v_{i,j} r_j \tag{4-19}$$

Where $C_{i,s}$ is the molar concentration of component i inside the solid, $\mathcal{D}_{e,i}$ is the equivalent diffusion coefficient, ρ_s is the apparent density of the solid, a is the normalized activity, $v_{i,j}$ is the stoichiometric coefficient of component i in reaction j and r_j is the j reaction rate. The diffusivity inside the pellet can be calculated using the diffusivity of the component in the fluid media corrected with the pellet's porosity (not the whole particle is empty) and tortuosity (the channels are not straight) as follows:

$$\mathcal{D}_{e,i} = \mathcal{D}_i \frac{\varepsilon_p}{\tau_p} \tag{4-20}$$

Where $\mathcal{D}_e$ the equivalent diffusivity, $\mathcal{D}_i$ the diffusivity coefficient of component i, ε_p the pellet porosity and τ_p the pellet pore tortuosity.

The intrinsic kinetic model adopted here is based on the kinetic model of Xu and Froment [134]. The model considers 3 reactions (CO_2 methanation, reverse water gas shift and CO methanation) based on a LHHW kinetic approach. The reactions can be summarized as follows:

$$r_{CO_2-meth} = -k_{CO_2-meth}\left(P_{CH_4}P_{H_2O}^2 - \frac{P_{CO_2}P_{H_2}^4}{K_{eq,CO_2-meth}}\right)\cdot\frac{1}{den^2} \tag{4-21}$$

$$r_{RWGS} = -k_{RWGS}\left(P_{CO}P_{H_2O} - \frac{P_{CO_2}P_{H_2}}{K_{eq,RWGS}}\right)\cdot\frac{1}{den^2} \tag{4-22}$$

$$r_{CO-meth} = -k_{CO-meth}\left(P_{CH_4}P_{H_2O} - \frac{P_{CO}P_{H_2}^3}{K_{eq,CO-meth)}}\right)\cdot\frac{1}{den^2} \tag{4-23}$$

$$den = 1 + K_{CO}P_{CO} + K_{H_2}P_{H_2} + K_{CH_4}P_{CH_4} + K_{H_2O}\frac{P_{H_2O}}{P_{H_2}} \tag{4-24}$$

The parameters were readapted by Ducamp and are summarized in Table 4-1.

Parameters	Value
$k_{CO_2\text{-meth},0}$ $(\text{mol kg}_{cat}^{-1}\,\text{bar}^{0.5}\text{s}^{-1})$	$1.28 \cdot 10^{13}$
$E_{A,CO_2\text{meth}}$ (kJ mol^{-1})	209.9
$k_{RWGS,0}$ $(\text{mol kg}_{cat}^{-1}\,\text{s}^{-1})$	3.11
$E_{A,\,RWGS}$ (kJ mol^{-1})	59.4
$k_{CO\text{-}meth,0}$ $(\text{mol kg}_{cat}^{-1}\,\text{s}^{-1})$	$5.78 \cdot 10^{13}$
$E_{A,\,CO\text{-meth}}$ (kJ mol^{-1})	218.9
$K_{CO,0}$ (bar^{-1})	$8.23 \cdot 10^{-5}$
$\Delta H_{CO}(\text{kJ mol}^{-1})$	-70.65
$K_{H_2,0}$ (bar^{-1})	$6.12 \cdot 10^{-9}$
$\Delta H_{H_2}(\text{kJ mol}^{-1})$	-82.9
$K_{CH_4,0}$ (bar^{-1})	$6.65 \cdot 10^{-4}$
$\Delta H_{CH_4}(\text{kJ mol}^{-1})$	-38.28
$K_{H_2O,0}$ $(-)$	$1.77 \cdot 10^{5}$
$\Delta H_{H_2O}(\text{kJ mol}^{-1})$	$-88,68$

4.2.2 Energy balance

Reactor level energy balance

The heat balance at the reactor level is represented throw the following equation:

$$\rho_f Cp_f \frac{\partial T_f}{\partial t} + \rho_f Cp_f \boldsymbol{u}\nabla T_f = \nabla(\boldsymbol{\lambda_{eq}}\nabla T_f) + \dot{Q} \tag{4-25}$$

Where Cp_f is the heat capacity at constant pressure of the fluid, T_f is the fluid temperature, $\boldsymbol{\lambda_{eq}}$ is the equivalent heat conductivity tensor and Q is the heat source term. The boundary conditions for the heat balance equations are the following:

$$z = 0, \forall r, \forall t: \qquad -\boldsymbol{n} \cdot (\boldsymbol{\lambda_{eq}}\nabla T_f) = \rho\Delta H\,\boldsymbol{u} \cdot \boldsymbol{n} \tag{4-26}$$

$$z = L_R, \forall r, \forall t: \qquad -\boldsymbol{n} \cdot (\boldsymbol{\lambda_{eq}}\nabla T_f) = 0 \tag{4-27}$$

$$r = d_t/2, \forall z, \forall t: \qquad -\boldsymbol{n} \cdot (\boldsymbol{\lambda_{eq}}\nabla T_f) = U_W(T_{coolant} - T_{bed}) \tag{4-28}$$

Where $\Delta H = \int_{T_{upstream}}^{T_{bed}} C_p\,dT$ takes into account the difference in temperature of the fresh fluid entering the bed and the bed in order to avoid a discontinuity in temperature across the boundary.

For a 2-D axisymmetric geometry the heat dispersion tensor is a 2 by 2 matrix of the following form:

$$\boldsymbol{\lambda_{eq}} = \begin{pmatrix} \lambda_{eq,ax} & 0 \\ 0 & \lambda_{eq,rad} \end{pmatrix} \tag{4-29}$$

The elements of the equivalent heat conductivity tensor can be viewed as the sum of two contributions:

$$\lambda_{eq,ax/rad} = \lambda_{eq,0} + \lambda_{D,ax/rad} \tag{4-30}$$

Where $\lambda_{eq,0}$ is the conductivity of the bed without fluid flow and λ_D is the contribute of the moving fluid. The stagnant fluid contribution is isotropic and

depends on the structure of the bed, the conductivity of the solid (λ_s) and of the fluid (λ_f). The conductivity is made of two contributions: the first is the so-called parallel conductivity ($\lambda_{\text{parallel}}$) where heat is transferred through the contact points between the solid particles and by the fluid; the second is the so-called series conductivity (λ_{series}) where heat is transferred between phases from solid to gas and from gas to solid [135].

$$\lambda_{parallel} = (1 - \varepsilon_b)\lambda_s + \varepsilon_b \lambda_f \tag{4-31}$$

$$\lambda_{series} = \frac{1}{\frac{1 - \varepsilon_b}{\lambda_s} + \frac{\varepsilon_b}{\lambda_f}} \tag{4-32}$$

A comparison of different correlations to find the stagnant conductivity can be found in literature [136]. In this study the equation proposed by Krupiczka [137] was used to estimate the stagnant heat conductivity:

$$\frac{\lambda_{eq,0}}{\lambda_f} = \left(\frac{\lambda_s}{\lambda_f}\right)^n \tag{4-33}$$

$$n = 0.28 - 0.757 \log(\varepsilon_b) - 0.057 \log\left(\frac{\lambda_s}{\lambda_f}\right) \tag{4-34}$$

The radial heat dispersion component in λ_{eq} was estimated using the correlation proposed by Bey and Eigenberger [138], [139]:

$$\frac{\lambda_{eq,rad}}{\lambda_f} = \frac{\lambda_{eq,0}}{\lambda_f} + 0.1 Re_p Pr \tag{4-35}$$

The inner wall heat transfer coefficient can be estimated using correlations expressed in function of particle Nusselt, Reynolds and Prandtl numbers of the following form:

$$Nu_w = \frac{h_w d_p}{\lambda_f} = Nu_{w0} + b\, Re_p^m\, Pr^n \tag{4-36}$$

Where Nu_{w0} is the stagnant contribution to the heat transfer coefficient. Different correlations for the stagnant term can be found in literature[128], [139], [140]. In this study the correlation proposed by Bey and Eigenberger[139]:

$$Nu_w = 2.4 \frac{\lambda_{eq,0}}{\lambda_f} + 0.054\left(1 - \frac{d_p}{d_t}\right) Re_p Pr^{1/3} \tag{4-37}$$

The reactor was supposed to be cooled by boiling water with an external heat transfer h_c=10000 W/m²/K[141]. The overall heat transfer coefficient was calculated using equation (4-19).

$$U_{\text{wall}} \cong \left(\frac{1}{h_w} + \frac{1}{h_c}\right)^{-1} \tag{4-38}$$

The heat source term in equation (4-25) was expressed as follows:

$$Q = h_p(T^S - T^B) \cdot a_s(1 - \varepsilon_b) \tag{4-39}$$

Similar to the mass transfer coefficient the correlations are found for the heat transfer coefficient between the catalyst pellet and the fluid phase as function of particle Nusselt or Stanton, Reynolds and Prandtl numbers:

$$Nu_p = \frac{h_p d_p}{\lambda_s} = a\, Re_p^k\, Pr^l \tag{4-40}$$

$$St = \frac{Nu}{Re\, Pr} = \frac{h_p}{\rho_f\, u_f\, C_{p,f}} = b\, Re_p^m\, Pr^n \tag{4-41}$$

Different correlations can be found in literature [131], [132]. In this study the heat transfer was evaluated using Satterfield's correlation[133]:

$$h_p = \frac{0.43}{1 - \varepsilon_b} Pr^{-0.67} Re_p^{-0.36} \left(Cp_f \rho_f u\right) \tag{4-42}$$

Catalyst level energy balance

The pellet level heat balance was expressed using equation (4-20).

$$\rho_s Cp_s \frac{\partial T_s}{\partial t} + \nabla\left(-\lambda_{eq} \nabla T_s\right) = \rho_s \sum_j a \cdot r_j \Delta H_{r,j} \tag{4-43}$$

Where Cp_s is the heat capacity, T_s is the temperature, λ_{eq} is the equivalent heat conductivity of the solid and $\Delta H_{r,j}$ is the reaction heat of reaction j.

4.2.3 Momentum balance

The momentum balance was evaluated using Darcy's equation with Forchheimer's and Brinkmann's extensions (4-23). At the same time the continuity equation was solved together with the momentum balance (4-24).

$$\frac{\rho_g}{\varepsilon_b} \left(\frac{\partial u}{\partial t} + (u \cdot \nabla) \frac{u}{\varepsilon_b}\right) = -\nabla \cdot (PI + K) - \left(\frac{\mu}{\kappa} + \rho_g \beta_F |u|\right) u + F \tag{4-44}$$

$$\frac{\partial}{\partial t} \left(\varepsilon_b \rho_g\right) + \nabla \cdot \left(\rho_g u\right) = 0 \tag{4-45}$$

Where P is the pressure, μ is the gas viscosity, κ is the permeability of the bed, **K** is the viscous stress tensor, β_F is the Forchheimer drag factor and **F** is the force term. The viscous stress tensor was expressed with the generalized Newton's viscous law:

$$K = \frac{\mu}{\varepsilon_{bed}} ((\nabla u + (\nabla u)^T) - \frac{2}{3} (\nabla \cdot u)I) \tag{4-46}$$

The permeability of the bed and the Forchheimer drag factor were taken from Ergun's equation:

$$\kappa = \frac{d_p^2}{150} \frac{\varepsilon_b^3}{(1 - \varepsilon_b)^2} \tag{4-47}$$

$$\beta_F = \frac{1{,}75\rho_G}{d_p} \frac{1 - \varepsilon_b}{\varepsilon_b^3} \tag{4-48}$$

4.3 Transport proprieties

4.3.1 Thermodynamic proprieties

The pure component heat capacity at constant pressure, enthalpy difference and entropy were calculated using Shomates's equations:

$$C_p^0(T) = A + B\,t + C\,t^2 + D\,t^3 + \frac{E}{t^2} \tag{4-49}$$

$$\Delta H^0(T) = H^0(T) - H^0(298.15K)$$
$$= A\,t + B\frac{t^2}{2} + C\frac{t^3}{3} + D\frac{t^4}{4} - \frac{E}{t} + F - H \tag{4-50}$$

$$S^0(T) = A \ln(t) + B\,t + C\frac{t^2}{2} + D\frac{t^3}{3} - \frac{E}{2\,t^2} + G \tag{4-51}$$

Where $t = T/1000$. The coefficients from A to H of Shomate's equations were obtained from the National Institute of Standards and Technology (NIST) Chemistry WebBook [142]. The gas mixture heat capacity at constant pressure was calculated by weeing the pure component heat capacity with the mass fractions (4-31).

$$C_{p,mix}^0(T) = \sum_1^{nc} w_i C_{p,i}^0(T) \tag{4-52}$$

The equilibrium constants K_p for the ideal gas were calculated by using the following expression:

$$K_p(T) = \prod_i \left(\frac{P_{i,eq}}{P^0}\right)^{v_i} = \exp\left(-\frac{\Delta G^0(T)}{RT}\right), P^0 \equiv 1\ bar \tag{4-53}$$

Where ΔG^0 was calculated as follows:

$$\Delta G^0(T) = \sum_i v_i \left(\Delta H_i^0(T) + \Delta H_{f,i}^0 - T\,S_i^0(T)\right) \tag{4-54}$$

The gas mixture was considered ideal therefore for all other proprieties the ideal gas law was used.

4.3.2 Gas mixture diffusivity

If the fluid is a liquid, then the diffusivity to consider is the molecular diffusion (or regular diffusion).

If the fluid is a gas, then two cases can occur depending on the mean free path of the molecules and the diameter of the pores. The mean free path is given from the kinetic theory of gases:

$$l = \frac{RT}{\pi\sqrt{2}p\mathcal{N}_{Av}\sigma^2} \tag{4-55}$$

where R the gas constant, T the temperature, p the pressure, $\mathcal{N}_{Av}$ Avogadro's number, σ the mean diameter of the molecule. We can define the Knudsen number as the ration of the mean free path and the mean pore diameter of the catalyst ($Kn = l/d_p$). Three cases can be distinguished:

➢ Kn<0.1 represent regular diffusion regime
➢ 0.1<Kn<10 transient between regular and Knudsen diffusion regimes
➢ Kn>10 Knudsen diffusion regime

The Knudsen diffusion coefficient can be calculated as follows:

$$D_{K,i} = \frac{1}{3} d_p \sqrt{\frac{8RT}{\pi MM_i}} \underset{in\ SI}{=} 1.534\, d_p \sqrt{\frac{T}{MM_i}} \tag{4-56}$$

Where d_p the pore diameter, R the gas constant and MM_i the molar mass.

Most probably we are in the transition regime between regular and Knudsen diffusion. Therefore, the diffusivity should be calculated using a relationship combining the regular and Knudsen. One of the simplest relationships for this task is the Bosanquet equation:

$$\frac{1}{D} = \frac{1}{D_K} + \frac{1}{D} \tag{4-57}$$

The regular binary diffusivity was calculated using Fullers expression[143]:

$$D_{AB} = \frac{0.00143\ T^{1.75}}{P\ M_{AB}^{0.5}\left((\Sigma_v)_A^{1/3} + (\Sigma_v)_B^{1/3}\right)^2} \tag{4-58}$$

Where:

T = temperature in K

P = pressure in bar

M_A, M_B = the molecular mass of the two components in g/mol

M_{AB} = 2 $(1/M_A + 1/M_B)^{-1}$

Σ_v = is the sum of the atomic diffusion volumes that can be found tabulated

The mixture diffusion coefficient has been calculated using Fairbanks and Wilke correlation[144]:

$$D_{i,m} = \frac{1 - y_i}{\sum_{j \neq i}^{nc} \frac{y_j}{D_{ij}}} \tag{4-59}$$

4.3.3 Viscosity

For pressures below 10 bar the first order Chapman-Enskog equation (4-36) is used to determine the viscosity of pure components.

$$\mu_i = 26.69\frac{(MM_i\ T)^{0.5}}{\sigma^2\Omega_v} \tag{4-60}$$

Where μ_i is the viscosity (µP), MM_i the molecular mass (g/mol), T the temperature (K), σ the hard-sphere diameter (Å) and Ω_v is the collision integral. The collision integral is a function of the dimensionless temperature which depends on the chosen potential $\psi(r)$. It can be calculated using the dimensionless temperature defined as follows:

$$T^* = \frac{kT}{\varepsilon} \tag{4-61}$$

Where k is Boltzmann's constant, T the temperature and ε is the minimum of the pair-potential energy. The Lennard-Jones potential has most often been applied for the ideal gas viscosity calculation. The collision integral using this potential is calculated with equation (4-38).

$$\Omega_v = A(T^*)^{-B} + C\exp(-D\ T^*) + E\exp(-F\ T^*) \tag{4-62}$$

Where T^* is the dimensionless temperature, A=1.16145, B=0.14874, C=0.52487, D=0.77320, E=2.16178 and F=2.43787. This equation is valid for 0.3≤T^*≤100. The values of k/ε and σ are found tabulated.

The mixture viscosity was calculated using Wilke's method with Herning and Zipperer Approximation of ϕ_{ij}:

$$\mu = \sum_{i=1}^{n} \frac{y_i\mu_i}{\sum_{j=1}^{n} y_j\phi_{ij}} \tag{4-63}$$

Where y_i is the mole fraction of component i, μ_i is the viscosity of pure component i and ϕ_{ij} is calculated as follows:

$$\phi_{ij} = \sqrt{\frac{MM_i}{MM_j}} = \phi_{ji}^{-1} \tag{4-64}$$

4.3.4 Thermal conductivity

The pure component gas thermal conductivity was calculated using an empirical polynomial equation found in Todd et al. (2002). The gas mixture thermal conductivity was evaluated using Wassiljewa's empirical relation (4-41).

$$\lambda = \sum_{i=1}^{n} \frac{y_i \lambda_i}{\sum_{j=1}^{n} y_j A_{ij}} \tag{4-65}$$

Where y_i is the mole fraction of the ith component, λ_i is the thermal conductivity of the pure component i. The term A_{ij} is calculated using the Mason and Saxena modification (4-42). Note that equation (4-41) has the the same form of the viscosity mixture equation.

$$A_{ij} = \frac{\varepsilon \left(1 + \left(\lambda_{tr_i} / \lambda_{tr_j} \right)^{1/2} \left(MM_i / MM_j \right)^{1/4} \right)^2}{\left(8 \left(1 + MM_i / MM_j \right) \right)^{1/2}} \tag{4-66}$$

Where MM_i is the molecular mass, λ_{tr} is the monoatomic thermal conductivity of the component and ε is a constant equal to 0.85 standing to Tandon and Saxena (1965). With few calculations it can be demonstrated that $A_{ij} = \varepsilon \phi_{ij}$. Therefore, the calculation of both viscosity and thermal conductivity of the mixture can be calculated starting from the pure component proprieties and using the same relationship for the mixture.

Inside the pellet the effective thermal conductivity was calculating using the weighted average between the gas and the solid conductivity using the porosity:

$$\lambda_e = \varepsilon \lambda_G + (1 - \varepsilon) \lambda_S \tag{4-67}$$

Where λ_e is the effective heat conductivity, λ_G is the gas heat conductivity, λ_S the solid heat conductivity and ε the particle porosity.

4.4 Steady state reactor performances

As mentioned in the introduction, the simulation involves a multichannel reactor. The channels are tubular, and a single channel is simulated. A 2-D axisymmetric model is used because due to the highly exothermic reaction and poor conductivity of the bed a high radial gradient will be present as reported in previous studies [128].

The chosen reactor length for the following results is 0.5 m and the ratio between the reactor diameter and the catalyst pellet is equal to 10 in order to avoid channelling. The bed and catalyst proprieties are summarized in .

The effect of the coolant temperature (T_c) was investigated for a channel diameter of 8 mm and space velocity GHSV=16000 h^{-1}. The coolant temperature was varied between 250 and 280°C. For T_c=250 °C the temperature increases on

the axis of the reactor channel by maximum 15° and modest CO_2 conversion of 22% is obtained. As the coolant temperature is raised to 260°C a peak temperature of 480°C is reached due to the ignition of the reactor and a CO_2 conversion of 65% is obtained. Increasing the temperature further up to 280°C can lead to a CO_2 conversion up to 80%. The hot spot temperature would reach temperatures up to 580°C and may damage the catalyst rapidly. Furthermore, increasing the temperature moves the peak temperature towards the reactor inlet due to higher volumetric heat generation. The results are reported in Figure 4-8.
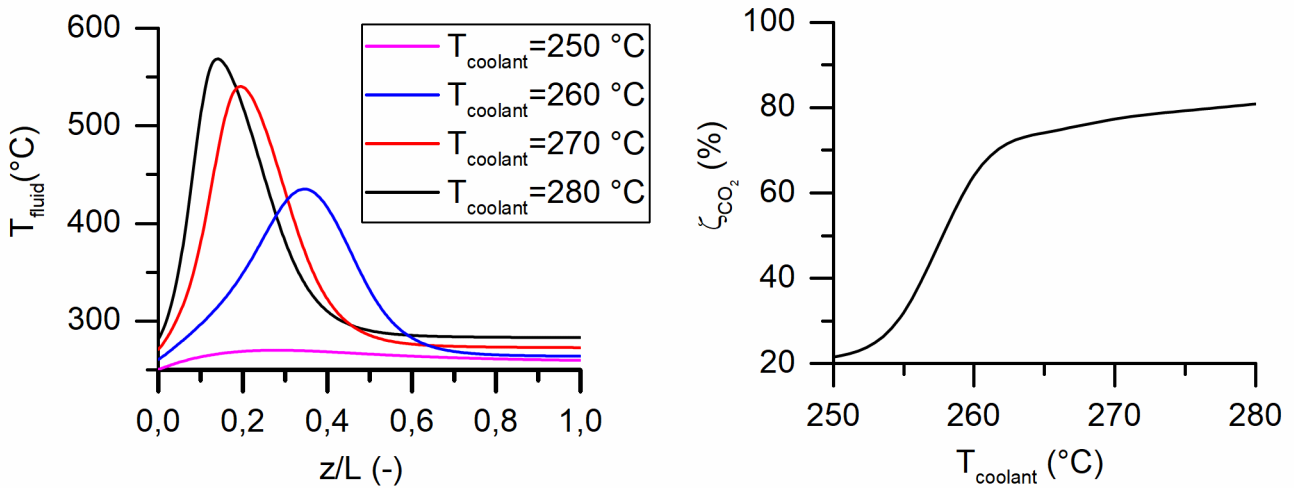
Figure 4-8: Effect of coolant temperature on the reactor temperature profile (left) and CO_2 conversion (right) (d_t=8mm, NT=120, P=4 bar)

In Figure 4-9 the radial temperature profile can be appreciated. At 280°C of coolant temperature the radial temperature difference passes from 565°C to the wall temperature of 280°C in 4 mm of radius length.
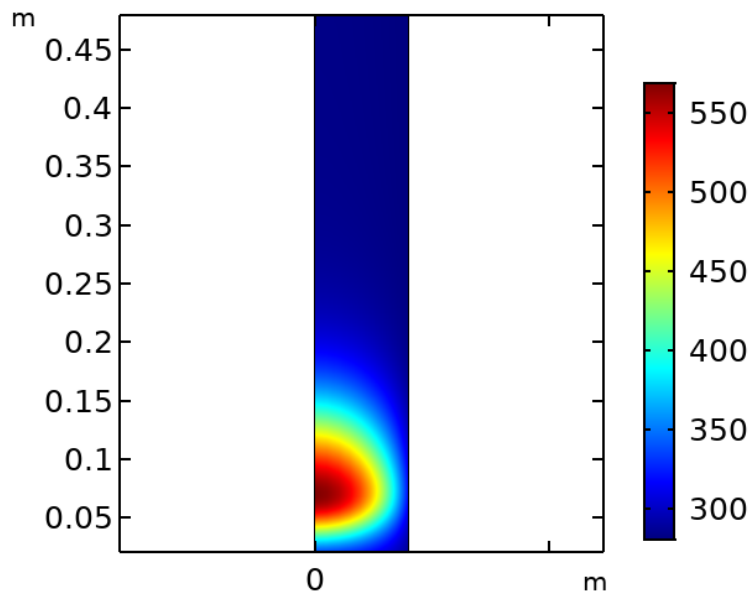
Figure 4-9: Temperature map of the reactor for d_t=8mm T_c=280°C P=4 bar

With the same operating conditions as the ones above, the concentration profile inside the catalyst was investigated. In Figure 4-10 the concentration and

89

the temperature profiles for the fluid phase and catalyst surface and centre are re. External mass transport limitations are not present in the operating conditions. While inside the catalytic pellet there is a strong concentration gradient due diffusion limitation inside the pores of the catalyst. In fact, near the hot spot a complete depletion of CO_2 at the centre of the catalyst is obtained. Hydrogen on the other hand does never go to depletion, even if it is consumed 4 times faster, due to a higher equivalent diffusion (i.e. one order of magnitude higher than CO_2). For the temperature profile there is a slight external heat transfer limitation giving of maximum temperature difference between the fluid and the pellet of about 10 °C. No internal heat transfer limitations are obtained for the studied case.
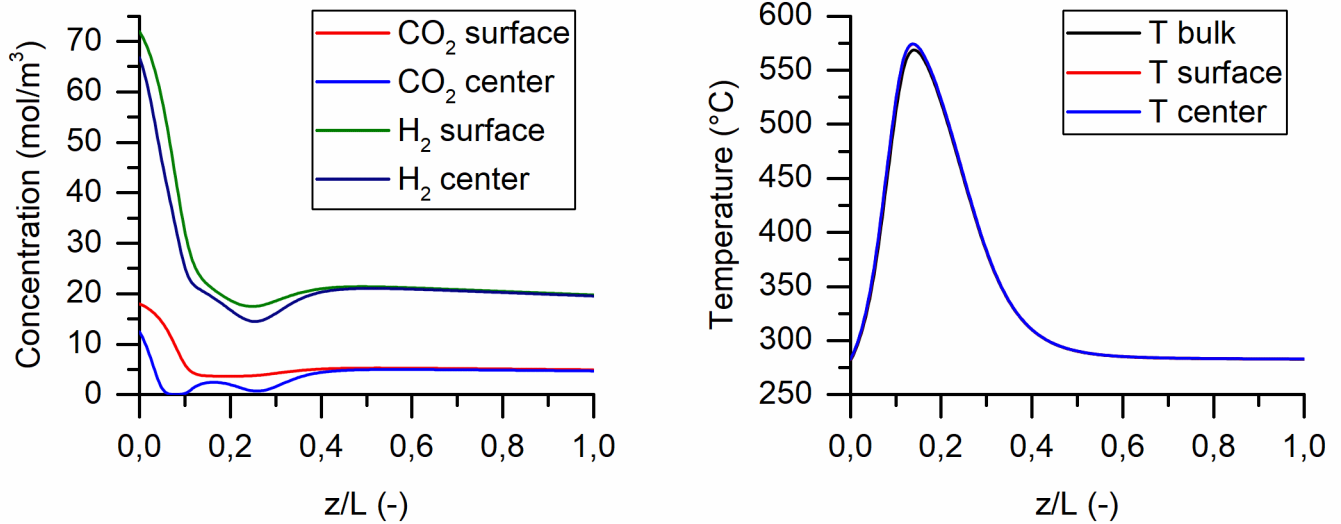
Figure 4-10: CO_2 and H_2 concentration on the pellet surface and centre (left) and temperature (right) profiles inside the pellet (surface and center) and in in fluid along the reactor axis. The simulation was carried out on for a reactor operating with d_t=8 mm, T_c=280 °C and p=4 bar

A catalyst utilization factor (effectiveness factor) can be defined as the ratio between the actual converted reactant and the converted reactant if the reaction rate were constant and equal to the surface rate along the entire pellet (4-68).

$$\eta_j = \frac{\int_0^{V_p} r_j(C,T)dV}{\int_0^{V_p} r_j(C^S,T^S)dV}$$

(4-68)

Where $r_j(C,T)$ is the reaction rate along the catalyst pellet and $r_j(C^S,T^S)$ is the reaction rate with the catalyst surface conditions of concentrations and temperature. The effectiveness factor for the three reactions is reported in Figure 4-11. A strong CO_2 concentration gradient inside the pellet implies that the effectiveness factor in this region will be significantly lower than unity due to reactant starvation for the CO_2 methanation reaction and RWGS. This is caused by the strong increase in the reaction temperature reached at the inlet of the reactor. The CO methanation effectiveness is higher than 1 towards the inlet of the reaction because carbon monoxide is produced inside the pellet by the RWGS reaction. Therefore, the CO concentration increases inside the pellet compared to the surface and CO methanation rate along the pellet coordinate. Around the peak temperature the maximum CO yield is also reached. As the temperature drops after the hot spot due to the lack of reactants, CO becomes thermodynamically

unfavoured and will start to go back to CO_2 (water gas shift) and to methane by CO methanation. In fact, it was found that for the RWGS two sign changes are obtained for the effectiveness factor. Finally, towards the reactor exit the effectiveness factors for all rates tend towards unity because the reaction rates slow down due to the approach to the thermodynamic equilibrium.
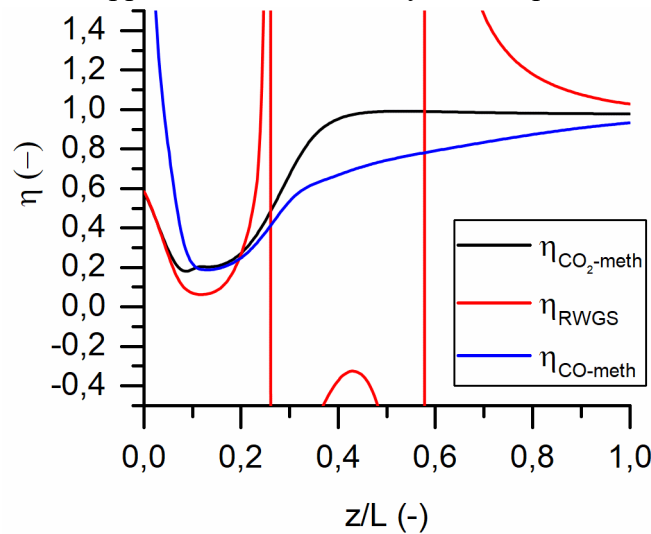
Figure 4-11: Effectiveness factor along the axial coordinate of the reactor for d_t=8 mm, T_c=280 °C and p=4 bar

The effect of the total pressure on the temperature profile and CO_2 conversion was investigate in the range 2 to 10 bar. The analysis was performed using a tube diameter of 8 mm with GHSV=16000 h^{-1} and a coolant temperature of 280°C. At 2 bar of total pressure the maximum temperature reached is 405°C with a CO_2 conversion of 67%. Increasing the pressure beyond 4 bar will give a modest increase in CO_2 conversion. In fact, going from 4 bar to 10 bar the conversion 80% to 86%. This is mainly caused mainly by the poor activity of the catalyst at low temperature that occurs at after the hot spot. Furthermore, the hot spot will be narrower and will move towards the inlet where ma majority of the reactants are consumed. The results are reported in Figure 4-12.
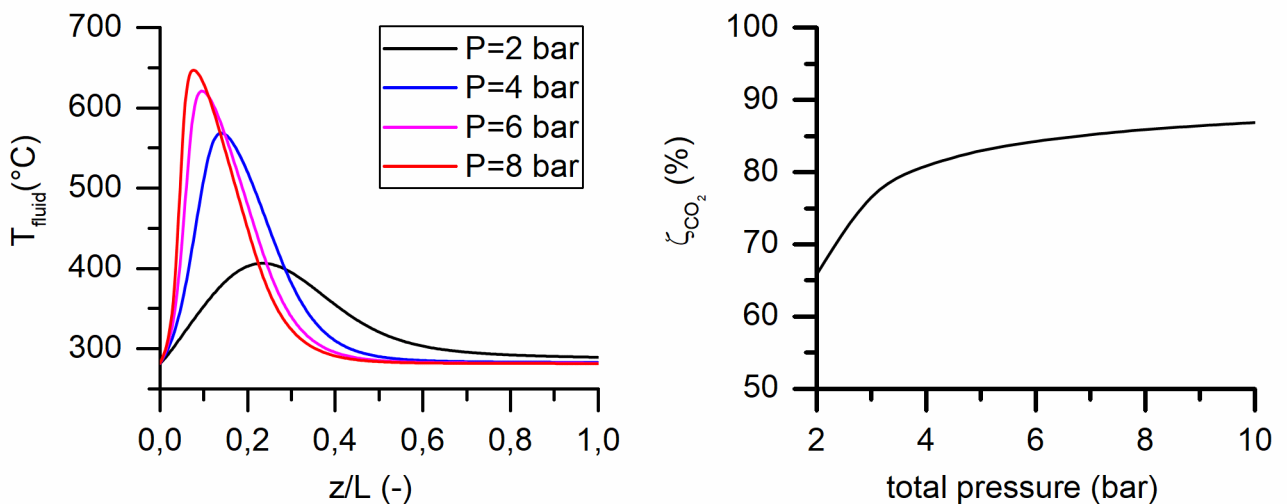
Figure 4-12: Effect of operating pressure on the temperature profile and CO2 conversion (dt=8mm, NT=120, Tc=280°C)

91

The effect of the geometry of the reactor on the reactor performance was investigated. In particular the channel diameter was varied between 6 and 10 mm. The simulations were carried out for a coolant temperature of 275°C and with fixed space velocity (GHSV = 16000 h^{-1}). The temperature profiles and CO_2 conversions are reported in Figure 4-13. The smaller channels have a higher area to volume ratio. This guarantees a more efficient heat removal and temperature control. In fact, for a tube diameter of 6 mm the hot spot temperature is 455°C and the 65% of CO_2 conversion is reached. For the larger tube diameters, the hot spot temperature increases in intensity with the maximum in the same position. Furthermore, the amplitude of the hot spot increases, occupying a larger part of the bed. In this case the conversion rises as the diameter of the tube is increased and consequently a higher temperature is reached that could lead to a faster aging process.
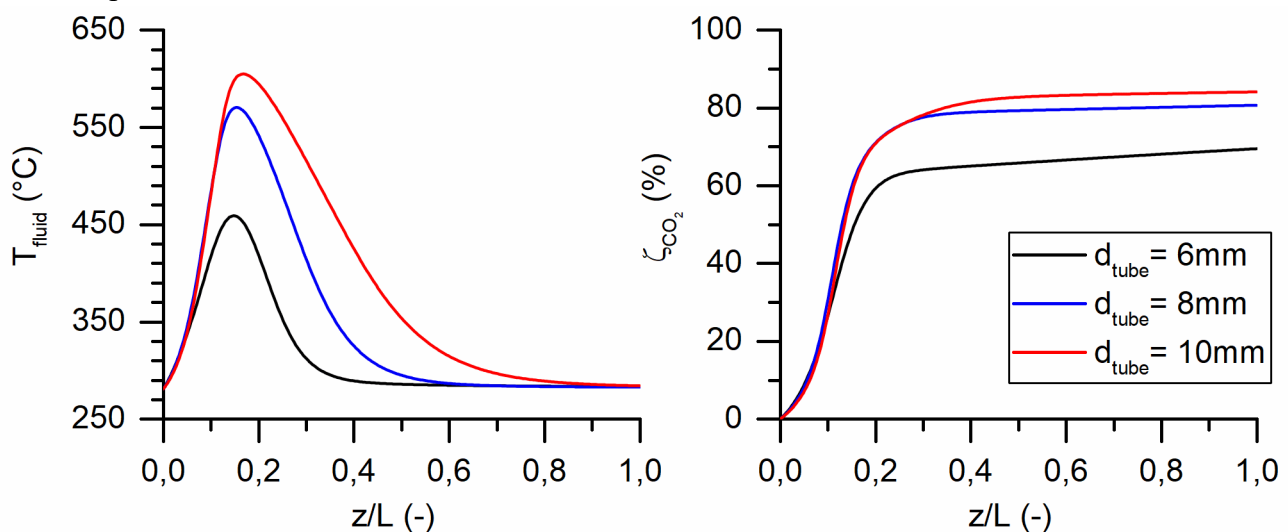
Figure 4-13: Effect of the tube diameter (constant GHSV=16000 h-1) on the temperature profile and CO_2 conversion

Finally, the effect of the space velocity was investigated between 9500 and 66000 Nm^3/h/m$^3_{bed}$ by varying the number of tubes of the reactor (NT=30-210 Table 4-2). Lowering the space velocity from 16600 Nm^3/h/m$^3_{bed}$ (increasing the number of tubes) will shift the position of the hot spot towards the inlet. Furthermore, the intensity of the peak also diminishes. This is caused by the balance between heat generation and heat rejection. The decrease in space velocity has the effect of reducing the heat exchange coefficient due to a lower gas speed. A lower space velocity also means that the volumetric heat generation will be lower due to a lower reactants flow rate and hence a lower converted quantity. When the space velocity is increased the opposite will happen. The heat exchange coefficient will increase increasing the heat rejection capacity but also the heat generation will increase due to higher reactants flow rate. The result will be that the hot spot gets wider and the maximum temperature reached will increase. The results are reported in Figure 4-14 (left). In both cases the surface to volume ratio of the reactor channels will determine the intensity of the phenomena described above. The effect of the space velocity on the performance of the

reactor is reported in Figure 4-14 (right). At high space velocity the CO_2 conversion reduces, and a higher yield of CO is obtained caused by the high temperature reached along all the reactor. A correct balance between the hot spot temperature and space velocity is required in order to improve the longevity of the catalyst and the desired conversion.

Table 4-2: Number of tubes conversion to GHSV

Number of tubes	Gas Hourly Space Velocity $(Nm^3/h/m^3_{bed})$
30	66600
60	33300
120	16600
180	11100
210	9500
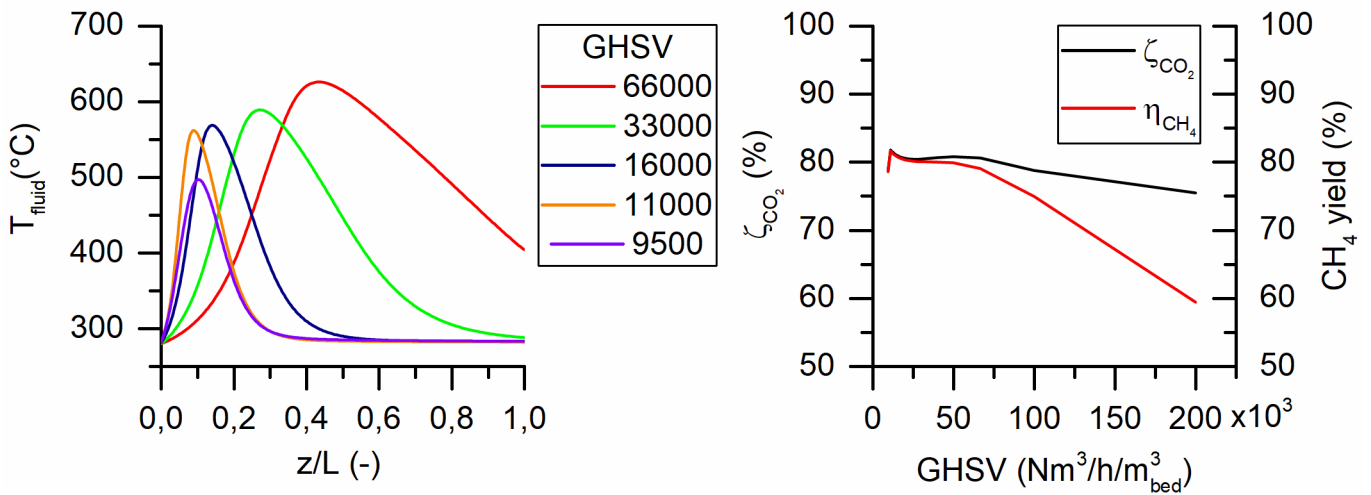
Figure 4-14: Effect of the number of tubes (effect of GHSV) on the temperature profile and CO_2 conversion

4.5 Aging effects on the reactor performances

The effect of catalyst aging on the reactor performance was studied for the reactor configuration with dt=8 mm and 120 tubes (GHSV=16600 $Nm^3/h/m^3_{bed}$). The chosen operating conditions are coolant temperature equal to 280°C and outlet pressure of 4 bar. A general power law expression (GPLE) was used to express the aging kinetics:

$$-\frac{da}{dt} = k_{d,Tref} \exp\left(\frac{E_{A,d}}{R}\left(\frac{1}{T_{ref}} - \frac{1}{T}\right)\right)(a - a_{eq})^2 \frac{P_{H_2O}}{P_{H_2}^{0.5}}$$

(4-69)

It was considered that the same law is valid for all the reaction rates meaning that the aging process has the same effect. This kind of aging kinetics allows to take into account the fact that aging phenomena have an asymptotic behaviour and that at the end of the catalyst life span there will still be a residual activity [127], [145]. Furthermore, the sintering in this was considered to be activated by the presence of water and inhibited by hydrogen. The parameters for the GPLE are summarized in Table 4-3.

Table 4-3: GPLE aging rate parameters

Parameter	Value
T_{ref} (K)	573.15
$k_{d,T_{ref}}$ (h^{-1})	$3.78 \cdot 10^{-4}$
$E_{A,d}$ (kJ/mol)	112.0
a_{eq} (−)	0.4

In Figure 4-15 the effect of catalyst aging on the axial temperature profile and on the conversion is reported. The hot spot temperature gets lower as aging proceeds. The position remains pretty much the same because at the entrance of the reactor the catalyst has basically the same activity because water is not present in the feed stream. This is confirmed by the conversion that remains at around 20% in the first 10% of the bed through the 1000h of simulated time on stream. For the peak to move the aging should bring the residual activity at the entrance towards zero. The tail of the temperature peak becomes wider due to less conversion taking place in the hot spot caused by the lower temperature peak reached. Therefore, on the right side of the hot spot an increase of the temperature is predicted. It is interesting to note that the conversion takes place mainly in the first 40% of the reactor and very little in the rest with this catalyst and reactor configuration.
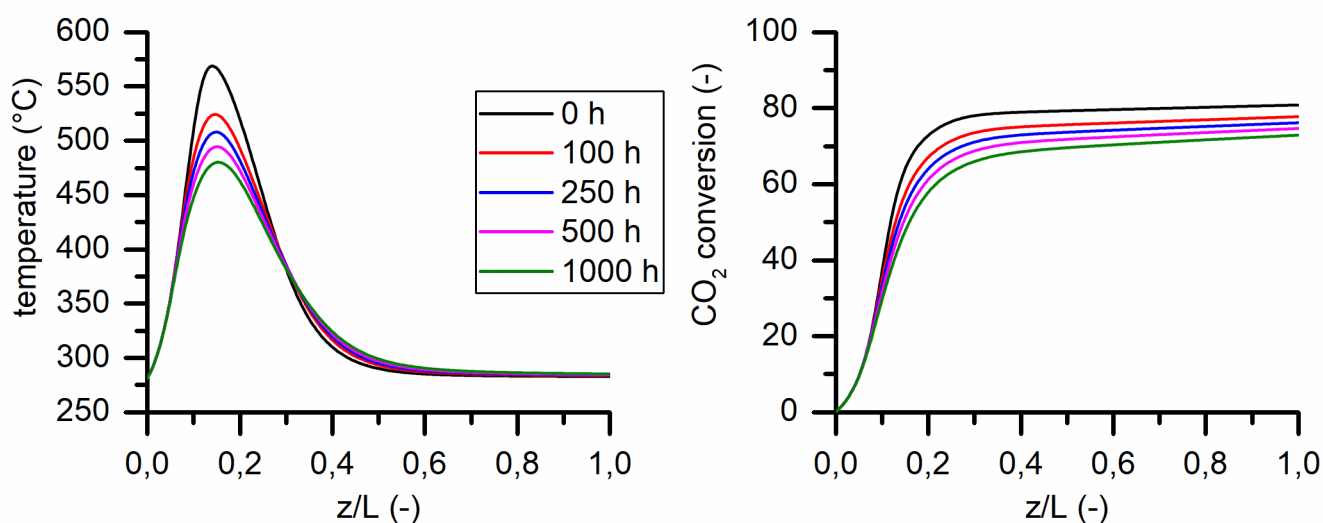
Figure 4-15: Effect of aging on reactor temperature profile and CO₂ conversion along the reactor

In Figure 4-16 the catalyst activity along the reactor is reported for different time on stream. As previously mentioned, at the entrance of the reactor water is not present and the temperature is not high for the aging to take place. The activity around the hot spot goes towards the asymptotic value of 0.4 fast in the first 100 h of time on stream. The rest of the catalyst does not lose activity because the temperature is not sufficiently high, and the slight activity loss observed for the last 50% of the bed is due mainly to the effect of the large amount of water present in the stream. Lastly, the difference in the activity between the surface and the centre of the catalyst is caused by water that is the product of the reactions and is being produced inside the pellet. Therefore, a water concentration gradient will

be present inside the pellet while hydrogen is consumed and will be less going towards the centre of the pellet.
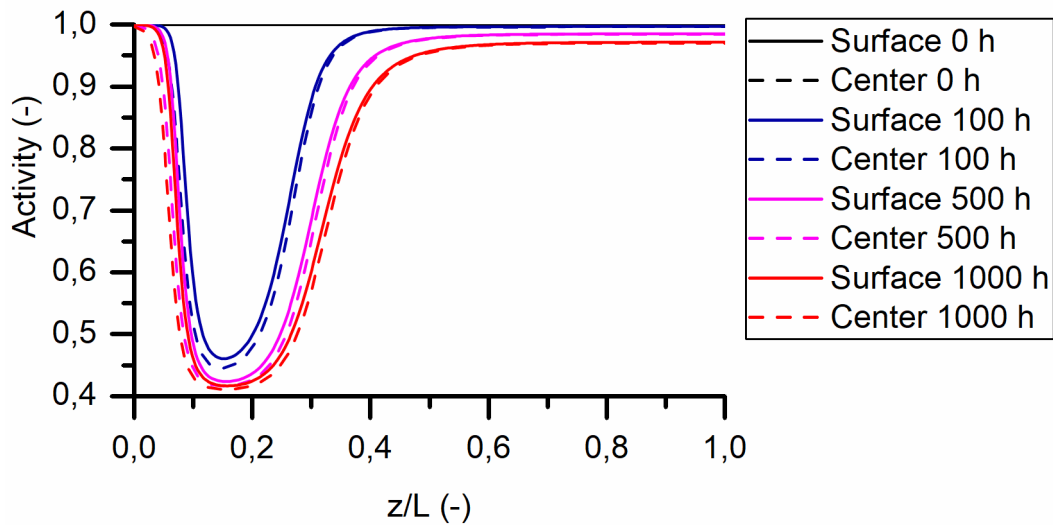
Figure 4-16: Catalyst activity along the reactor centre

In Figure 4-17 the reactor performance in terms of carbon dioxide conversion and methane yield is report as a function of time on stream. The CO_2 conversion drops from 81% to 74% in 1000 h of time on stream. Interesting fact is that the methane yield passes from being basically equal to the conversion (100% selectivity towards methane) to a slightly lower value. In fact, after 1000h of time on stream a 0.3% difference between CO_2 conversion and in methane yield is obtained. This phenomenon was also observed experimentally and presented in section 3.2.1.
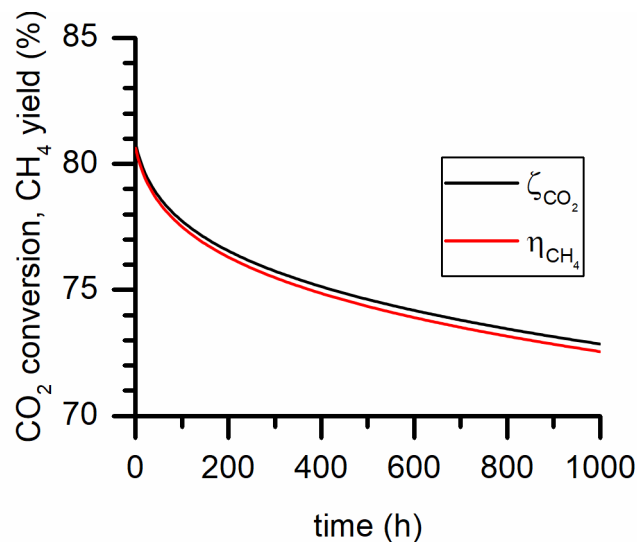
Figure 4-17: CO₂ conversion and methane evolution in time

In order to limit the effect of catalyst aging on the reactor performance some operating parameters can be adjusted. The coolant temperature could be increased by a few degrease or the operating pressure. In Figure 4-18 the of the performance by increasing both temperature and pressure for a catalytic bed that was uniformly aged to a=0.6. The temperature was varied between 280 and 300 °C and the

pressure between 4 and 6 bar. Many combinations of pressure and coolant temperature manage to restore the initial performance of the reactor.
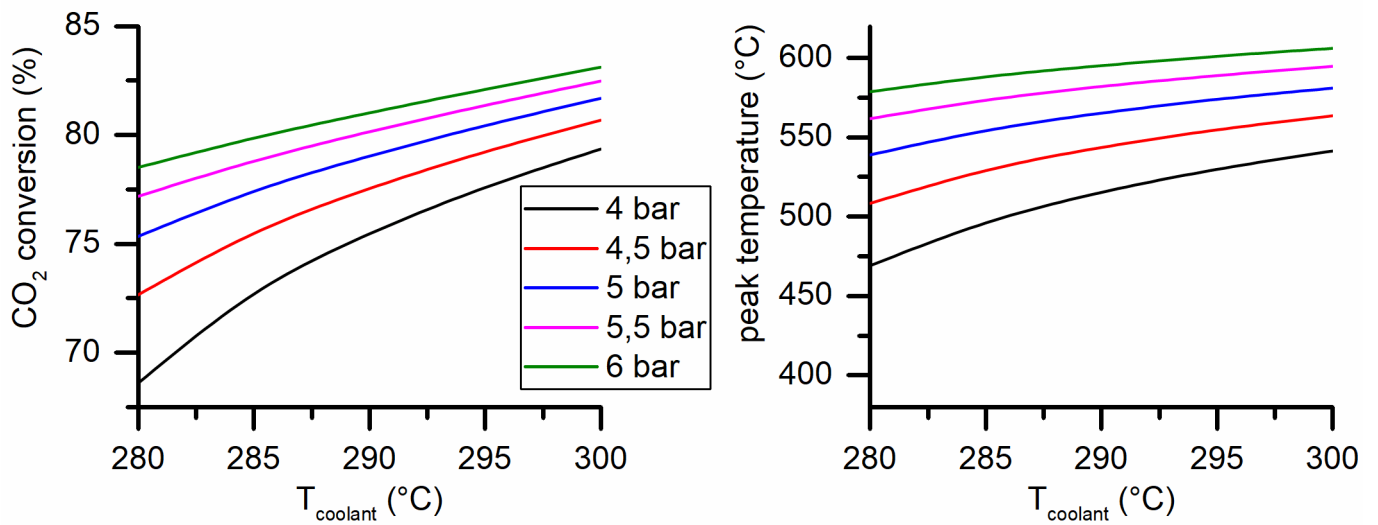
Figure 4-18: Sensitivity analysis varying coolant temperature and pressure in order to restore the initial CO₂ conversion for a reactor aged uniformly with residual activity=0.6

Conclusions

The objective of this work can be summarized in three parts:

> ➢ Perform the process modelling of the plant concept to produce synthetic LNG using hydrogen generated from excess renewable electricity and carbon dioxide captured from air was analysed in this study.
> ➢ Using the individuated compositions of the process modelling a catalytic test campaign was performed in order to investigate the catalytic aging process under realistic conditions. Furthermore, a full kinetic model that include the aging law and the intrinsic kinetic rate laws was developed.
> ➢ Finally, a multitube reactor model that included the aging catalyst aging effect was implemented in order to understand the impact that aging has on the reactor performance and how can be limited.

The process simulations of the concept was performed including optimisation of single units and whole plant by including thermal integration. The simulation model accounted for the efficiency of commercially available technologies (i.e. electrolysis and CO_2 capture).

A membrane gas separation system was developed: screening of different membranes and choosing the appropriate module layout. A two-stage membrane system resulted adequate for the stream purification. Besides this, choosing the appropriate separation system would give the possibility for the produced gas to be injected into the natural gas grid or undergo liquefaction allowing for a flexible operation. Afterwards, the optimization of the SMR liquefaction system confirmed that the tested refrigerant compositions can be used. Among the several considered mixtures, the ethylene-propane refrigerant gave the lowest energy consumption of 0.57 kWh/kg_{LNG}.

After heat recovery an overall plant efficiency of 46.3% electrical to chemical conversion was calculated for the demo plant. However, the use of an electrolysis system operating temperatures higher than 140 °C would allow to recover the produced heat and use it in the carbon dioxide capturing unit and the two TSA modules. This would allow to reach an electrical to chemical efficiency of 52.6%.

A thermodynamic analysis focused on the methanation reactor excluded the carbon formation in the range of possible operating conditions. Therefore, carbon deposition is thermodynamically unfavoured. This doesn't exclude the possibility of carbon deposition occurring for kinetic reasons. The aging of a commercial nickel-based catalyst was performed in process relevant conditions of temperature, pressure and feed gas composition.

The feed gas composition was determined through the process modelling of the gas separation system that contains recycle streams. It was determined through 100h long tests that catalyst ages at temperature above 350 °C with a slow and gradual loss of activity.

In order to understand the cause of aging was individuated by performing the following catalyst characterisation techniques: temperature programmed combustion (TPC), X-ray diffractometry (XRD) and nitrogen adsorption isotherm for surface area determination through the BET technique. The TPC analysis allowed to exclude carbon deposition as a possible cause of deactivation. Through the XRD it was excluded any phase change of the nickel active metal (i.e. the nickel did not react with the alumina support to form $NiAl_2O_4$). The culprit was found by the BET analysis. A huge total area decrease was discovered that can be caused by the alumina support sintering.

A kinetic analysis was performed on a fresh and aged sample. The activation energy does not change between the samples meaning that there is no change in the reaction mechanism. Furthermore, a perfect correlation was found between the ratio of the surface areas of the fresh and aged samples and the preexponential factor of the rate equation. To complete the kinetic description of the catalyst the intrinsic kinetics was determined and a LHHW model was fitted to the experimental data.

Finally, a multitube methanation reactor was in order to understand the effects of the operating conditions (temperature, pressure, space velocity) and the geometry in the temperature profiles and performance. An aging law was used in the model in order to consider the aging effect on the conversion rate. It was determined that to manage the declining performance caused by aging it is sufficient to adjust the operating temperature and pressure of the system to restore the initial conversion rates.

Future perspectives

In Chapter 3 the effect of catalyst aging on the performance was reported and the main cause of deactivation was determined. Secondary effects, like nickel particle growth, could also be present and may be interesting to study.

In Chapter 4 the reactor modelling of a multitube methanation reactor was performed. The steady state simulations have evidenced that most of the catalytic bed is inactive. Therefore, an optimization of the reactor design should be carried out in order to improve the catalyst utilization. Furthermore, a methanation reactor line could be designed and sized.

References

[1]   Intergovernmental Panel on Climate Change, "Climate Change 2014 Synthesis Report - IPCC," 2014.

[2]   A. Zervos, C. Lins, and L. Tesnière, "Mapping Renewable Energy Pathways towards 2020," *Eur. Renew. Energy Counc.*, p. 28, 2011.

[3]   P. Marocco *et al.*, "CO_2 methanation over Ni/Al hydrotalcite-derived catalyst: Experimental characterization and kinetic study," *Fuel*, vol. 225, pp. 230–242, Aug. 2018.

[4]   W. E. Outlook and Internation Energy Agency, "World Energy Outlook 2016," Paris, 2016.

[5]   D. O. Akinyele and R. K. Rayudu, "Review of energy storage technologies for sustainable power networks," *Sustain. Energy Technol. Assessments*, vol. 8, pp. 74–91, Dec. 2014.

[6]   H. Ibrahim, A. Ilinca, and J. Perron, "Energy storage systems-Characteristics and comparisons," *Renew. Sustain. Energy Rev.*, vol. 12, no. 5, pp. 1221–1250, Jun. 2008.

[7]   F. Salomone, E. Giglio, D. Ferrero, M. Santarelli, R. Pirone, and S. Bensaid, "Techno-economic modelling of a Power-to-Gas system based on SOEC electrolysis and CO_2 methanation in a RES-based electric grid," *Chem. Eng. J.*, vol. 377, p. 120233, Dec. 2019.

[8]   E. Giglio *et al.*, "Power-to-Gas through High Temperature Electrolysis and Carbon Dioxide Methanation: Reactor Design and Process Modeling," *Ind. Eng. Chem. Res.*, vol. 57, no. 11, pp. 4007–4018, Mar. 2018.

[9]   I. Hadjipaschalis, A. Poullikkas, and V. Efthimiou, "Overview of current and future energy storage technologies for electric power applications," *Renew. Sustain. Energy Rev.*, vol. 13, no. 6–7, pp. 1513–1522, Aug. 2009.

[10]   K. C. C. Divya and J. Østergaard, "Battery energy storage technology for power systems-An overview," *Electr. Power Syst. Res.*, vol. 79, no. 4, pp. 511–520, Apr. 2009.

[11]   H. Lund and G. Salgi, "The role of compressed air energy storage (CAES) in future sustainable energy systems," *Energy Convers. Manag.*, vol. 50, no. 5, pp. 1172–1179, May 2009.

[12]   J. P. Deane, B. P. Ó Gallachóir, and E. J. McKeogh, "Techno-economic review of existing and new pumped hydro energy storage plant," *Renew. Sustain. Energy Rev.*, vol. 14, no. 4, pp. 1293–1302, May 2010.

[13]   M. Götz *et al.*, "Renewable Power-to-Gas: A technological and economic review," *Renew. Energy*, vol. 85, pp. 1371–1390, Jan. 2016.

[14]   N. Meiri, R. Radus, and M. Herskowitz, "Simulation of novel process of CO_2 conversion to liquid fuels," *J. CO2 Util.*, vol. 17, pp. 284–289, Jan.

2017.

[15] H. Chen, T. N. Cong, W. Yang, C. Tan, Y. Li, and Y. Ding, "Progress in electrical energy storage system: A critical review," *Prog. Nat. Sci.*, vol. 19, no. 3, pp. 291–312, Mar. 2009.

[16] A. Castillo and D. F. Gayme, "Grid-scale energy storage applications in renewable energy integration: A survey," *Energy Convers. Manag.*, vol. 87, pp. 885–894, 2014.

[17] X. Luo, J. Wang, M. Dooner, and J. Clarke, "Overview of current development in electrical energy storage technologies and the application potential in power system operation," *Appl. Energy*, vol. 137, pp. 511–536, Jan. 2015.

[18] M. Specht *et al.*, "Storing bioenergy and renewable electricity in the natural gas grid," in *FVEE AEE Topics 2009*, 2009, pp. 69–78.

[19] I. Kougias and S. Szabó, "Pumped hydroelectric storage utilization assessment: Forerunner of renewable energy integration or Trojan horse?," *Energy*, vol. 140, pp. 318–329, Dec. 2017.

[20] M. Beaudin, H. Zareipour, A. Schellenberglabe, and W. Rosehart, "Energy storage for mitigating the variability of renewable electricity sources: An updated review," *Energy Sustain. Dev.*, vol. 14, no. 4, pp. 302–314, Dec. 2010.

[21] C. Graves, S. D. Ebbesen, M. Mogensen, and K. S. Lackner, "Sustainable hydrocarbon fuels by recycling CO_2 and H_2O with renewable or nuclear energy," *Renew. Sustain. Energy Rev.*, vol. 15, no. 1, pp. 1–23, Jan. 2011.

[22] M. Bailera, P. Lisbona, L. M. Romeo, and S. Espatolero, "Power to Gas projects review: Lab, pilot and demo plants for storing renewable energy and CO_2," *Renew. Sustain. Energy Rev.*, vol. 69, no. October 2016, pp. 292–312, 2017.

[23] G. Reiter and J. Lindorfer, "Global warming potential of hydrogen and methane production from renewable electricity via power-to-gas technology," *Int. J. Life Cycle Assess.*, vol. 20, no. 4, pp. 477–489, Apr. 2015.

[24] G. A. Olah, A. Goeppert, and G. K. S. Prakash, "Chemical Recycling of Carbon Dioxide to Methanol and Dimethyl Ether: From Greenhouse Gas to Renewable, Environmentally Carbon Neutral Fuels and Synthetic Hydrocarbons," *J. Org. Chem.*, vol. 74, no. 2, pp. 487–498, 2009.

[25] D. H. König, N. Baucks, R.-U. U. Dietrich, and A. Wörner, "Simulation and evaluation of a process concept for the generation of synthetic fuel from CO_2 and H_2," *Energy*, vol. 91, pp. 833–841, Nov. 2015.

[26] A. Buttler and H. Spliethoff, "Current status of water electrolysis for energy storage, grid balancing and sector coupling via power-to-gas and power-to-liquids: A review," *Renew. Sustain. Energy Rev.*, vol. 82, no. February, pp. 2440–2454, 2018.

[27] T. Kuramochi, A. Ramírez, W. Turkenburg, and A. Faaij, "Comparative assessment of CO_2 capture technologies for carbon-intensive industrial processes," *Prog. Energy Combust. Sci.*, vol. 38, no. 1, pp. 87–112, Feb. 2012.

[28] R. Socolow *et al.*, "Direct Air Capture of CO_2 with Chemicals: A Technology Assessment for the APS Panel on Public Affairs." 2011.

[29] E. Ryckebosch, M. Drouillon, and H. Vervaeren, "Techniques for transformation of biogas to biomethane," *Biomass and Bioenergy*, vol. 35, no. 5, pp. 1633–1645, May 2011.

102

[30] R. Augelletti, M. Conti, and M. C. Annesini, "Pressure swing adsorption for biogas upgrading. A new process configuration for the separation of biomethane and carbon dioxide," *J. Clean. Prod.*, vol. 140, pp. 1390–1398, 2017.

[31] Eurobserv'ER, "Biogas Barometer." 2014.

[32] K. Hashimoto *et al.*, "Global CO_2 recycling—novel materials and prospect for prevention of global warming and abundant energy supply," *Mater. Sci. Eng. A*, vol. 267, no. 2, pp. 200–206, Jul. 1999.

[33] N. M. Mikhin and K. S. Lyapin, "Hardness dependence of the coefficient of friction," *Sov. Phys. J.*, vol. 13, no. 3, pp. 317–321, Dec. 1972.

[34] dena, "The Power to Gas Strategy Platform." [Online]. Available: http://www.powertogas.info/power-to-gas/pilotprojekte-im-ueberblick/audi-e-gas-projekt/. [Accessed: 08-Jan-2018].

[35] KIT, "Helmeth Project Documents." [Online]. Available: http://www.helmeth.eu/index.php/documents. [Accessed: 08-Jan-2018].

[36] J. N. Park and E. W. McFarland, "A highly dispersed Pd-Mg/SiO2 catalyst active for methanation of CO_2," *J. Catal.*, vol. 266, no. 1, pp. 92–97, 2009.

[37] M. A. A. Aziz, A. A. Jalil, S. Triwahyono, and A. Ahmad, "CO_2 methanation over heterogeneous catalysts: recent progress and future prospects," *Green Chem.*, vol. 17, no. 5, pp. 2647–2663, 2015.

[38] W. Wang and J. Gong, "Methanation of carbon dioxide: An overview," *Front. Chem. Eng. China*, vol. 5, no. 1, pp. 2–10, 2011.

[39] J. Gao, Q. Liu, F. Gu, B. Liu, Z. Zhong, and F. Su, "Recent advances in methanation catalysts for the production of synthetic natural gas," *RSC Adv.*, vol. 5, no. 29, pp. 22759–22776, 2015.

[40] G. Garbarino, P. Riani, L. Magistri, and G. Busca, "A study of the methanation of carbon dioxide on Ni/Al_2O_2 catalysts at atmospheric pressure," *Int. J. Hydrogen Energy*, vol. 39, no. 22, pp. 11557–11565, Jul. 2014.

[41] J. Zhang, Z. Xin, X. Meng, and M. Tao, "Synthesis, characterization and properties of anti-sintering nickel incorporated MCM-41 methanation catalysts," *Fuel*, vol. 109, pp. 693–701, 2013.

[42] C. K. Vance and C. H. Bartholomew, "Hydrogenation of carbon dioxide on group VIII metals," *Appl. Catal.*, vol. 7, no. 2, pp. 169–177, 1983.

[43] S. Tada, T. Shimizu, H. Kameyama, T. Haneda, and R. Kikuchi, "Ni/CeO2 catalysts with high CO_2 methanation activity and high CH4 selectivity at low temperatures," *Int. J. Hydrogen Energy*, vol. 37, no. 7, pp. 5527–5531, Apr. 2012.

[44] H. Liu, X. Zou, X. Wang, X. Lu, and W. Ding, "Effect of CeO_2 addition on Ni/Al_2O_3 catalysts for methanation of carbon dioxide with hydrogen," *J. Nat. Gas Chem.*, vol. 21, no. 6, pp. 703–707, Nov. 2012.

[45] M. Cai, J. Wen, W. Chu, X. Cheng, and Z. Li, "Methanation of carbon dioxide on Ni/ZrO_2-Al_2O_3 catalysts: Effects of ZrO_2 promoter and preparation method of novel ZrO_2-Al_2O_3 carrier," *J. Nat. Gas Chem.*, vol. 20, no. 3, pp. 318–324, May 2011.

[46] J. Liu *et al.*, "Enhanced low-temperature activity of CO_2 methanation over highly-dispersed Ni/TiO_2 catalyst," *Catal. Sci. Technol.*, vol. 3, no. 10, p. 2627, 2013.

[47] P. A. U. Aldana *et al.*, "Catalytic CO_2 valorization into CH_4 on Ni-based ceria-zirconia. Reaction mechanism by operando IR spectroscopy," *Catal. Today*, vol. 215, pp. 201–207, 2013.

[48] F. Ocampo, B. Louis, L. Kiwi-Minsker, and A.-C. Roger, "Effect of Ce/Zr composition and noble metal promotion on nickel based CexZr1−xO2 catalysts for carbon dioxide methanation," *Appl. Catal. A Gen.*, vol. 392, no. 1–2, pp. 36–44, Jan. 2011.

[49] S. Abate *et al.*, "Catalytic Performance of γ-Al$_2$O$_3$–ZrO$_2$–TiO2–CeO2 Composite Oxide Supported Ni-Based Catalysts for CO$_2$ Methanation," *Ind. Eng. Chem. Res.*, vol. 55, no. 16, pp. 4451–4460, Apr. 2016.

[50] L. Zhao, X. Li, X. Quan, and G. Chen, "Effects of surface features on sulfur dioxide adsorption on calcined NiAl hydrotalcite-like compounds," *Environ. Sci. Technol.*, vol. 45, no. 12, pp. 5373–5379, 2011.

[51] M. Gabrovska, R. Edreva-Kardjieva, D. Crişan, P. Tzvetkov, M. Shopska, and I. Shtereva, "Ni–Al layered double hydroxides as catalyst precursors for CO$_2$ removal by methanation," *React. Kinet. Mech. Catal.*, vol. 105, no. 1, pp. 79–99, 2011.

[52] L. He, Q. Lin, Y. Liu, and Y. Huang, "Unique catalysis of Ni-Al hydrotalcite derived catalyst in CO$_2$ methanation: Cooperative effect between Ni nanoparticles and a basic support," *J. Energy Chem.*, vol. 23, no. 5, pp. 587–592, 2014.

[53] D. Wierzbicki, R. Debek, M. Motak, T. Grzybek, M. E. Gálvez, and P. Da Costa, "Novel Ni-La-hydrotalcite derived catalysts for CO$_2$ methanation," *Catal. Commun.*, vol. 83, pp. 5–8, Aug. 2016.

[54] S. Abelló, C. Berrueco, and D. Montané, "High-loaded nickel–alumina catalyst for direct CO$_2$ hydrogenation into synthetic natural gas (SNG)," *Fuel*, vol. 113, pp. 598–609, Nov. 2013.

[55] S. Abate *et al.*, "Synthesis, Characterization, and Activity Pattern of Ni–Al Hydrotalcite Catalysts in CO$_2$ Methanation," *Ind. Eng. Chem. Res.*, vol. 55, no. 30, pp. 8299–8308, Aug. 2016.

[56] S. Sharma, Z. Hu, P. Zhang, E. W. McFarland, and H. Metiu, "CO$_2$ methanation on Ru-doped ceria," *J. Catal.*, vol. 278, no. 2, pp. 297–309, Mar. 2011.

[57] D. C. Upham, A. R. Derk, S. Sharma, H. Metiu, and E. W. McFarland, "CO$_2$ methanation by Ru-doped ceria: the role of the oxidation state of the surface," *Catal. Sci. Technol.*, vol. 5, no. 3, pp. 1783–1791, 2015.

[58] Y. Zhu *et al.*, "Catalytic conversion of carbon dioxide to methane on ruthenium-cobalt bimetallic nanocatalysts and correlation between surface chemistry of catalysts under reaction conditions and catalytic performances," *ACS Catal.*, vol. 2, no. 11, pp. 2403–2408, 2012.

[59] A. Karelovic and P. Ruiz, "CO$_2$ hydrogenation at low temperature over Rh/γ-Al$_2$O$_3$ catalysts: Effect of the metal particle size on catalytic performances and reaction mechanism," *Appl. Catal. B Environ.*, vol. 113–114, pp. 237–249, Feb. 2012.

[60] S. K. Beaumont *et al.*, "Combining in situ NEXAFS spectroscopy and CO$_2$ methanation kinetics to study Pt and Co nanoparticle catalysts reveals key insights into the role of platinum in promoted cobalt catalysis," *J. Am. Chem. Soc.*, vol. 136, no. 28, pp. 9898–9901, 2014.

[61] J. H. Kwak, L. Kovarik, and J. Szanyi, "Heterogeneous Catalysis on Atomically Dispersed Supported Metals: CO$_2$ Reduction on Multifunctional Pd Catalysts," *ACS Catal.*, vol. 3, no. 9, pp. 2094–2100, Sep. 2013.

[62] N. Srisawad, W. Chaitree, O. Mekasuwandumrong, A. Shotipruk, B. Jongsomjit, and J. Panpranot, "CO2 hydrogenation over Co/Al2O3

catalysts prepared via a solid-state reaction of fine gibbsite and cobalt precursors," *React. Kinet. Mech. Catal.*, vol. 107, no. 1, pp. 179–188, Oct. 2012.

[63] S. Kato *et al.*, "CO_2 hydrogenation on a metal hydride surface," *Phys. Chem. Chem. Phys.*, vol. 14, no. 16, p. 5518, 2012.

[64] S. K. Hoekman, A. Broch, C. Robbins, and R. Purcell, "CO_2 recycling by reaction with renewably-generated hydrogen," *Int. J. Greenh. Gas Control*, vol. 4, no. 1, pp. 44–50, Jan. 2010.

[65] H. Hiller *et al.*, *Gas Production. Ullmann's Encyclopedia of Industrial Chemistry.* Wiley Online Library, 2006.

[66] J. Kopyscinski, T. J. Schildhauer, and S. M. A. Biollaz, "Production of synthetic natural gas (SNG) from coal and dry biomass - A technology review from 1950 to 2009," *Fuel*, vol. 89, no. 8, pp. 1763–1783, 2010.

[67] J. . Jensen, J. . Poulsen, and N. . Andersen, "From Coal To Clean Energy," *Nitrogen+Syngas*, no. April. pp. 1–5, 2011.

[68] U.S. Department of Energy - Office of Fossil Energy, "Practical experience gained during the first twenty years of operation of the Great Plains Gasification Plant and implications for future projects," 2006.

[69] M. Sudiro and A. Bertucco, "Synthetic Natural Gas (SNG) from coal and biomass: a survey of existing process technologies, open issues and perspectives." InTech, 2010.

[70] W. P. Haynes and A. J. Forney, "High BTU gas from coal: status and prospects," 1976.

[71] S. Rönsch *et al.*, "Review on methanation - From fundamentals to current projects," *Fuel*, vol. 166, pp. 276–296, Feb. 2016.

[72] C. Janke, M. S. Duyar, M. Hoskins, and R. Farrauto, "Catalytic and adsorption studies for the hydrogenation of CO_2 to methane," *Appl. Catal. B Environ.*, vol. 152–153, no. 1, pp. 184–191, Jun. 2014.

[73] Y. Liu and O. Hinrichsen, "CFD Simulation of Hydrodynamics and Methanation Reactions in a Fluidized-Bed Reactor for the Production of Synthetic Natural Gas," *Ind. Eng. Chem. Res.*, vol. 53, no. 22, pp. 9348–9356, Jun. 2014.

[74] J. T. J. Cobb and R. C. Streeter, "Evaluation of Fluidized-Bed Methanation Catalysts and Reactor Modeling," *Ind. Eng. Chem. Proc. Des. Dev.*, vol. 18, no. 4, pp. 672–679, 1979.

[75] J. Kopyscinski, T. J. Schildhauer, and S. M. A. Biollaz, "Methanation in a fluidized bed reactor with high initial CO partial pressure: Part II-Modeling and sensitivity study," *Chem. Eng. Sci.*, vol. 66, no. 8, pp. 1612–1621, 2011.

[76] F. Meng, Z. Li, J. Liu, X. Cui, and H. Zheng, "Effect of promoter Ce on the structure and catalytic performance of Ni/Al_2O_3 catalyst for CO methanation in slurry-bed reactor," *J. Nat. Gas Sci. Eng.*, vol. 23, pp. 250–258, Mar. 2015.

[77] J. Lefebvre, M. Götz, S. Bajohr, R. Reimert, and T. Kolb, "Improvement of three-phase methanation reactor performance for steady-state and transient operation," *Fuel Process. Technol.*, vol. 132, pp. 83–90, Apr. 2015.

[78] E. A. Morosanu, A. Saldivia, M. Antonini, and S. Bensaid, "Process Modeling of an Innovative Power to LNG Demonstration Plant," *Energy & Fuels*, vol. 32, no. 8, pp. 8868–8879, Aug. 2018.

[79] NGVA Europe, "NGVA Europe - NG Vehicle Catalogue," 2015. [Online]. Available: http://www.ngva.eu/ng-vehicle-catalogue. [Accessed: 03-Apr-

2017].

[80] DG MOVE, "LNG Blue Corridors," 2013. [Online]. Available: http://lngbc.eu/. [Accessed: 03-Apr-2017].

[81] International Gas Union, "Enabling clean marine transport," 2017.

[82] F. Burel, R. Taccani, and N. Zuliani, "Improving sustainability of maritime transport through utilization of Liquefied Natural Gas (LNG) for propulsion," *Energy*, vol. 57, no. October 1983, pp. 412–420, 2013.

[83] S. Kumar *et al.*, "LNG: An eco-friendly cryogenic fuel for sustainable development," *Appl. Energy*, vol. 88, no. 12, pp. 4264–4273, 2011.

[84] J. D. Holladay, J. Hu, D. L. King, and Y. Wang, "An overview of hydrogen production technologies," *Catal. Today*, vol. 139, no. 4, pp. 244–260, 2009.

[85] Y. Liu and G. Wang, "Membranes: Technology and Applications," in *Nanostructured Polymer Membranes*, 2nd ed., vol. 2, Hoboken, NJ, USA: John Wiley & Sons, Inc., 2016, pp. 27–88.

[86] T. Pettersen and K. M. Lien, "A new robust design model for gas separating membrane modules, based on analogy with counter-current heat exchangers," *Comput. Chem. Eng.*, vol. 18, no. 5, pp. 427–439, May 1994.

[87] W. Lim, K. Choi, and I. Moon, "Current status and perspectives of Liquefied Natural Gas (LNG) plant design," *Ind. Eng. Chem. Res.*, vol. 52, no. 9, pp. 3065–3088, 2013.

[88] C. W. Remeljej and A. F. A. A. Hoadley, "An exergy analysis of small-scale liquefied natural gas (LNG) liquefaction processes," *Energy*, vol. 31, no. 12, pp. 1669–1683, 2006.

[89] B. Austbø, S. W. Løvseth, and T. Gundersen, "Annotated bibliography-Use of optimization in LNG process design and operation," *Comput. Chem. Eng.*, vol. 71, pp. 391–414, Dec. 2014.

[90] L. Cao, J. Liu, and X. Xu, "Robustness analysis of the mixed refrigerant composition employed in the single mixed refrigerant (SMR) liquefied natural gas (LNG) process," *Appl. Therm. Eng.*, vol. 93, pp. 1155–1163, 2016.

[91] X. Xu, J. Liu, and L. Cao, "Optimization and analysis of mixed refrigerant composition for the PRICO natural gas liquefaction process," *Cryogenics (Guildf).*, vol. 59, pp. 60–69, 2014.

[92] J. K. Adewole, A. L. Ahmad, S. Ismail, and C. P. Leo, "Current challenges in membrane separation of CO_2 from natural gas: A review," *Int. J. Greenh. Gas Control*, vol. 17, pp. 46–65, Sep. 2013.

[93] M. Gassner, R. Baciocchi, F. Maréchal, and M. Mazzotti, "Integrated design of a gas separation system for the upgrade of crude SNG with membranes," *Chem. Eng. Process. Process Intensif.*, vol. 48, no. 9, pp. 1391–1404, 2009.

[94] Z. Wang, D. Wang, F. Zhang, and J. Jin, "Tröger's base-based Microporous polyimide membranes for high-performance gas separation," *ACS Macro Lett.*, vol. 3, no. 7, pp. 597–601, Jul. 2014.

[95] W.-H. Lin and T.-S. Chung, "Gas permeability, diffusivity, solubility, and aging characteristics of 6FDA-durene polyimide membranes," *J. Memb. Sci.*, vol. 186, no. 2, pp. 183–193, May 2001.

[96] S. H. Han, J. E. Lee, K. J. Lee, H. B. Park, and Y. M. Lee, "Highly gas permeable and microporous polybenzimidazole membrane by thermal rearrangement," *J. Memb. Sci.*, vol. 357, no. 1–2, pp. 143–151, 2010.

[97] Union Gas Limited, "Union Gas," 2018. [Online]. Available: ttps://www.uniongas.com/about-us/about-natural-gas/chemical-

composition-of-natural-gas. [Accessed: 19-Jun-2018].

[98] E. Frank, J. Gorre, F. Ruoss, and M. J. Friedl, "Calculation and analysis of efficiencies and annual performances of Power-to-Gas systems," *Appl. Energy*, vol. 218, no. February, pp. 217–231, 2018.

[99] G. Gahleitner, "Hydrogen from renewable electricity: An international review of power-to-gas pilot plants for stationary applications," *Int. J. Hydrogen Energy*, vol. 38, no. 5, pp. 2039–2061, 2013.

[100] J. C. Ganley, "High temperature and pressure alkaline electrolysis," *Int. J. Hydrogen Energy*, vol. 34, no. 9, pp. 3604–3611, May 2009.

[101] F. Allebrod, C. Chatzichristodoulou, and M. B. Mogensen, "Alkaline electrolysis cell at high temperature and pressure of 250 °C and 42 bar," *J. Power Sources*, vol. 229, pp. 22–31, May 2013.

[102] A. Ursúa, L. M. Gandía, P. Sanchis, A. Ursua, L. M. Gandia, and P. Sanchis, "Hydrogen production from water electrolysis: Current status and future trends," *Proc. IEEE*, vol. 100, no. 2, pp. 410–426, 2012.

[103] A. D. Tevebaugh and E. J. Cairns, "Carbon Deposition Boundaries in the CHO System at Several Pressures.," *J. Chem. Eng. Data*, vol. 10, no. 4, pp. 359–362, Oct. 1965.

[104] V. Frick, J. Brellochs, and M. Specht, "Application of ternary diagrams in the design of methanation systems," *Fuel Process. Technol.*, vol. 118, pp. 156–160, 2014.

[105] C. BARTHOLOMEW, "Sintering of alumina-supported nickel and nickel bimetallic methanation catalysts in H_2/H_2O atmospheres," *J. Catal.*, vol. 79, no. 1, pp. 34–46, Jan. 1983.

[106] C. H. Bartholomew and W. L. Sorensen, "Sintering kinetics of silica- and alumina-supported nickel in hydrogen atmosphere," *J. Catal.*, vol. 81, no. 1, pp. 131–141, 1983.

[107] J. Sehested, A. Carlsson, T. V. . Janssens, P. . Hansen, and A. . Datye, "Sintering of Nickel Steam-Reforming Catalysts on $MgAl_2O_4$ Spinel Supports," *J. Catal.*, vol. 197, no. 1, pp. 200–209, Jan. 2001.

[108] J. Sehested, "Sintering of nickel steam-reforming catalysts," *J. Catal.*, vol. 217, no. 2, pp. 417–426, Jul. 2003.

[109] J. R. Rostrup-Nielsen, K. Pedersen, and J. Sehested, "High temperature methanationSintering and structure sensitivity," *Appl. Catal. A Gen.*, vol. 330, no. 1–2, pp. 134–138, Oct. 2007.

[110] F. Koschany, D. Schlereth, and O. Hinrichsen, "On the kinetics of the methanation of carbon dioxide on coprecipitated $NiAl(O)_x$," *Appl. Catal. B Environ.*, vol. 181, pp. 504–516, Feb. 2016.

[111] S. Ewald, M. Kolbeck, T. Kratky, M. Wolf, and O. Hinrichsen, "On the deactivation of Ni-Al catalysts in CO2 methanation," *Appl. Catal. A Gen.*, vol. 570, pp. 376–386, Jan. 2019.

[112] R. Try, A. Bengaouer, P. Baurens, and C. Jallut, "Dynamic modeling and simulations of the behavior of a fixed-bed reactor-exchanger used for CO_2 methanation," *AIChE J.*, vol. 64, no. 2, pp. 468–480, 2018.

[113] J. Ducamp, A. Bengaouer, and P. Baurens, "Modelling and experimental validation of a CO_2 methanation annular cooled fixed-bed reactor exchanger," *Can. J. Chem. Eng.*, vol. 95, no. 2, pp. 241–252, Feb. 2017.

[114] V. Alzate-Restrepo and J. M. Hill, "Effect of anodic polarization on carbon deposition on Ni/YSZ anodes exposed to methane," *Appl. Catal. A Gen.*, vol. 342, no. 1–2, pp. 49–55, 2008.

[115] J. Maček, B. Novosel, and M. Marinšek, "Ni-YSZ SOFC anodes-

Minimization of carbon deposition," *J. Eur. Ceram. Soc.*, vol. 27, no. 2–3, pp. 487–491, 2007.

[116] F. Rahbar Shamskar, M. Rezaei, and F. Meshkani, "The influence of Ni loading on the activity and coke formation of ultrasound-assisted co-precipitated Ni–Al_2O_3 nanocatalyst in dry reforming of methane," *Int. J. Hydrogen Energy*, vol. 42, no. 7, pp. 4155–4164, Feb. 2017.

[117] Z. Jiang, X. Liao, and Y. Zhao, "Comparative study of the dry reforming of methane on fluidised aerogel and xerogel Ni/Al_2O_3 catalysts," *Appl. Petrochemical Res.*, vol. 3, no. 3–4, pp. 91–99, 2013.

[118] D. San-José-Alonso, J. Juan-Juan, M. J. Illán-Gómez, and M. C. Román-Martínez, "Ni, Co and bimetallic Ni-Co catalysts for the dry reforming of methane," *Appl. Catal. A Gen.*, vol. 371, no. 1–2, pp. 54–59, 2009.

[119] K. S. W. Sing, "Reporting physisorption data for gas/solid systems with special reference to the determination of surface area and porosity (Recommendations 1984)," *Pure Appl. Chem.*, vol. 57, no. 4, pp. 603–619, Jan. 1985.

[120] E. P. Barrett, L. G. Joyner, and P. P. Halenda, "The Determination of Pore Volume and Area Distributions in Porous Substances. I. Computations from Nitrogen Isotherms," *J. Am. Chem. Soc.*, vol. 73, no. 1, pp. 373–380, Jan. 1951.

[121] G. Weatherbee, "Hydrogenation of CO_2 on group VIII metals II. Kinetics and mechanism of CO_2 hydrogenation on nickel," *J. Catal.*, vol. 77, no. 2, pp. 460–472, Oct. 1982.

[122] NIST Standard Reference Data, "NIST Chemistry WebBook." [Online]. Available: https://webbook.nist.gov/chemistry/.

[123] G. F. Froment, K. B. Bischoff, and J. De Wilde, *Chemical reactor analysis and design*, 3rd Editio., vol. 2. Wiley New York, 2012.

[124] H. S. Fogler, *Elements of chemical reaction engineering*, 3rd ed. Pearson Education, 2010.

[125] O. Levenspiel, *Chemical Reaction Engineering*, Third Edit. John Wiley & Sons, Inc., 1999.

[126] S. E. Wanke and P. C. Flynn, "The Sintering of Supported Metal Catalysts," *Catal. Rev.*, vol. 12, no. 1, pp. 93–135, Jan. 1975.

[127] C. H. Bartholomew, "Sintering kinetics of supported metals: new perspectives from a unifying GPLE treatment," *Appl. Catal. A, Gen.*, vol. 107, no. 1, pp. 1–57, 1993.

[128] D. Schlereth and O. Hinrichsen, "A fixed-bed reactor modeling study on the methanation of CO_2," *Chem. Eng. Res. Des.*, vol. 92, no. 4, pp. 702–712, Apr. 2014.

[129] J. M. P. Q. Delgado, "A critical review of dispersion in packed beds," *Heat Mass Transf. und Stoffuebertragung*, vol. 42, no. 4, pp. 279–310, 2006.

[130] D. J. Gunn, "Axial and radial dispersion in fixed beds," *Chem. Eng. Sci.*, vol. 42, no. 2, pp. 363–373, 1987.

[131] R. H. Perry, *Perry's Chemical Engineers' Handbook Seventh*, 8th Editio. New York, 1997.

[132] R. B. Bird, W. E. Steward, and E. N. Lightfoot, *Transport Phenomena*, Revised Se. Wiley International edition, 2007.

[133] C. N. Satterfield and C. N. Satterfield, *Mass Transfer in Heterogeneous Catalysis*, vol. 39, no. 4. MIT press Cambridge, MA, 1970.

[134] J. Xu and G. F. Froment, "Methane steam reforming, methanation and water-gas shift: I. Intrinsic kinetics," *AIChE J.*, vol. 35, no. 1, pp. 88–96,

Jan. 1989.

[135] R. G. Deissler and J. S. Boegli, "An investigation of effective thermal conductivities of powders in various gases," *Trans. Am. Soc. Mech. Engrs.*, vol. 80, p. 1417-1425, 1958.

[136] W. Van Antwerpen, C. G. Du Toit, and P. G. Rousseau, "A review of correlations to model the packing structure and effective thermal conductivity in packed beds of mono-sized spherical particles," *Nucl. Eng. Des.*, vol. 240, no. 7, pp. 1803–1818, 2010.

[137] R. Krupiczka, "Analysis of thermal conductivity in granular materials," *Int. Chem. Eng.*, vol. 7, no. 1, pp. 122–144, 1967.

[138] D. Wen and Y. Ding, "Heat transfer of gas flow through a packed bed," *Chem. Eng. Sci.*, vol. 61, no. 11, pp. 3532–3542, 2006.

[139] O. Bey and G. Eigenberger, "Gas flow and heat transfer through catalyst filled tubes," *Int. J. Therm. Sci.*, vol. 40, no. 2, pp. 152–164, 2001.

[140] M. Winterberg and E. Tsotsas, "Correlations for effective heat transport coefficients in beds packed with cylindrical particles," *Chem. Eng. Sci.*, vol. 55, no. 23, pp. 5937–5943, 2000.

[141] P. B. Whalley, *Boiling, condensation, and gas-liquid flow*. Clarendon Press, 1987.

[142] National Institute of Standards and Technology NIST, "NIST chemistry Webbook," *Choice Reviews Online*, 1998. [Online]. Available: http://choicereviews.org/review/10.5860/CHOICE.35-2709. [Accessed: 20-Jan-2017].

[143] B. Poling, J. Prausnitz, and J. O'Connell, *The Properties of Gases and Liquids*, 5th ed. 2000.

[144] D. F. Fairbanks and C. R. Wilke, "Diffusion Coefficients in Multicomponent Gas Mixtures," *Ind. Eng. Chem.*, vol. 42, no. 3, pp. 471–475, Mar. 1950.

[145] C. H. Bartholomew, "Sintering Kinetics of Supported Metals: Perspectives from a Generalized Power Law Approach," *Stud. Surf. Sci. Catal.*, vol. 88, no. C, pp. 1–18, 1994.

[146] S. Abate *et al.*, "Catalytic Performance of γ-Al$_2$O$_3$–ZrO$_2$–TiO$_2$–CeO$_2$ Composite Oxide Supported Ni-Based Catalysts for CO$_2$ Methanation," *Ind. Eng. Chem. Res.*, vol. 55, no. 16, pp. 4451–4460, Apr. 2016.

Appendix A

A.1 Hydrogen temperature reduction

The reducibility of the catalyst was investigated using a hydrogen temperature programmed reduction technique (H_2-TPR). The tests were performed in a homemade setup. A 200 mg fresh catalyst sample was loaded into a U-shaped quartz tube reactor with an internal diameter of 4 mm. The reactor was then placed into temperature-controlled oven. The H_2-TPR was performed with a 200 ml/min gas mixture containing 5% of H_2 in N_2 and with a heating rate of 5°C/min up to 800°C. Hydrogen consumption was monitored using a multi-channel Emerson X-Stream gas analyser equipped with non-dispersive infrared (NDIR) sensors for CO, CO_2 and CH_4, a thermal conductivity (TCD) detector for H_2 and a paramagnetic sensor for O_2 measurement. The temperature was recorded using a thermocouple placed within the catalyst bed.

In Figure A.1 the hydrogen concentration variation is reported. The reduction peaks characterize the metal-support interaction[55], [146]. The deconvolution of the TPR profile has allowed to identify the presence of three reduction peaks ($R^2 \geq 0.99$). A big reduction peak was observed at around 290°C. This peak can be assigned to the reduction of surface amorphous NiO and bulk NiO. Two more peaks were identified at 445 °C and 492 °C that can be assigned to NiO weakly and strongly interacting with the Al_2O_3 support. The activation temperature of 260°C that is used in the real plant will only reduce part of the NiO. About 22% of the total hydrogen uptake takes place during the activation procedure. This corresponds to the same fraction of reduced nickel.
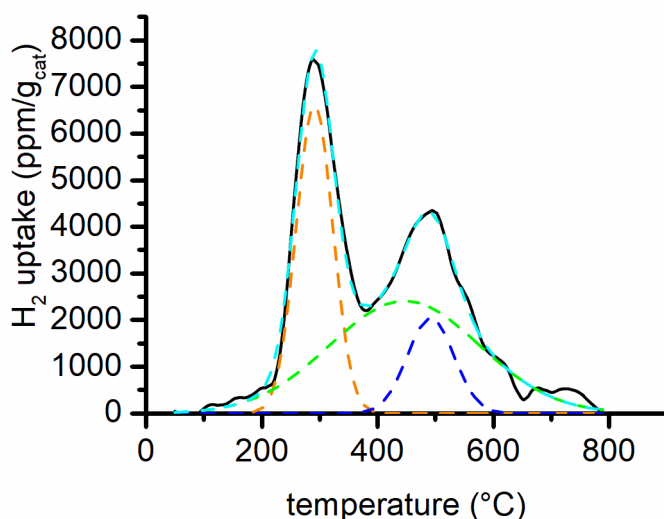

Figure A.1: H_2-TPR with peak deconvolution

A.2 CO₂ temperature programmed desorption

The CO_2 adsorption capacity of the catalyst was investigated by performing a CO_2-TPD. The same apparatus used for the TPR analysis was employed also for the TPD. A 200 mg sample of catalyst was reduced in situ at 400°C prior to the analysis. The sample was then saturated with carbon dioxide at room temperature under continuous flow (100 ml/min, 10% CO_2 in nitrogen) for one hour. After cleaning the sample for 30 minutes under nitrogen flow the desorption was started. A heating rate of 10°C/min and a 200 ml/min of N_2 were used during the desorption.

In Figure A.2 the CO_2 concentration evolution is reported. Most of the adsorbed CO_2 is released at temperature below 350°C. This result was useful for the identification of the catalyst samples pre-treatment procedure before the TPO analysis.
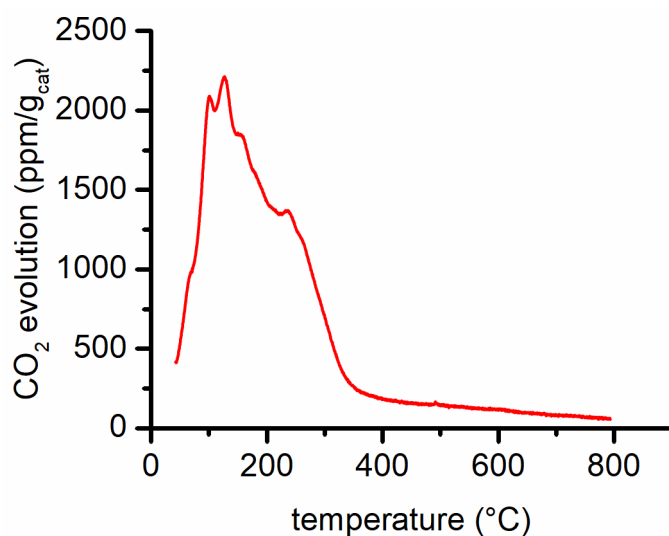

Figure A.2: CO₂ evolution during TPD analysis